Szczepan Piotr Polak

Laboratory and Numerical Study of Scaling Parameters Used in Modelling of CO_2 Storage in Rocks

Thesis for the degree of Philosophiae Doctor

Trondheim, September 2014

Norwegian University of Science and Technology
Faculty of Engineering Science and Technology
Department of Petroleum Engineering
and Applied Geophysics

NTNU – Trondheim
Norwegian University of
Science and Technology

NTNU
Norwegian University of Science and Technology

Thesis for the degree of Philosophiae Doctor

Faculty of Engineering Science and Technology
Department of Petroleum Engineering and Applied Geophysics

ISBN 978-82-326-0420-3 (printed ver.)
ISBN 978-82-326-0421-0 (electronic ver.)
ISSN 1503-8181

Doctoral theses at NTNU, 2014:254

Printed by NTNU-trykk

Acknowledgements

I would like to thank to everyone who had his or her share in the accomplishment, which took form of this PhD thesis.

I would especially like to thank Professor Ole Torsæter for being an excellent supervisor during my doctoral studies. Thank you for sharing your great knowledge in science and your professional experience with me. You were always enthusiastic about my work and ready to provide advices and valuable criticism at any time. Thank you also for being cheerful, patient, and for respecting my way of doing things.

I would like to thank my co-supervisor, Dr Torleif Holt, for guidance during completion of this PhD work. I highly appreciate the good discussions we had, your constructive critic and comments as well as help with laboratory experiments.

Special acknowledgments go to Dr Yildiray Cinar, for supervising me during my stay at The School of Petroleum Engineering, University of New South Wales (UNSW), Australia. Large part of the work presented in this thesis would not happen without your inspiration and support.

Great thanks to all my former colleagues from SINTEF Petroleum AS for constant support during the course of my PhD work. My laboratory activities were patiently supervised and assisted by Øyvind Haave, Oddmund Frigård, Svein Arild Utne, and Dr Bård Bjørkvik. Thank you for sharing your professional experience with me.

I also gratefully acknowledge Dr Erik Lindeberg and Dr Alv-Arne Grimstad for fruitful discussions, providing help in solving problems, and sharing important advices.

Many thanks to Per Bergmo for involving me in his work, which became a part of this thesis.

My laboratory activities at UNSW would not progress without assistance of Nino Zajaczkowski and Dr Furqan Hussain. I am grateful for your help and company.

I would also like to thank to my current colleagues at Statoil for their patience and understanding that I have been less available at the final stage of work with the thesis.

I would like to thank to my family for understanding, patience and support during the work with the thesis. Special thanks to my parents, who always believed in me and supported me. Thanks to them I could reach to the point where I find myself now. Thank you also, for constantly and tirelessly asking when I intend to finish my PhD.

I am indebted especially to my wonderful wife, Anna Zofia, for believing in me, unconditional support, and patience. Thank you for proofreading the thesis and showing how to improve it. Your proficiency in use of graphical software significantly reduced number of my sleep-deprived nights. Thank you for caring for me so I have not suffered from malnutrition during periods of intense work. Thank you for cheering me up when things were difficult, and giving me a push whenever it was necessary. Without your help, it would be much more difficult to complete the work on the thesis.

Finally, I would like to thank the Norwegian University of Sciences and Technology (NTNU) and the Department of Petroleum Engineering and Applied Geophysics for giving me the opportunity to conduct my PhD studies. I would like to acknowledge SINTEF Petroleum AS and The School of Petroleum Engineering (UNSW) for making their facilities available to perform this research. I would like to acknowledge the BIGCO2 project, performed under the strategic Norwegian research program CLIMIT, for providing funding for this PhD fellowship. And the last but not least, I would like to acknowledge the funding provided by the Australian Government through the CRC Program to support CO2CRC research.

Szczepan P. Polak
Bergen, March 2014

Abstract

Storage of CO_2 in deep saline formations is currently the most promising option for mitigating the impact of climatic changes. The main concern related to CO_2 storage in geological formation is safety. It is necessary that injected CO_2 is under control at all times and its behaviour is predictable. Therefore, it is important to understand flow processes and distribution of forces acting underground on CO_2 during and after injection. It is also crucial to know what happens with CO_2 after tens, hundreds and even thousands of years after it has been injected. The only way to predict movement of CO_2 in such a long time span is by modelling processes that take place underground. This work presents findings of both experimental and numerical modelling of flow processes taking place during and after CO_2 injection.

Special experiments were designed in order to demonstrate the influence of gravitational, viscous, and capillary forces on the flow of CO_2. In laboratory experiments fluid representing CO_2 was injected into a 2D porous medium saturated with fluid representing brine. Two sets of fluids characterized by different interfacial tension (IFT) were tested. Results of the experiments demonstrate that at increasing injection rate viscous forces become stronger. This leads to a higher total displacement of brine. Such performance facilitates dissolution and residual trapping of CO_2 and is desired at the field scale. However, such conditions can lead to pressure increase in the near-well zone due to injection and this can possibly damage the geological formation by fracturing, which in turn, can compromise safety of the storage site.

At low injection rates and high permeability, gravity effects increase their influence. This is demonstrated by lower volumes of the in-situ fluid displacement what is not favourable during CO_2 storage. Therefore, reservoirs giving low influence of gravity forces are more suitable for CO_2 storage.

Although the high-IFT fluid system had an IFT corresponding to the value of CO_2-brine systems at possible reservoir conditions the flow in laboratory model was dominated by capillary forces. This kind of behaviour is less likely to be observed at

the field scale. However, observations at the low-IFT fluid system resemble better the field scale flow behaviour.

A scaling analysis of the experiments and reservoir cases was performed based on dimensionless numbers. It showed that the experimental capillary number and viscous-to-gravity ratio at high-IFT and low injection rate agree reasonably well with calculations for some of the sedimentary basins and storage sites. However, low-IFT experiments scale far from the field cases when the range of flow velocities is assumed to be the same in field cases and in experiments. Range of velocities observed in experiments is expected to occur in the reservoir far from the injection point, where the gravity forces dominate. The scaling analysis showed importance of various parameters in the process of site characterisation for CO_2 storage. Representation of the reservoir conditions by means of the dimensionless analysis provides possibility of comparing various storage sites and predicting the flow regimes that may occur when CO_2 is injected.

The laboratory experiments were modelled using numerical reservoir simulation software. In case of high-IFT system the flow was dominated by channelling. These features were caused by strong capillary effects and were challenging to model. This problem was solved by modifying properties of the simulation grid and results of sensitivities are presented. Simulations of low-IFT displacements showed accurate reflection of experiments.

Sensitivities on influence of capillary pressure were also performed. In the laboratory experiments capillary pressure was negligibly small but in the field scale modelling on generic models results proved to be very susceptible to this parameter. It strongly influences migration speed and thickness of the CO_2 front.

Further analysis on full field case showed that low permeability of the storage site will have negative impact on the storage capacity and well injectivity. Due to low permeability the injected CO_2 will not be able to reach all parts of the reservoir, hence not all available pore space will be utilized. Additionally, limited injectivity will result in lower injection rates, as increase of pressure in the near-well zone has to be avoided, or introduction of additional injection wells will be necessary to compensate for lower injection rates.

Table of Contents

1 Introduction

1.1 Background

In the light of growing evidence on greenhouse gases (GHG) negative influence on Earth's climate (Stocker et al. 2013; IPCC 1995, 2001), scientific communities from all around the world have begun in recent years to investigate various methods of mitigating the excess emissions of GHGs to the atmosphere. Numerous national and international consortia with scientific and industrial partners were established in order to work together towards researching and developing methods for remediating climate changes. The most common GHG is carbon dioxide (CO_2) and its largest sources are power and industry sectors (IPCC 2005). One of the methods of reducing CO_2 emission that particularly has got attention is its geological storage (e.g. CO2CRC 2008; IPCC 2005). The goals of the scientific consortia were and are ranging from more specialized ones, focusing only on one objective, like capture of CO_2 (e.g. ENCAP, CACHET) or selection of suitable storage site (e.g. CO2SINK, CO2GEONET) to such that take into consideration the whole process-chain from capture through transport to underground storage of CO_2 (European Commission 2007). An example of such consortium was an international collaborative research project BIGCO2 R&D Platform in which this PhD project was initiated. The ambition of the BIGCO2 Platform was to investigate technological options for carbon capture and storage (CCS) and develop scientific basis for CCS solutions. It had focus on lower costs and higher efficiency, which in turn would support a large-scale deployment of CO_2 capture from power generation and its underground storage (Mølnvik et al. 2012).

1.2 Project scope and objectives

The main concern when it comes to CO_2 storage in geological formation is safety. Keeping in mind that leakage of CO_2 to the surface is not an option, it is therefore very important to understand processes that take place within formation after CO_2 is injected. It is also crucial to know what happens with CO_2 after tens, hundreds and even thousands of years after it has been injected. The only way to predict movement of CO_2 in such a long time span is by modelling processes that take place underground. Computer modelling is one of the tools which is commonly used for foreseeing possible leakage paths, and by that, significantly reduces risk of problems in the distant future. Another important tool that helps in understanding basic flow processes that may take place underground is experimental modelling.

As this PhD project focuses on issues related to CO_2 storage in geological formations, the following objectives were identified:

- Improve understanding of the flow processes that take place within the reservoir during CO_2 injection
- Experimentally investigate the scaling laws which describe CO_2 injection into saline aquifers
- Demonstrate the influence of gravitational, viscous and capillary effects on the vertical flow of CO_2
- Use simulation tools to model various aspects of CO_2 behaviour based on laboratory experiments and full-field cases with focus on migration patterns and storage safety.

This work looks at the basic flow processes that take place when CO_2 is injected as well as modelling of them at both laboratory and full-field scale. In the series of laboratory experiments performed on synthetic porous medium, the balance between capillary, viscous, and gravity forces has been studied. Further, these processes are modelled in simulation tool both at laboratory scale and elements of the observations are taken into full field models. The work that focuses on laboratory experiments is described in Paper II and Paper IV. In the latter, detailed computer modelling of the experiments has been presented. Additional details on simulations and various sensitivities in relation to the used parameters are described in this thesis. In Paper III, results of the full-field reservoir simulations are presented, both on a generic model and on a real reservoir. Also Paper I concerns reservoir simulations on a real full-field model, however it describes another type of geological setting as well as risks related to the CO_2 leakage through abandoned wells.

2 Theoretical background

2.1 Anthropogenic CO_2 vs. climate change

Data gathered and analysed by scientists indicates that since the late 19th century the Earth's surface temperature has increased (IPCC 2001, 1995; Stocker et al. 2013). The Intergovernmental Panel on Climate Change (IPCC) has concluded that climate change is a fact and that its causes and effects should be mitigated.

The main cause of the climate change is the anthropogenic emission of greenhouse gases (GHG) as a result of fossil fuel combustion. Six gases (or groups of gases) have been identified as GHG under the Kyoto Protocol. These are: Carbon dioxide (CO_2), Methane (CH_4), Nitrous oxide (N_2O), Hydrofluorocarbons (HFCs), Perfluorocarbons (PFCs), and Sulphur hexafluoride (SF_6). In order to mitigate GHG effect on climate change it is necessary to significantly reduce their emission (IPCC 2001, 1995). In 2004, yearly emission of GHG reached 49 Gigatonnes (Gt) of CO_2-equivalents. CO_2 constitutes about 70% of this amount. Power and industry sectors are responsible for 60% of total CO_2 emission (IPCC 2005).

Concentration of CO_2 in atmosphere in the pre-industrial time was 280 ppmv (parts per million by volume) (IPCC 1995). Due to fossil fuel combustion its current concentration is 380 ppmv (IPCC 2005) and quickly approaching 400 ppmv (NOAA Earth System Research Laboratory 2014). If CO_2 emissions will continue at the current level it will certainly cause further increase of the Earth's surface temperature. In the mitigation scenarios for stabilisation of atmospheric GHG the concentration is expected to reach range of 450-750 ppmv of CO_2 (IPCC 2005). Reduction in use of fossil fuels by replacing them with renewable sources of energy is one of the solutions that would certainly lower emission of CO_2 to the atmosphere. However, this is not expected to be significant contribution to lower emissions in the near future. Presently there are several other methods identified which can be utilized in order to reduce CO_2

emissions. One of those that have got particular attention in recent years is geological storage of CO_2.

2.2 Geological storage of CO_2

The process, during which CO_2 is injected into the subsurface, after being captured from a source and transported, is called CO_2 storage. There are several possible methods for storing CO_2 in geological formations (e.g. IPCC 2005; CO2CRC 2008):

- Depleted oil and gas reservoirs,
- CO_2 enhanced oil/gas recovery (CO_2-EOR/EGR),
- Saline aquifers,
- Deep and unminable coal seems,
- CO_2 Enhanced Coal-Bed Methane recovery (ECBM),
- Other options – storage in basalts, oil shales, cavities.

CO_2 is naturally present in geological formations. Its accumulations that occur throughout the world are important source of information on long-term safety of the underground CO_2 storage. Natural CO_2 is present in CO_2-rich water, both in springs and underground. These resources are often used for production of mineral water. Other sources of natural CO_2 are dry gas vents associated with Cenosoic rifts, hydrothermal fields, and Quaternary to recent volcanic activity (e.g. Baines and Worden 2004; Pearce et al. 2004). CO_2 accumulations are natural laboratory that can provide information needed for better assessment of potential storage sites for anthropogenic CO_2. They are often close to populated areas, some of them are leaking while others are well sealed. Good understanding of these sites can provide valuable data for the reservoir modelling.

The most promising geological storage option for CO_2 is its injection into deep saline aquifers. Saline aquifers are sedimentary rock formations which are saturated with brine. These brines are not suitable neither for human consumption nor for agriculture (e.g. IPCC 2005). Saline aquifers are considered to be the best option for CO_2 storage due to their large storage capacity potential (Table 2.1).

Table 2.1 ***Storage capacity for geological storage options. The storage capacity includes storage options that may not be economically viable (from IPCC 2005).***

Reservoir type	Estimate of storage capacity (Gt of CO_2)
Oil and gas fields	675-900
Unminable coal seams (ECBM)	3-200
Deep saline formations	1000-10000*
*) uncertain, but possible	

In potential storage formations various conditions can be encountered which may be favourable for storing CO_2. Several factors should be taken into consideration while assessing site for CO_2 storage. The most important are storage capacity, injectivity potential, caprock quality and distance to the CO_2 source. There are some positive indicators for saline aquifers such as high porosity (>20%), high permeability (>500 mD), relatively large thickness of the formation (>50m), suitable depth (>1000m <2500m), uniform stratigraphy with no faults (preferentially with structural traps, such as domes or anticlines), capillary entry pressure in caprock much higher than maximum predicted injection induced pressure increase and large thickness of a caprock (>100m) (e.g. Chadwick et al. 2008; CO2CRC 2008). However, these constraints are not strict and each potential storage site needs to be assessed individually.

Depending on the conditions in the storage formations the CO_2 may behave differently. In highly permeable rocks, injected CO_2 will rise quickly to the top of formation and will accumulate under the seal. In case the seal is imperfect, it may lead to a leakage. On the other hand, if the rock has low permeability, the injectivity of CO_2 will be lower than in high-permeable formation. In order to keep high injection rate in the low permeable formation, the injection pressure would have to be increased. This can lead to dangerous conditions at which the formation could be damaged by fracturing. To avoid such situation, additional injection wells might be needed in order to accommodate desired throughput without increasing injection pressure. This issue is discussed in Paper I (Polak and Grimstad 2009) and Paper III (Bergmo et al. 2013). However, low permeability is a desired factor for efficient permanent trapping of CO_2. In such formation CO_2 will be slowly moving through a reservoir and thus will be contacting more pores (residual trapping) and water (diffusion and dissolution) which is favourable for permanent trapping (see 2.3 CO2 trapping mechanisms). Fluid flow behaviour in low- and high-permeable porous media on a laboratory scale is presented later in this thesis, and in Paper II (Polak et al. 2011) and Paper IV.

Presently, there is a number of on-going and planned CO_2 storage projects, both as scientific pilots and at commercial scale. These projects take place, among others, in Norway, Australia, USA, Germany, and Japan (IPCC 2005; IEA-GHG 2009).

The first and probably the best known example of geological storage of CO_2 is Norwegian CO_2 offshore storage project in the saline aquifer in the Utsira Formation at the Sleipner field in the North Sea (operated by Statoil). It was the first project of the industrial scale and CO_2 injection started there already in 1996 (Baklid et al. 1996). Another Norwegian offshore CO_2 storage project is at Snøhvit gas field in Barents Sea (operated by Statoil) (Maldal and Tappel 2004). In both these cases CO_2 comes from stripping a natural gas from CO_2. It is later injected underground instead of being released to the atmosphere. In Salah gas field in Algeria (operated by Statoil, BP, and Sonatrach) is another example of the CCS operation (Riddiford et al. 2003). Also in this case CO_2 is separated from produced gas, but contrary to two projects mentioned earlier, this one is an onshore project. It is the first geological storage of CO_2 in the deep saline formation of an active gas reservoir (started in 2004).

These are only a few examples of CO_2 storage projects. Overview of on-going and completed projects can be found on the IEA Greenhouse Gas R&D Programme website (http://ieaghg.org/).

2.3 CO_2 trapping mechanisms

Within saline aquifer formation CO_2 is stored by different trapping mechanisms. Many authors propose classifications for trapping mechanism that differ from the one presented in Figure 2.1 (e.g. Chadwick et al. 2008; CO2CRC 2008; IPCC 2005; Pearce et al. 2004; Gunter et al. 2004). Considering only the most basic trapping mechanisms they can be classified as shown in Figure 2.1.

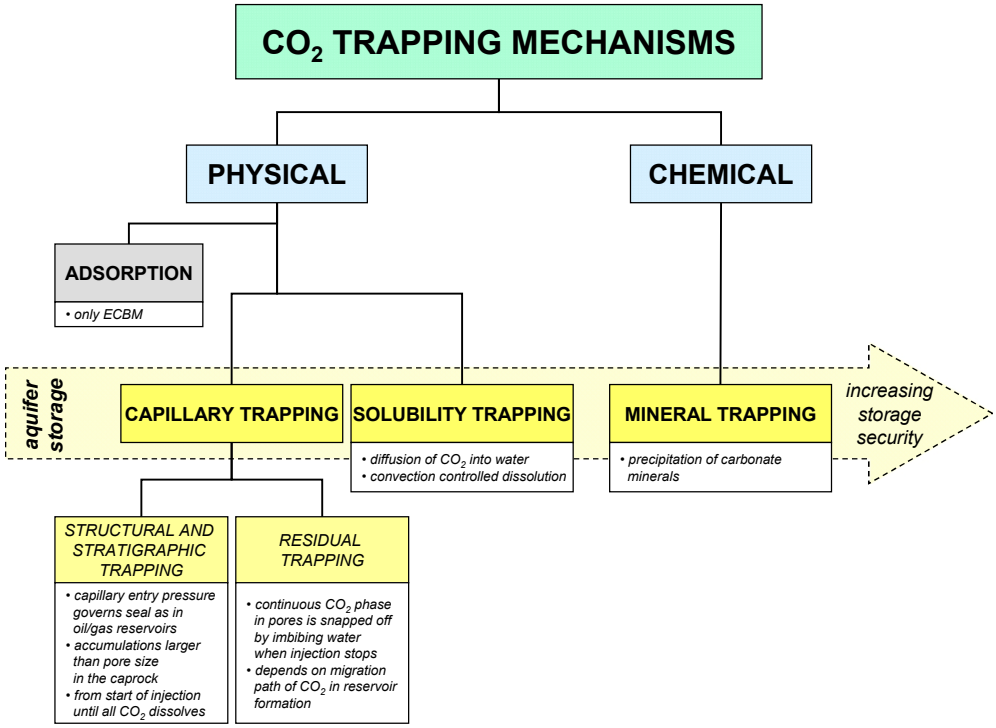

Figure 2.1 Trapping mechanisms in geological storage of CO_2.

Trapping mechanisms can be grouped either into physical or chemical processes. Physical trapping mechanisms can be divided into three groups: adsorption, capillary trapping and solubility trapping (Figure 2.1). Adsorption is a dominant trapping mechanism in the Enhanced Coal-Bed Methane (ECBM) recovery process. CO_2 is adsorbed at the coal surface where it replaces methane, which in turn could be commercially produced.

Capillary trapping mechanism refers to the CO_2 being trapped by capillary forces. Rocks with high capillary entry pressure constitute seal that can form stratigraphic and structural traps. CO_2 within such traps is stored similarly to hydrocarbon accumulations. This kind of trapping mechanism is acting from start of injection until all CO_2 is dissolved.

Stratigraphic or structural traps, however, are not essential for retaining CO_2. In aquifers with flow (order of centimetres per year) injected CO_2, both dissolved and free, can travel with the formation water for very long residence time when distance from injection point to the formation outcrop is hundreds of kilometres. In such case

seal does not constitute structural trap and even if inclined it can still provide safe storage site.

When CO_2 flows through the pores it forms continuous phase. Once CO_2 stops to flow, water invades pores (imbibition) and snaps off CO_2, which becomes trapped as discontinuous phase and is immobilized. This mechanism is called residual trapping. There is, however, an exception where this kind of trapping mechanism is not present. If CO_2 was injected at the top of reservoir, just under the seal, it would move radially and downwards, displacing water. In this case water would not invade pores after stop of injection process. Only after CO_2 dissolves water can flood back the pores, however capillary trapping would still not take place.

Solubility trapping mechanisms is simply dissolution of CO_2 in water. It is reversible process and depends on temperature and pressure. Dissolution of CO_2 can be expressed by following reaction path:

$$CO_{2(g)} + H_2O \leftrightarrow H_2CO_3^* \leftrightarrow HCO_3^- + H^+ \leftrightarrow CO_3^{2-} + 2H^+$$

Equation 2.1

CO_2 dissolves in water due to diffusion. It is present in solution as both a dissolved gas $CO_{2(aq)}$ and a true carbonic acid H_2CO_3. Total analytical concentration of dissolved CO_2 can be expressed by composite concentration $[H_2CO_3^*]$ of $CO_{2(aq)}$ and H_2CO_3 (Equation 2.1). However, most of the dissolved CO_2 is present in form of dissolved gas $CO_{2(aq)}$ (Stumm and Morgan 1996). Equation 1 indicates that process that consumes H^+ ions will move reaction to the right and thus cause more CO_2 to be dissolved.

Dissolution of CO_2 can be enhanced by convection process. When CO_2 dissolves, water becomes heavier and gravitationally sinks to the bottom of the formation. Lighter brine without or with very little content of dissolved CO_2 is displaced by denser brine and migrates towards the top of formation (bottom of CO_2 plume) where it contacts CO_2 which continue to dissolve. This process lasts until all CO_2 is dissolved.

Chemical trapping mechanisms is mineral trapping of CO_2. Dissolved CO_2, which in aqueous phase is present as $CO_{2(aq)}$, $H_2CO_3^o$, HCO_3^-, and CO_3^{2-}, reacts with metal ions present in formation water, and precipitates as carbonate minerals. The type of the formed mineral depends on the reservoir chemistry, i.e. composition of a reservoir rock and brine. CO_2 in reactions with host rock and/or ions present in brine may form for example calcite, dawsonite, smectite, and siderite (Rochelle et al. 2004).

Some authors distinguish other trapping mechanisms in addition to these listed above. For example Gunter et al. (Gunter et al. 2004) describes hydrogeological trapping and IPCC (IPCC 2005) and CO2CRC (CO2CRC 2008) refer to hydrodynamic trapping. Both terms relate to process where dissolved as well as free CO_2 travels with

the formation water for very long residence time. Due to the fact that the distance from injection point to the formation outcrop is hundreds of kilometres CO_2 can be considered as permanently stored. Hydrogeological (or hydrodynamic) trapping is nevertheless a combination of three basic trapping mechanisms described earlier – capillary, solubility and mineral trapping. Injected CO_2 flows under the seal (*structural trapping*) and leaves behind *residually trapped* CO_2. In addition, during the flow, CO_2 is dissolved and it may precipitate from solution as carbonate minerals.

Saadatpoor et al. (2008) suggested term *capillary trapping* to describe accumulations of CO_2 within heterogeneous reservoirs. CO_2 injected at the bottom of formation migrates upwards and is trapped under low- or non-permeable zones or, in other words, under zones with high capillary entry pressure. This trapping mechanism can be classified as small-scale *structural trapping*, which has been described above.

At the beginning of injection the largest amount of CO_2 is trapped by capillary trapping mechanism, less by solubility and least by mineral trapping. After the end of injection and progressively afterwards, the balance is moved towards solubility and mineral trapping until all CO_2 is dissolved. The structural and stratigraphic trapping is the most important mechanism for safe storage in short term (human life time) and it is acting until all CO_2 is dissolved. Solubility and mineral trapping importance is increasing in long-term (hundreds to thousands of years) since more CO_2 dissolves in water and can react with other compounds present in solution and precipitate as carbonate minerals. Residual trapping is important when injection stops. CO_2 snapped off in pores will, due to diffusion, slowly dissolve in formation water (CO2CRC 2008; IPCC 2005).

2.4 Risk of leakage and need for monitoring

Trapped CO_2 is less mobile and therefore the risk of leakage to the surface is lower. However, if brine saturated with CO_2 leaks through a caprock, it will be depressurized at lower depths and will release free CO_2. Leakage of CO_2 could be hazardous to human and ecosystems, therefore it is important to identify possible leakage flow paths at the stage of storage site selection, before any injection takes place. CO_2 can leak out of storage site through leaking injection wells, abandoned wells, across faults and ineffective confining layers (IPCC 2005). Nevertheless, brine saturated with CO_2 becomes denser and sinks to the bottom of the saline formation. This limits risk of leakage in a long-term (Lindeberg and Bergmo 2003).

One of the hazards related to a potential CO_2 leakage is contamination of the ground/potable water. Presence of the CO_2 causes decline in the pH and by that

increases concentrations of metals that can be potentially harmful for living organisms, including humans (Little and Jackson 2010). Another threat related to CO_2 is that its very localised and high concentrations in the atmosphere can be dangerous or even lethal to the living organisms. As an asphyxiant gas, already at concentrations of 1% may cause drowsiness, and at concentration of 7 to 10% can cause suffocation (U.S. EPA 2000). However, a number of natural CO_2 seepages occurring throughout the world, indicates relatively low risk of leakage becoming serious threat (e.g. Beaubien et al. 2005), especially considering that constant monitoring and awareness would be introduced at areas where CO_2 would be stored.

Due to the risks related to the leakage of CO_2 there is a need for constant monitoring of the storage sites. During injection phase, and also many years after, a seismic monitoring has to be undertaken (e.g. Arts et al. 2004). Images of the CO_2 underground distribution should be taken sufficiently often in order to assess movement of the CO_2 plume. Knowing where CO_2 is located will facilitate remedy in case of leakage by, for example, producing CO_2 and re-injecting it in another location (Akervoll et al. 2009). In addition to seismic monitoring, further measures must be included in order to ensure maximum control over the storage site, such as analyses of ground water, soil gas, and air. Considering that CO_2 may stay underground in a free form (i.e. not dissolved in water or trapped in minerals) for as many as thousands of years, the monitoring issue may cause problems in recognizing responsibility for the stored CO_2 in such a long time span.

2.5 Properties of CO_2 and CO_2-water mixture

Thermodynamic properties of CO_2 are important parameters, which have to be considered in storage site characterisation process. CO_2 injected underground will be subject to changing pressure and temperature. Its behaviour under these conditions is described by the equation of state (EOS) and can be presented in the *P-T* phase diagram. The simplest EOS that links relation between pressure, temperature and volume of the fluid is the ideal gas law $PV = nRT$ (P – pressure of the gas, Pa; V – volume of the gas, m^3; n – amount of substance of gas, moles; R – gas constant gas constant, 8.3144621(75) J/mol·K; T – temperature of the gas, K). This relationship however, was not suitable to predict the state of real gases, therefore a number of much more advanced EOS have been developed. Presently they can accurately describe changes of state at conditions that are of interest for underground storage of CO_2.

Phase diagram for CO_2

The most important elements of the *P-T* phase diagram for CO_2 are the triple point and critical point. At the triple point all three phases – vapour, solid and liquid – coexist. The temperature at the triple point is -56.57°C and the pressure is 5.185 bar (Angus et al. 1976) (Figure 2.2). The critical point is the point at which the phase boundary between liquid and gas terminates. Above this point the distinction between vapour and liquid is not possible. According to Span and Wagner, 1996, the critical point for CO_2 is at 30.95°C and 73.40 bar (Figure 2.2).

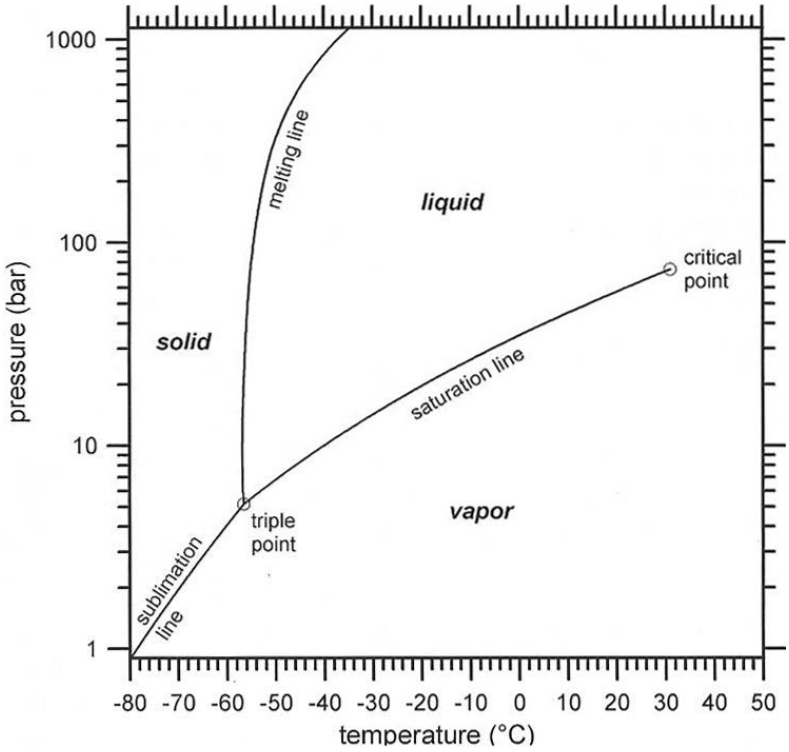

Figure 2.2 Phase diagram for CO_2 (figure from Marini 2007; data from Span and Wagner 1996).

CO_2 is injected into the saline aquifer formation as a supercritical (dense) fluid. Liquid CO_2 can be produced at temperatures lower than the critical temperature and the pressures of tens of bars or higher but it is evident that in most of reservoirs the *P-T* conditions will be favourable for CO_2 storage in supercritical state. Considering worldwide average geothermal gradient and hydrostatic pressure, favourable conditions for supercritical CO_2 occur usually at depths greater than 800m. At this depth and below the density of CO_2 is much higher than in the gas phase and larger

volumes can be stored in available pore space (IPCC 2005; CO2CRC 2008). Variation of CO_2 density with depth is shown in Figure 2.3.

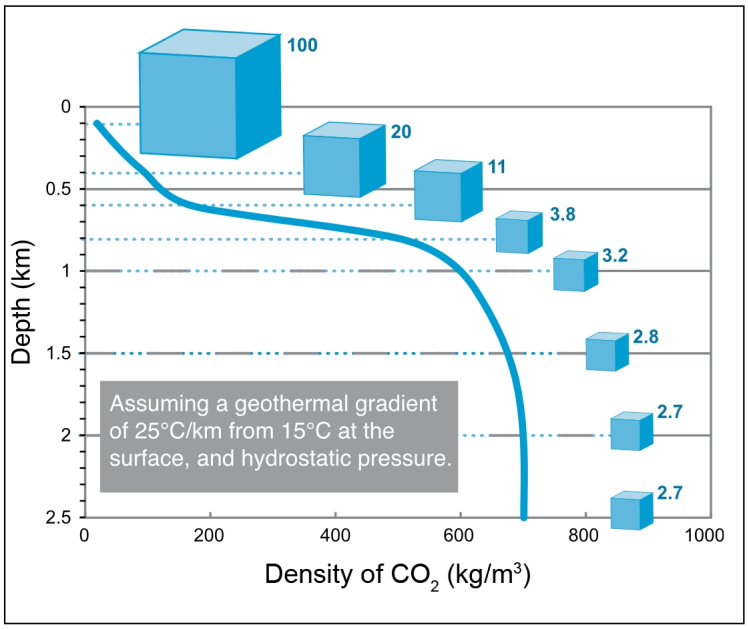

Figure 2.3 ***Increasing storage efficiency for CO_2 with depth; above critical depth, about 800 m, CO_2 is in gaseous state; below critical depth it is in liquid-like state, and its density does not change noticeably with depth (from IPCC 2005).***

Also P-V diagram (Figure 2.4) can be used to describe changes of state. The molar volume which is on the x-axis represents inversed density ($1/\rho$), thus lower values relates to the higher density. Transition from the right side of the diagram to the left above the critical point at the constant pressure does not show change of phase. Below the critical point we go through the region of distinction of two separate phases – liquid and vapour.

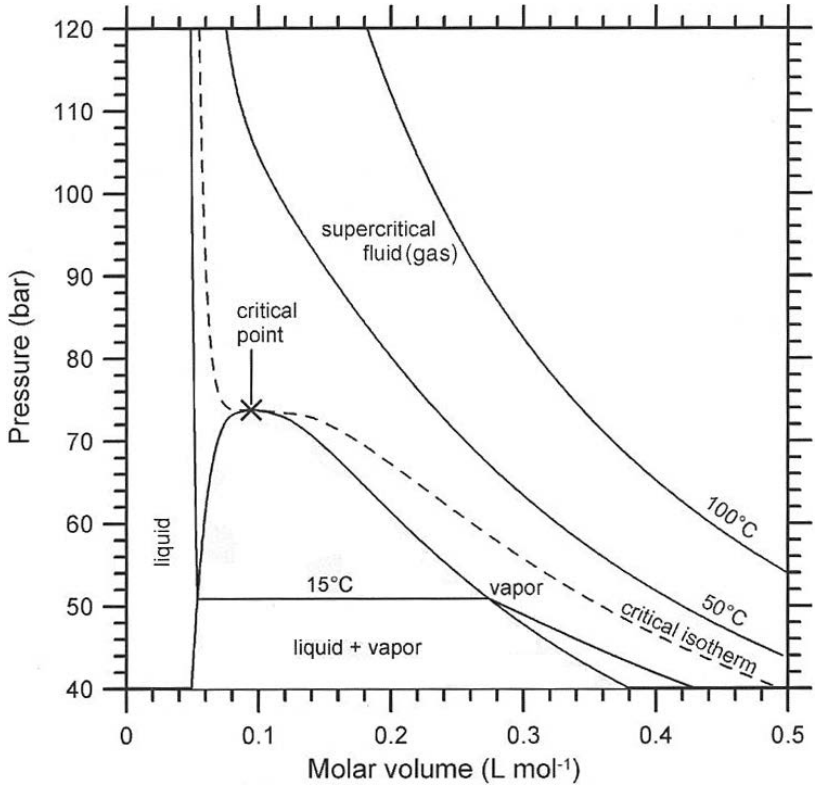

Figure 2.4 P-V diagram for CO_2 (from Marini 2007).

Phase diagram for CO_2-water system

Since supercritical CO_2 is injected into aquifer it is important to look at the influence of aqueous phase on the CO_2 properties. Phase diagram for the CO_2-water system showing different phases, which are stable at low temperatures and relatively low pressures is presented in Figure 2.5.

The Q_1, the first quadrupole point at 9.77 °C and 44.60 bar, represents conditions at which four phases coexist (H, L_{aq}, L_{CO2}, V). This is also an intersection point of three stable curves H+L_{aq}+V, L_{aq}+L_{CO2}+V and H+L_{aq}+L_{CO2} and metastable curve H+ L_{CO2}+V. The Q_2, the second quadrupole point, represents conditions at which H, L_{aq}, V and ice coexist. The ice limits the extension of the H+L_{aq}+V curve. However, this part of the diagram is of negligible interest in CO_2 storage.

The saturation curve of pure CO_2 shown in Figure 2.5 almost overlaps the three-phase curve L_{aq}+L_{CO2}+V. The critical endpoint (CP) for pure CO_2 system is at 30.95 °C and 73.40 bar (Span and Wagner 1996) which is very close to the lower critical end point (LCEP) for CO_2-water system at 31.48 °C and 74.11 bar (Wendland et al. 1999).

Figure 2.5 shows that at the P-T conditions of interest for the geological CO_2 storage, the L_{aq} coexists with a CO_2-rich phase (V or L_{CO2} depending on pressure) below LCEP temperature and above 10 °C. Above temperature of LCEP only CO_2-rich gas is present because distinction between V and L_{CO2} vanishes (Marini 2007).

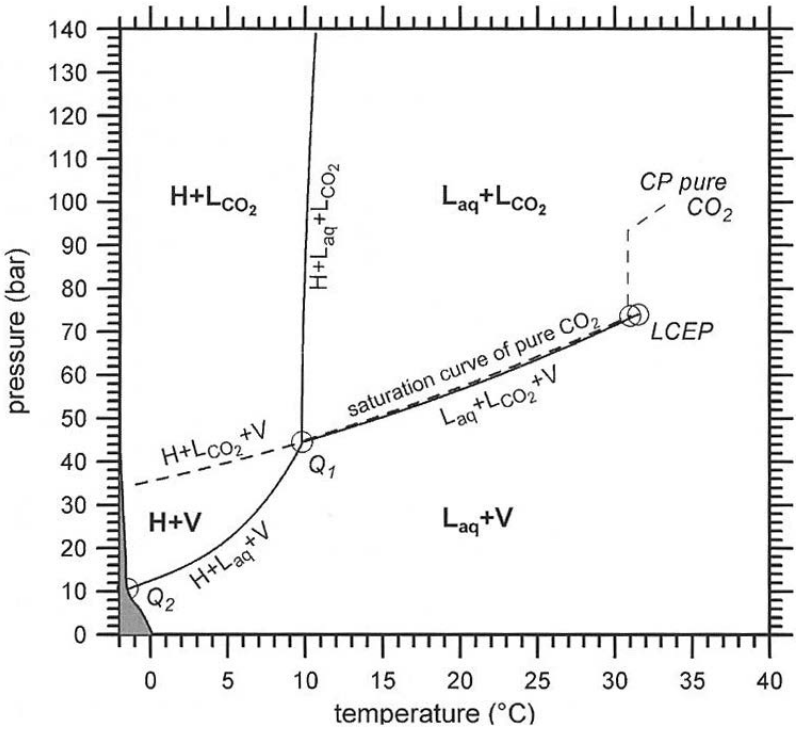

Figure 2.5 ***Phase diagram for the CO_2-water system at low temperatures and relatively low pressures (from Marini 2007): H – a solid, non-stoichiometric CO_2-clathrate-hydrate ($CO_2 \cdot 7.5\ H_2O$), L_{aq} – a CO_2 bearing water-rich liquid (aqueous phase), L_{CO2} – a CO_2-rich liquid phase, V – a CO2-rich vapour phase; the grey area represents the stability field of ice.***

For example, we can look at the conditions of injection point of Utsira CO_2 storage project. CO_2 is injected at depth of 1058 m and the reservoir temperature is 37 °C and pressure is approximately 100 bar (Zweigel et al. 2004; Lindeberg et al. 2009). These values are well above LCEP (and CP) at the CO_2-water phase diagram (Figure 2.5). This means that conditions in reservoir are suitable for CO_2 to stay in supercritical (dense) phase with no distinction on vapour and liquid.

The 'lower' part of the diagram (up to 10-11 °C) is especially interesting from the CO_2 transportation point of view. CO_2 transported in the pipelines on the sea floor or in

cold climate should be dry enough to avoid formation of hydrates (*H* on the diagram). This means that content of water in CO_2 should be below dew-point for a given temperature. Depending on the ambient temperature (e.g. 6 °C at the North Sea floor) the water content in CO_2 has to be adjusted according to needs in order to minimize costs related to removal of water.

Influence of salinity on CO_2 dissolution

Dissolution of CO_2 in pure water depends on temperature and pressure. For supercritical CO_2 at temperatures up to 100°C and pressures up to 300 bar solubility decreases with increasing temperature but increases with increasing pressure (Figure 2.6) (Rochelle et al. 2004).

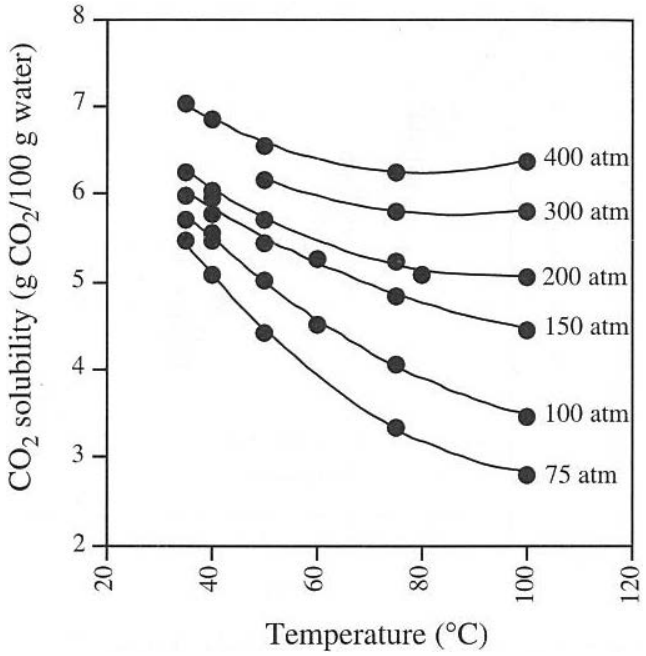

Figure 2.6 Solubility of CO_2 in pure water (from Rochelle et al. 2004).

During geological storage of CO_2 an important factor that controls solubility is a salinity of the formation water. General trend shows that solubility decreases with increasing ionic strength of the solution. However, CO_2 solubility does not depend on the brine composition but on the content of the total dissolved solids (TDS) (Figure 2.7) (Rochelle et al. 2004).

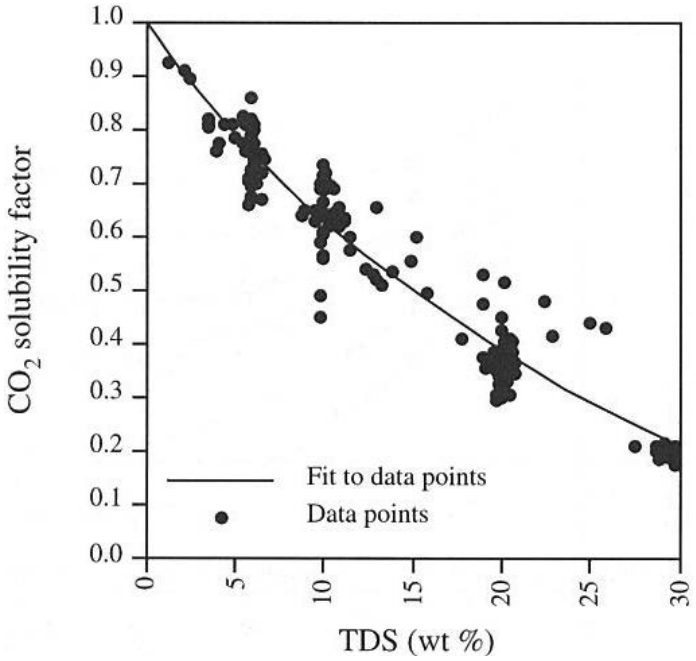

Figure 2.7 ***CO_2 solubility changes with salinity relative to that in pure water (data at 20-250°C and 30-850 bar) (from Rochelle et al. 2004).***

2.6 Forces affecting fluid flow in porous media

Interaction of various forces causes that flow of fluids in a reservoir is unstable and unpredictable. There are three main forces acting on the flow in porous media that can be distinguished: viscous forces, capillary forces, and gravity forces.

Viscous forces are driven by fluids viscosity ratios. At the high viscosity ratio, the viscous forces are low and at low viscosity ratio they are high. Also, the viscous forces are related to the flow velocity, i.e. the higher the flow velocity, the stronger viscous forces. In the field, they will be strongest near the injection well and will get weaker further away from the well as the flow velocity will decrease and the increasing influence of the gravity forces will marked itself. Gravity forces are driven by density difference between fluids. When the gravity forces are dominating it is manifested by fluid flow occurring more in the vertical direction. Also the fluid flow velocity influences strength of the gravity forces causing that they increase when the velocity is lower. Consequently, gravity forces will dominate further away from the injection well, where the flow velocity of injected fluid is low (Taku Ide et al. 2007).

Capillary forces come from interfacial forces between immiscible fluids and are stronger at systems with higher interfacial tension. Capillary forces, in a way, are acting against the flow as they are responsible for creating capillary barriers such as caprocks. Due to the interfacial tension between the fluids, on the pore scale, capillary forces will be stronger in smaller pores (e.g. caprock) than in large ones (e.g. reservoir formation). Therefore pore distribution in porous medium will have influence on the flow pattern. When flow is dominated by capillary forces, it will create fingers or channels that follow larger, and thus more permeable, interconnected pores (Løvoll et al. 2005).

Further in this thesis, the balance between these forces is discussed and results of experimental and numerical investigation of their influence on fluid flow in model porous medium are presented (also in Paper II and Paper IV).

2.7 Reservoir simulation tools

There are several reservoir simulation tools that can be used for modelling of both fluid flow and chemical reactions of CO_2 underground storage. One of the most commonly used flow simulators are Eclipse 100 and Eclipse 300 (both developed and distributed by Schlumberger Limited). The former is a black-oil simulator (does not use fluid composition), which is particularly useful in modelling of CO_2 storage in deep saline formations. The latter, Eclipse 300, is a compositional type of the simulator, especially useful in modelling of CO_2-EOR related problems.

Another popular simulation tool is GEM developed by Computer Modelling Group Ltd. It is a compositional simulator, popular in modelling CO_2 related problems. Simulators that take into consideration multiphase reactive flow of the fluids (reactive transport modelling) are COORES (developed by IFP-EN), TOUGH2 and TOUGHREACT (both developed at Lawrence Berkeley National Laboratory).

All simulations presented in this work are performed by means of Eclipse 100.

2.8 Need for more research

Currently there are many CCS project that are being planned or under development. Unfortunately there is still lack of large-scale approach that could help to accommodate significant volumes of the CO_2 emissions. One of the main reasons for that are issues related to costs of large scale CCS deployment. Also doubts regarding storage security are often raised in addition to questioning whether CCS could help mitigate climate change. Scientific communities are busy trying to investigate all kinds

of phenomena related to CCS, and present results to the public in the most informative way. Since the geological storage of CO_2 may become the most important mean for mitigation of climate change, it created need for extensive research. CO_2 storage does not have such a long research history as petroleum sciences but many of their technics can be used in order to better understand interaction of the CO_2 with the rocks underground. Although current state of the art is sufficient to perform large-scale CCS projects, there is still need for basic research. This will increase confidence and assure sceptics that CO_2 storage in geological formations is reliable and safe, and that it is the most efficient method of remediating global climate change.

3 Laboratory experiments and numerical simulations

Experimental and numerical investigation of the scaling laws describing CO_2 injection into saline aquifers is presented in this part of the thesis. Laboratory experiments represent CO_2 injection into model saline aquifer and influence of the low and high interfacial tension (IFT) fluid systems on the scaling relevance. Results, discussion, and main conclusions of this work are presented in Paper II (Appendix B) and Paper IV (Appendix D). Chapter 0 contains a summary of the findings presented in these papers. Moreover, this chapter encloses details of the research work performed in this project, in addition to extended information not included in aforementioned papers.

Quasi two-dimensional experiments were performed in a synthetic porous medium initially filled with a water-rich phase. The model was made of two vertical glass plates with the space between them packed with glass-beads. Models used in experiments represent a homogeneous porous medium where the glass-bead size controlled the permeability of the bead packs. Two sets of fluids were used in the experiments. The system was used for demonstrating the influence of gravitational, viscous and capillary effects on the vertical flow of CO_2. Experiments were described by dimensionless capillary (N_C) and capillary-to-gravity-ratio (R_{CG}) numbers which incorporate fluid and rock properties.

3.1 Model construction

There were two models developed in this project. The first was a 'fixed' one, i.e. the elements were glued together with no possibility to open the model, with the exception of the top side of the model. The opening was used for exchanging the glass-beads. The connectors were permanently fixed to the model and filters made of fabric mesh were glued on the inside of the model. The second model was of more 'flexible'

construction. The glass plates were clamped together with screws and the model could be easily opened and repaired if necessary. Also exchanging glass-beads was much easier to perform. Schematic of the flexible model assembly is shown in Figure 3.1. Dimensions of the glass-bead-filled part of the experimental model are presented in Table 3.1. Note that following description of the model construction and operation would only consider the 'flexible' model.

Table 3.1 ***Dimensions of the glass-bead-filled part of the models.***

	'Flexible' model
Height [cm]	30.44
Width [cm]	30.44
Thickness [cm]	0.260/0.236*
Distance from the inlet to top of the model [cm]	28.00
*) difference due to changes in seal thickness	

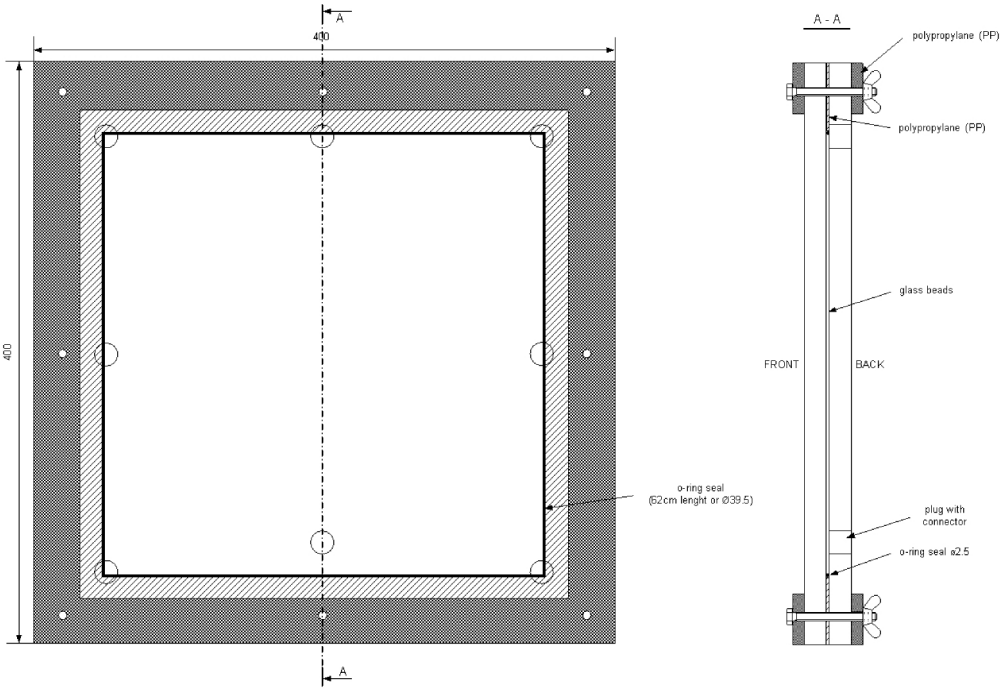

Figure 3.1 ***Schematic of the model assembly.***

The model consisted of two glass plates (400x400x14.5 mm). One of them was the 'front' of the model, with 8 holes (Ø6 mm) for assembly. Another plate was the 'back'

of the model, also with 8 holes used for assembly (Ø6 mm), and 8 larger holes (Ø16 mm) used for installation of tubing connectors. Connectors consisted of the following elements (Figure 3.2):

- Hollow and threaded inside fittings made of PEEK (polyether ether ketone), glued into the large holes in the 'back' panel
- Filters made of stainless steel; 150x150 mesh size; it has large open area and small enough opening to retain the smallest glass-beads used in experiments
- Nitrile O-ring for keeping filter in place and to improve the overall tightness of the connector
- Swagelok connector SS-100-1-OR with sealing O-ring screwed into the fitting.

Between the glass plates there was a polypropylene (PP) frame which was glued to the ‘front’ panel. Thickness of this frame was 2 mm and outer dimensions were equal with glass plates. There were 8 assembly holes (Ø6 mm) corresponding to those in glass plates. Along the inner side of the frame the O-ring (Ø2.62 mm) seal was attached. Additionally, the O-ring was covered with elastic silicone (Würth Silicone Special 180) in order to increase the tightness of the model. External polypropylene frames (8 mm thickness) with 8 assembly holes (Ø6 mm) were installed on both sides of the model and everything was clamped together with screws (M3) covered with silicone tubes for protecting the glass.

One of the connector holes in the corner of the assembled model was left open. The model was then placed on a vibrator table and the glass-beads were poured in through the opened hole. When the filling with beads was completed, the last connector was installed and the model was placed in the model-holding frame.

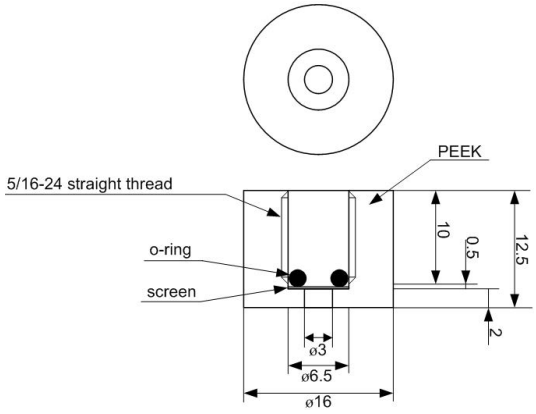

Figure 3.2 Schematic of the fitting.

3.2 Experimental setup

The experimental setup consisted of the following elements:

- 2D cell with the model holder,
- Set of tubing and valves with connectors (Swagelok) used for transporting fluids to and from the model,
- Two syringe pumps used for injecting the fluids into the model,
- Two digital balances used for measuring mass of the injected fluids,
- Digital differential pressure transducer,
- PC with logging program used for data acquisition from connected to it balances, differential pressure transducer, and digital camera,
- Tank with CO_2 used for drying the model after cleaning and for flushing the model before saturating it with water-rich phase.

The schematic of the experimental setup is shown in Figure 3.3, and pictures showing the actual setup are in Figure 3.4.

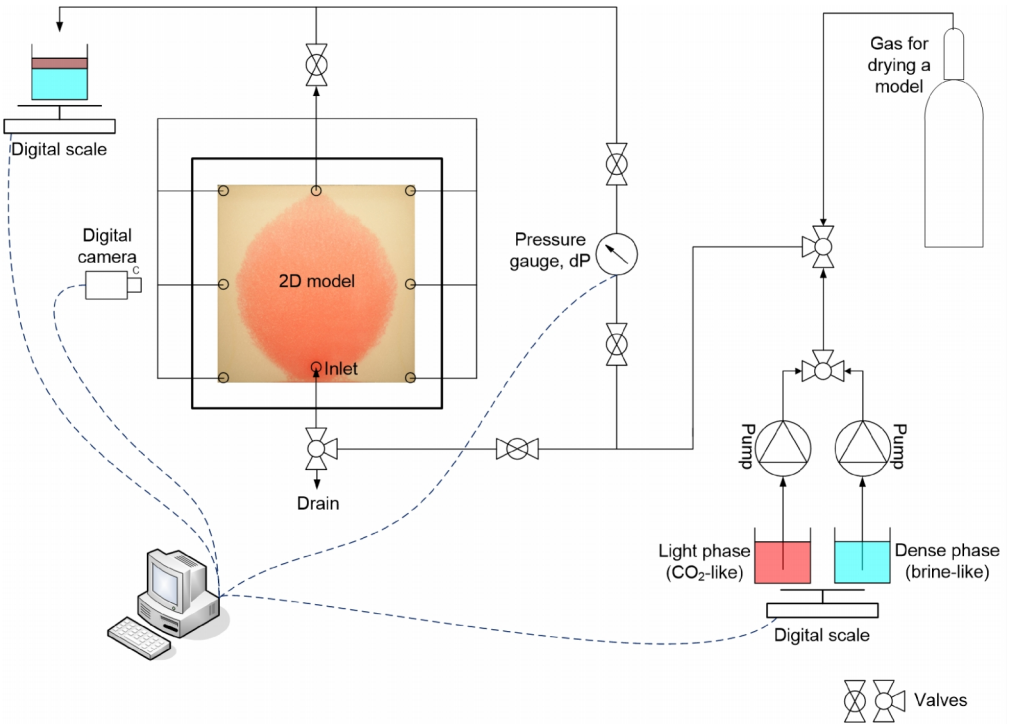

Figure 3.3 Schematic of the experimental setup.

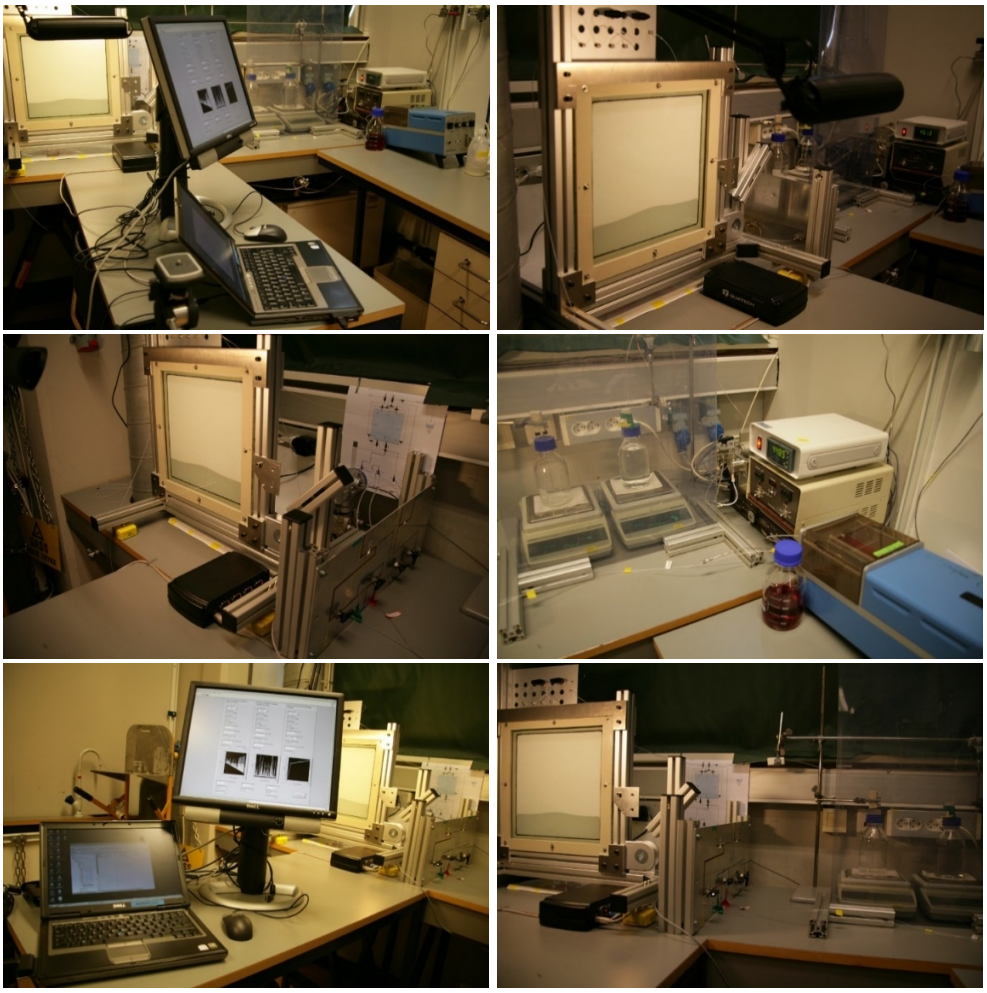

Figure 3.4 Pictures of the experimental setup.

3.2.1 Data acquisition

Data acquisition was performed by a logging program run on a PC to which digital balances and differential pressure transducer were connected. The logging program was developed in graphical programming tool LabVIEW (National Instruments). The software collected readings from instruments at given time intervals. The control panel of the data acquisition software is presented in Figure 3.5 and an example of the output file in Figure 3.6. After the experiments were performed the log files were transformed, analysed, and used for calculations in MATLAB software.

Additionally, a digital camera was used in order to record changes in saturation of the model. Camera was controlled by PC and pictures were taken automatically at given time intervals.

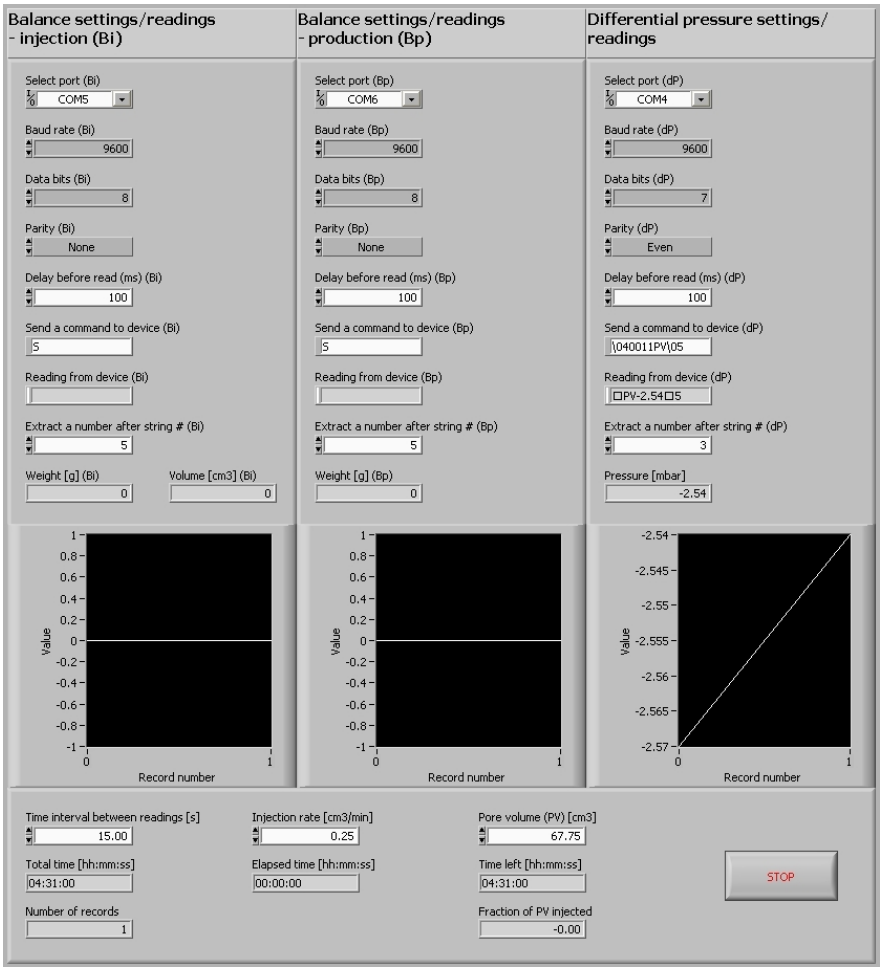

Figure 3.5 Control panel of the logging program developed in LabVIEW.

1	2011-08-08	17:57:59	0.00	6.39	0.03	−0.08
2	2011-08-08	17:58:04	5.00	6.21	0.00	−0.11
3	2011-08-08	17:58:09	10.00	5.98	7.00	−0.12
4	2011-08-08	17:58:14	15.00	5.79	0.10	−0.14
5	2011-08-08	17:58:19	20.00	5.71	0.12	−0.15
6	2011-08-08	17:58:24	25.00	5.63	0.15	7.00
7	2011-08-08	17:58:29	30.00	5.55	0.17	−0.18
8	2011-08-08	17:58:34	35.00	5.55	7.00	−0.19
9	2011-08-08	17:58:39	40.00	5.57	0.00	−0.21
10	2011-08-08	17:58:44	45.00	5.49	0.22	−0.22
11	2011-08-08	17:58:49	50.00	5.38	0.23	−0.24
12	2011-08-08	17:58:54	55.00	5.34	0.24	5.00
13	2011-08-08	17:58:59	60.00	5.28	0.27	−0.26
14	2011-08-08	17:59:04	65.00	5.24	0.00	−0.28
15	2011-08-08	17:59:09	70.00	5.22	0.32	−0.30
16	2011-08-08	17:59:14	75.00	5.23	0.32	−0.31
17	2011-08-08	17:59:19	80.00	5.20	0.35	−0.33
18	2011-08-08	17:59:24	85.00	5.18	0.37	−0.34
19	2011-08-08	17:59:29	90.00	5.20	0.39	−0.35
20	2011-08-08	17:59:34	95.00	5.18	0.40	−0.37
21	2011-08-08	17:59:39	100.00	5.15	0.42	−0.38
22	2011-08-08	17:59:44	105.00	5.18	0.44	−0.40
23	2011-08-08	17:59:49	110.00	5.14	0.45	2.00
24	2011-08-08	17:59:54	115.00	5.11	0.47	−0.43
25	2011-08-08	17:59:59	120.00	5.12	8.00	−0.45
26	2011-08-08	18:00:04	125.00	5.10	0.00	−0.45
27	2011-08-08	18:00:09	130.00	5.07	0.53	−0.47
28	2011-08-08	18:00:14	135.00	5.08	0.56	−0.48
29	2011-08-08	18:00:19	140.00	5.05	0.57	0.00
30	2011-08-08	18:00:24	145.00	5.02	0.59	−0.51
31	2011-08-08	18:00:29	150.00	5.00	1.00	−0.53
32	2011-08-08	18:00:34	155.00	4.98	0.63	−0.55
33	2011-08-08	18:00:39	160.00	4.97	0.65	−0.56
34	2011-08-08	18:00:44	165.00	4.93	0.67	−0.58
35	2011-08-08	18:00:49	170.00	4.88	0.70	−0.59
36	2011-08-08	18:00:54	175.00	4.86	0.72	−0.60
37	2011-08-08	18:00:59	180.00	4.83	0.00	−0.62
38	2011-08-08	18:01:04	185.00	4.83	0.75	−0.63
39	2011-08-08	18:01:09	190.00	4.80	0.75	−0.66
40	2011-08-08	18:01:14	195.00	4.77	0.78	6.00
41	2011-08-08	18:01:19	200.00	4.78	0.80	−0.68
42	2011-08-08	18:01:24	205.00	4.76	2.00	−0.69

Figure 3.6 ***Example of the log file generated by the logging program; columns from 1 to 7 contain respectively: (1) record number, (2) date and (3) time of the experiment, (4) time in seconds from start of experiment (here in 5 s intervals), (5) pressure difference in mbar between inlet and outlet of the model, (6) mass of produced effluent, and (7) mass of injected fluid; the erratic values visible in columns 6 and 7 were amended in MatLab.***

3.2.2 Model preparation prior to the experiment

The model was first saturated with CO_2 and then the water-rich phase was injected. The reason for using CO_2 was that the IFT between CO_2 and injected water-rich phase is lower than between air and water-rich phase, thus the injected fluid displaces gas more efficiently from the pores and avoids creating gas pockets. Also, in case the CO_2 was trapped in pores, it was usually dissolved in brine after short time. Both water-rich phase and non-wetting phase were injected from the bottom-middle hole (inlet) of the model (Figure 3.3). All remaining holes (outlets) were kept open during saturating process and experiments in order to create conditions analogous to an open reservoir.

3.2.3 Model cleaning

After the experiment was finished, the model could be cleaned in two ways depending on the fluid system used in experiment. When high-IFT system was used, the only way to clean the model was by gravity stable displacement of fluids by isopropanol. In case of low-IFT fluid system, the washing could be performed with forcing flow of the brine through the model (pumping) until the non-wetting fluid was removed from the model. This requires larger volume of prepared water-rich fluid but significantly reduces time needed for cleaning. However, after 2-3 experiments, air bubbles started to form in the model and thorough cleaning with isopropanol was necessary. After washing the model, it was drained of isopropanol and dried by letting CO_2 through the model.

3.2.4 Operational difficulties

During normal use of the model in the experiments special care had to be taken when exchanging the glass-beads. Disassembling the model, removing of glass-beads, cleaning, and re-assembling, had to be done very carefully in order to avoid fracturing the glass plates. Clamping the model with screws requires use of a special spanner which can control torque, so each screw is fastened with the same force.

When filling in the model with glass-beads, it was important to vibrate it for sufficiently long time, in order to pack it tightly enough to prevent dropping down the beads during experiments. Beads settle during saturating the model with fluids and this can create a gap at the top of the model. In such a case, more beads had to be added to the model.

The cleaning of the model can also cause difficulties. When the injected fluids are volatile and the model is cleaned with brine, gas bubbles may be created. When such situation occur, the model must be washed with isopropanol, drained, dried and saturated again before new experiment could be performed.

It should also be noted that preferential flow paths could be created along the boundaries of the model due to slightly higher permeability. Sometimes during experiments, often after the breakthrough, part of the injected fluid flowed along boundaries. It was an issue especially in attempts to perform the high-IFT, low-k cases. Such fluid behaviour could slightly affect the displacement patterns but had no influence on the results of the experiments and final calculations.

3.3 Properties of the porous medium

3.3.1 Porosity

The porous medium of the model consisted of regular soda-lime glass-beads. Both mono-dispersed and range sizes were used in experiments (Table 3.2). Porosity of the model was calculated in each experiment by measuring volume of the injected dense fluid and subtracting it from the volume of the model. Porosity (Table 3.2) and thus pore volume measurements were carried out each time the model was re-packed and re-saturated.

Table 3.2 Average porosity measured for a given glass-beads diameter.

Glass-beads diameter, d_b [micron]	Porosity
200	0.390
180-250	0.394
300-400	0.388
400	0.390

3.3.2 Permeability

The size of the glass-bead used in experiments controlled the permeability (k) of the model. The theoretical values of the permeability for each glass-bead size range used in experiments were calculated with both Rumpf and Gupte equation (R-G) (Equation 3.1) (Rumpf and Gupte 1975) and Kozeny-Carman equation (K-C) (Equation 3.2) (Kaviany 1995):

$$k = \frac{\phi^{5.5}}{5.6} d_b^2$$

Equation 3.1

$$k = \frac{\phi^3}{180(1-\phi)^2} d_b^2$$

Equation 3.2

where: k – permeability, m^2; ϕ – porosity; d_b – glass-bead diameter, m.

In order to verify calculated values, the permeability was also measured experimentally and calculated according to Darcy's flow equation (Equation 3.3):

$$k = \frac{q\mu L}{A\Delta p}$$

Equation 3.3

where: k – permeability, m^2; q – flow rate, m^3/s; μ – fluid viscosity, Pa·s; L – glass bead pack length, m; A – pack's cross section surface area, m^2; Δp – pressure drop measured along the pack, Pa.

Values of calculated and measured permeability are summarized in Table 3.3. Note that permeability values are given in Darcy unit (D), where 1 D = $1 \cdot 10^{-12}$ m^2.

Permeability measurement setup is presented in Figure 3.7. The setup consisted of glass-bead pack (black tube in Figure 3.7), syringe pump, and differential pressure transducer. The length of the pack was approximately 0.51 m and its cross section surface area of 0.0387 m^2. Distilled water was used in all measurements. The viscosity of water at laboratory conditions (temperature of approx. 20°C) was $1.002 \cdot 10^{-3}$ Pa·s.

Table 3.3 Calculated and measured permeability values of the glass beads used in experiments.

Glass-beads diameter, d_b [micron]	Average glass bead diameter used in calculations, d_b [micron]	Permeability for average glass bead diameter, (R-G) equation, k [D]	Permeability for average glass bead diameter, (K-C) equation, k [D]	Permeability measured in laboratory experiment, k [D]
200	200	40.2	34.5	15.6
180-250	215	46.5	40.9	28.9
300-400	350	123.3	108.5	75.1
400	400	161	141.7	-*

*) **Measurement for 400 micron was not performed due to insufficient volume of the glass beads available to conduct a reliable experiment.**

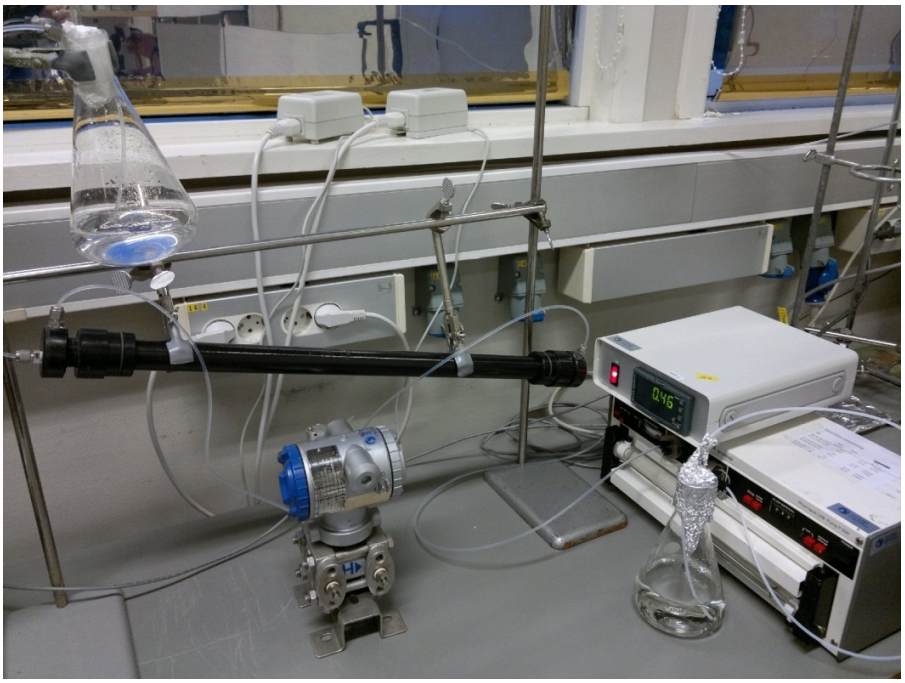

Figure 3.7 ***Laboratory setup used for permeability measurements (glass-bead pack, syringe pump, and differential pressure transducer).***

All further calculations are based on the permeability values calculated according to K-C equation. The reason for choosing K-C values is that they fall in between measured in 1D model (minimum) and R-G (maximum) calculated values of permeability. Lower value of the permeability measured in the laboratory is considered too low for the conditions present in the experimental 2D model. Glass-bead pack used for measuring permeability was much thicker than bead layer in the 2D model and thus the 'wall-effect' influence on fluid flow was significantly lower on the final permeability.

3.4 Fluid systems

There were two sets of the fluids used in experiments. The first set was a mixture of distilled water, glycerol, and n-heptane (Cinar et al. 2009). The second set was a mixture of 2% solution of $CaCl_2$ (brine), isopropanol, and isooctane (Schechter et al. 1991; Holt and Vassenden 1996). At ambient conditions both mixtures separate into two phases:

1) water-rich, dense and more viscous phase which in experiments represents reservoir brine, and
2) hydrocarbon-rich, lighter and less viscous phase which in experiments represents CO_2.

The hydrocarbon-rich phase was dyed red with Sudan IV dye and the water-rich phase had no dye added.

The first set of fluids is characterised by high density difference (476 kg/m^3) and high IFT value (34 mN/m) (high-IFT system). Its properties were analogous to the properties of the CO_2 and brine at possible reservoir conditions. The analogy was made based on the comparison of the density difference, viscosity ratios, and IFT values which all were within a range of values measured for CO_2 and brine at reservoir conditions (Nordbotten et al. 2005; Bennion and Bachu 2006a; Michael et al. 2009).

The second set of fluids characterises lower density difference (206 kg/m^3) and low IFT (1 mN/m) (low-IFT system). The advantage of these fluids was reduced entry pressure for the injected fluid. Detailed composition and properties of fluid systems used in experiments are presented in Table 3.4. Fluids' properties were measured with help of following instruments:

- density with Anton Paar DMA46 densimeter,
- viscosity with Ubbelohde viscometer,
- IFT with Du Noüy type ring tensiometer.

Table 3.4 Composition and properties of fluids used in experiments (table from Paper IV).

System	Composition	Phases	Density, kg/m^3	Density difference, kg/m^3	Viscosity, mPa·s	Viscosity ratio	IFT, mN/m
High IFT	distilled water (23 wt%) glycerol (44 wt%) n-heptane (33 wt%)	glycerol-rich phase (BRINE)	1160.4	475.9	12.557	30.8	34.0
		n-heptane-rich phase (CO_2)	684.5		0.408		
Low IFT	2% $CaCl_2$ brine (29.1 wt%) isopropanol (34.3 wt%) isooctane (36.6 wt%)	water-rich phase (BRINE)	903.1	205.6	3.556	6.4	1.0
		isooctane-rich phase (CO_2)	697.5		0.556		

3.5 Experiments

The glass-bead model was initially saturated with the denser fluid representing brine. The red-dyed, lower density fluid, representing CO_2, was injected from the bottom of the model using a piston pump. Fluid was injected at a constant rate in every experiment until it reached the top of the model. In some cases injection time was extended in order to see how displacement patterns were changing during longer injection periods. Injection time corresponded to the fraction of the model's pore volume (PV) injected and varies between 0.25 and 1.00 PV. All experiments were performed at ambient conditions. For a given fluid system only permeability (k) and injection rate (q) were varied and all the other parameters were kept constant. The flow velocities observed in experiments were within the range of 0.26-1.29 m/day which corresponds to the flow velocities observed during CO_2 storage processes in real reservoirs (Berg and Ott 2012). In order to represent flow in an open reservoir, the outlets located at the edges of the model were open during the experiments and thus injected fluid could displace the brine in all directions available in the 2D-model. Following parameters were recorded during the experiments:

- injection pressure,
- mass of the injected and produced fluids,
- time when injected fluid reached the top of the model,
- time when injected fluid left the model,
- pictures were taken during the experiments in order to visualize the changes in saturations.

Table 3.5 lists combinations of parameters in different cases investigated in the experiments. There were in total 11 cases investigated in laboratory and each case was attempted between two to four times depending on the results repeatability, i.e. if the results from two attempts of the same case were consistent, there were no more attempts of this case made. In this work averaged results of each case are presented. Note that one case – the high-IFT, low-k, high-q (1C) – was not performed due to the high pressure increase which could have caused the model to burst. This case, however, was included in the numerical modelling. Results of the experiments and calculations for high-IFT system were partly described in Paper II (Polak et al. 2011) and more comprehensive study of experiments and simulations in both low- and high-IFT systems is presented in Paper IV.

Table 3.5 Sets of experimental cases with parameters used in calculations (table from Paper IV).

Case	Case description	IFT, mN/m	Glass bead diameter, d_b, micron	Permeability, K-C equation, k, D	Porosity, ø	Injection rate, q, cm^3/min
1A	high-IFT, low-k, low-q	34	200	34.5	0.390	0.10
1B	high-IFT, low-k, mid-q	34	200	34.5	0.390	0.25
1C*	high-IFT, low-k, high-q	34	200	34.5	0.390	0.50
2A	high-IFT, high-k, low-q	34	400	141.7	0.390	0.10
2B	high-IFT, high-k, mid-q	34	400	141.7	0.390	0.25
2C	high-IFT, high-k, high-q	34	400	141.7	0.390	0.50
3A	low-IFT, low-k, low-q	1	180-250	40.9	0.394	0.10
3B	low-IFT, low-k, mid-q	1	180-250	40.9	0.394	0.25
3C	low-IFT, low-k, high-q	1	180-250	40.9	0.394	0.50
4A	low-IFT, high-k, low-q	1	300-400	108.5	0.388	0.10
4B	low-IFT, high-k, mid-q	1	300-400	108.5	0.388	0.25
4C	low-IFT, high-k, high-q	1	300-400	108.5	0.388	0.50
***) simulation only**						

3.5.1 Observations in experiments

Changes in fluid saturation in the model during injection of low density fluid (model-CO_2) are shown in Figure 3.8 to Figure 3.12. Pictures presented here were taken after injection of 0.010, 0.025, 0.050, 0.100, 0.150, 0.250 PV (Figure 3.8 to Figure 3.11), and at the moment of breakthrough (Figure 3.12). The breakthrough was assumed to take place when injected fluid reached the top and started leaving the model. Note that it is not straightforward to see a magnitude of the saturation by inspection of the pictures due to their resolution. The averaged values of 'brine' displacement after injection of 0.010, 0.025, 0.050, 0.100, 0.250, 0.300 PV are shown in Figure 3.13.

At low injection rates the plume of the injected fluid was narrowest. This was due to the gravity effects which were more pronounced in such cases (Figure 3.8 to Figure 3.11, cases 1A, 2A, 3A, and 4A). Density difference between fluids caused that injected one (lighter, thus more buoyant) flowed more in the vertical direction. As a result, less volume of the in-situ fluid was displaced compared to the mid- and high-q cases (see Figure 3.13 at 0.300 PV injected).

When the injection rate was raised, the impact of viscous forces increased, resulting in wider plume and growing recovery (Figure 3.8 to Figure 3.11, cases 1B, 1C, 2B, 2C, 3B, 3C, 4B, and 4C; recovery in Figure 3.13). Comparing results from cases with the same injection rate but different permeability it becomes apparent that

higher sweep efficiency in the displaced area is at low-k. This results in wider plume than in high-k cases (Figure 3.8 to Figure 3.11, cases 1 vs. 2, and 3 vs. 4).

Capillary forces dominate the flow of injected fluid at high value of IFT what is expressed by channelling. The plume's lateral extent is smaller than in low-IFT cases and the displacement front is significantly more bifurcated (Figure 3.8 to Figure 3.11, cases 1 and 2 vs. 3 and 4). Consequently, a large part of the brine was bypassed resulting in an early breakthrough and lower recovery than in corresponding cases with low-IFT fluid system (see Figure 3.13). After the breakthrough at high-IFT system, injected fluid flowed through the channels which were formed prior to the breakthrough and no further noticeable changes in saturation could be observed (Figure 3.8 to Figure 3.9).

More details regarding description of the results from laboratory experiments and thorough discussion are presented in Paper IV.

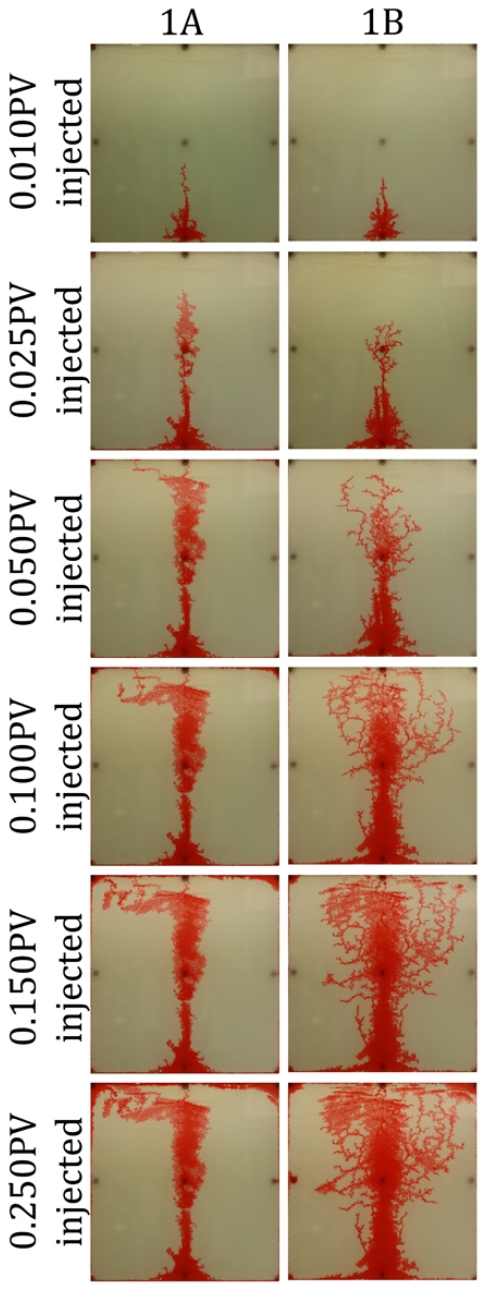

Figure 3.8 ***Examples of saturation maps at various steps of PV of 'CO₂' injected in high-IFT and low-k cases; figures are representative for experiments within each case.***

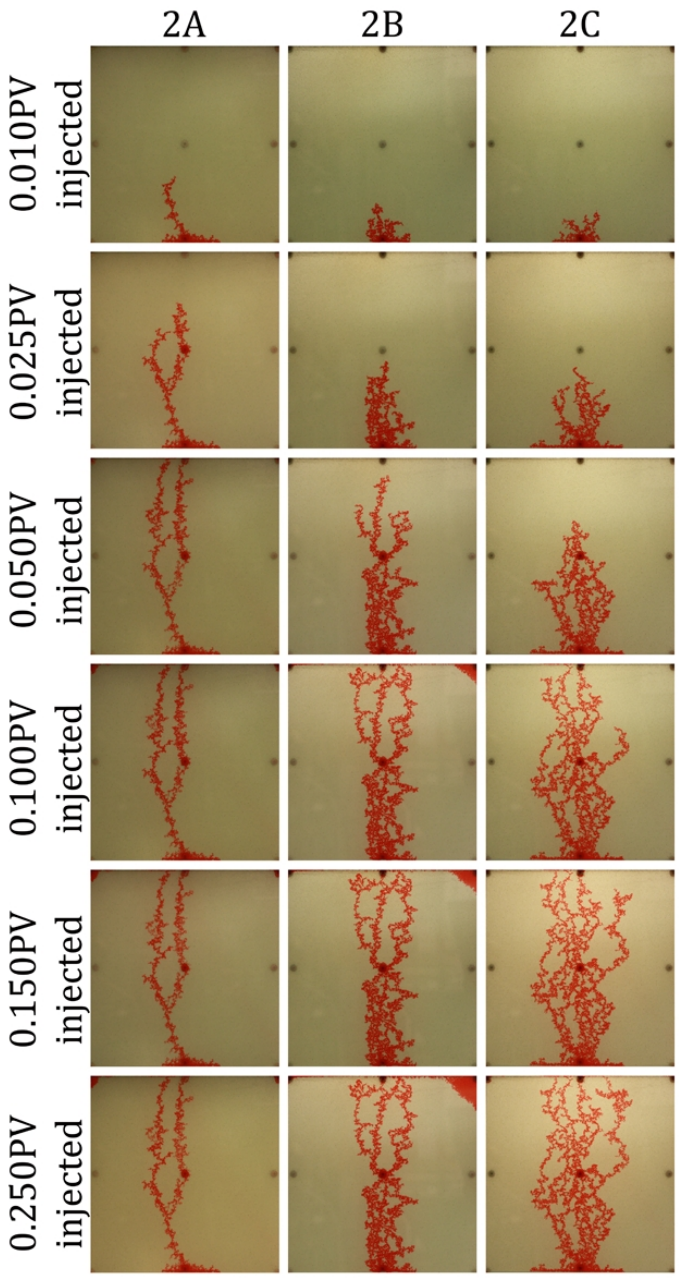

Figure 3.9 ***Examples of saturation maps at various steps of PV of 'CO₂' injected in high-IFT and high-k cases; figures are representative for experiments within each case.***

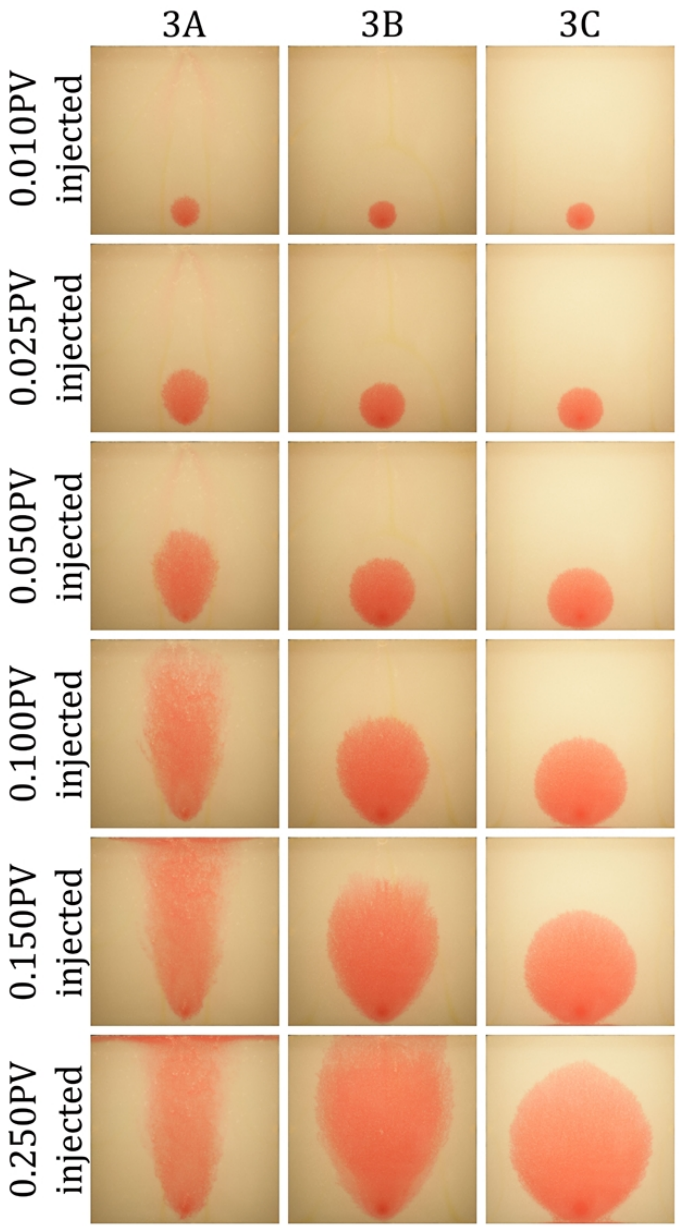

Figure 3.10 Examples of saturation maps at various steps of PV of 'CO_2' injected in low-IFT and low-k cases; figures are representative for experiments within each case.

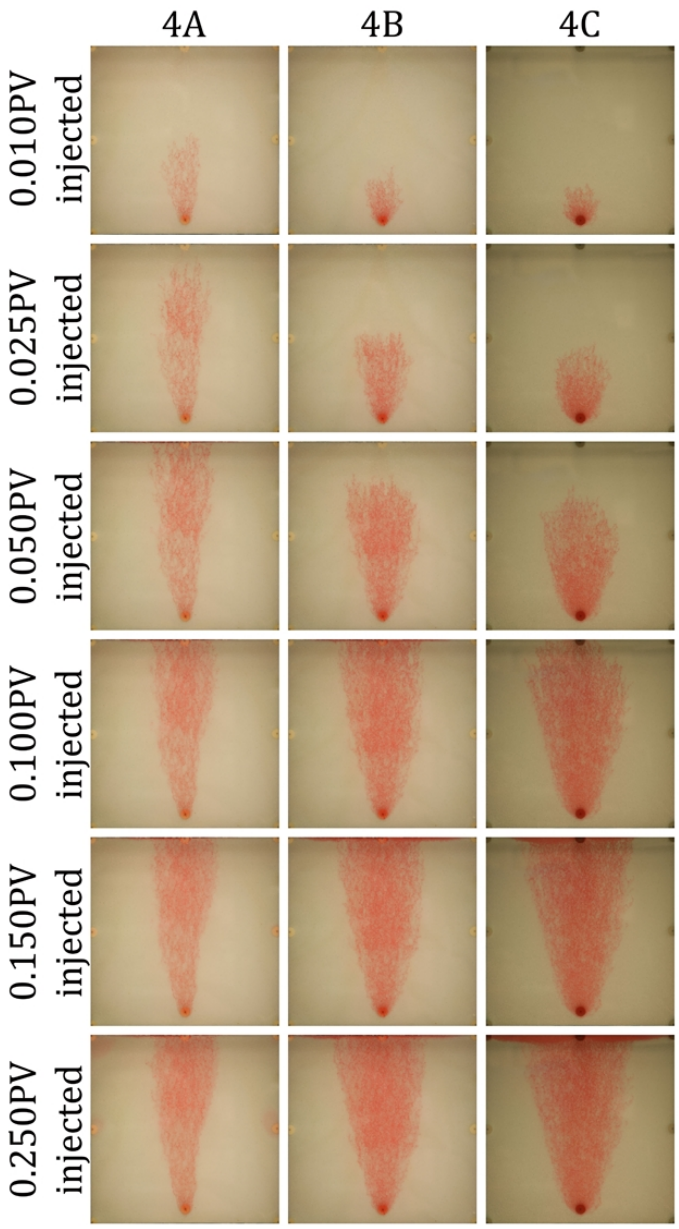

Figure 3.11 ***Examples of saturation maps at various steps of PV of 'CO₂' injected in low-IFT and high-k cases; figures are representative for experiments within each case.***

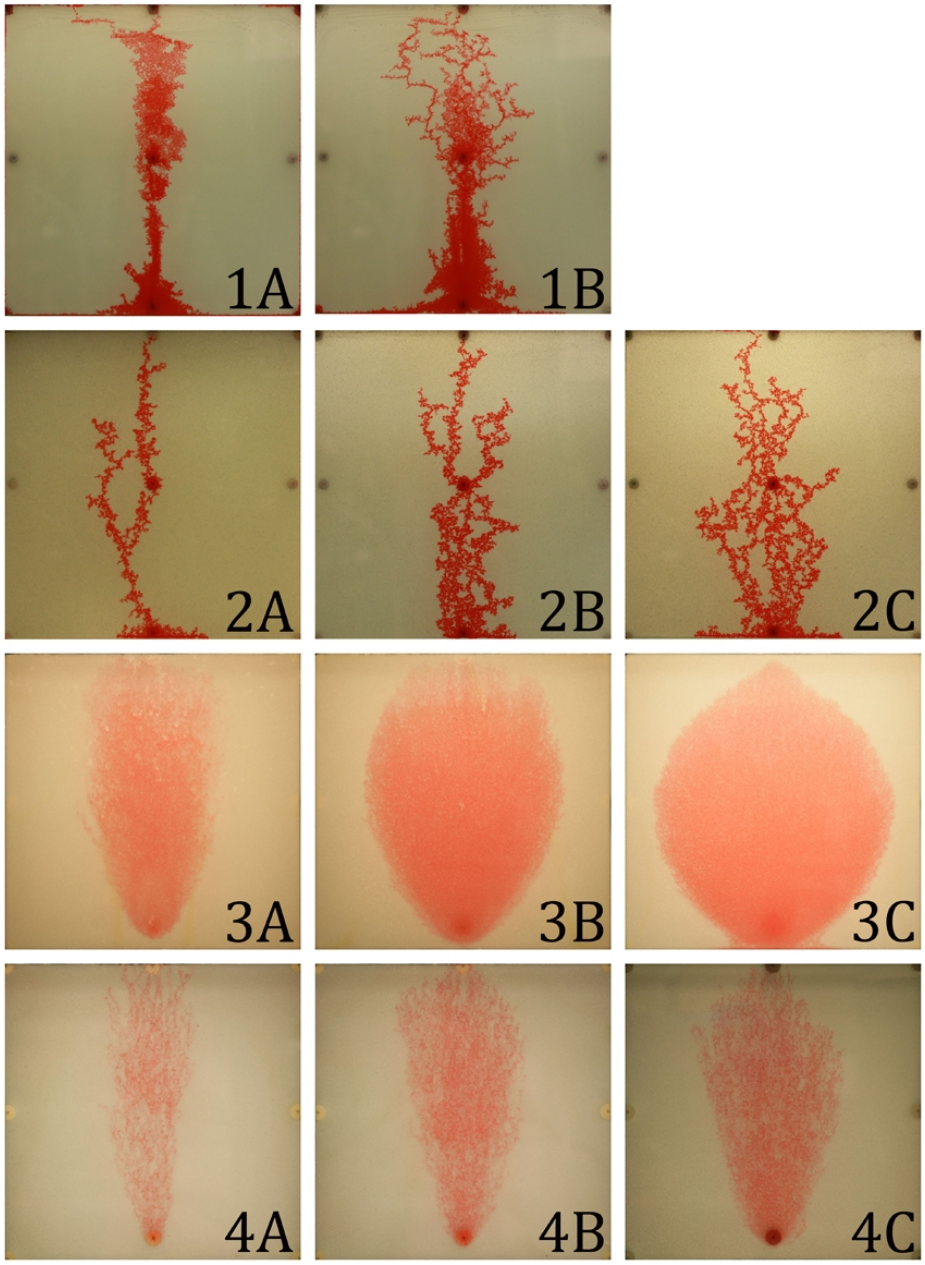

Figure 3.12 Examples of saturation maps at the breakthrough; figures are representative for experiments within each case.

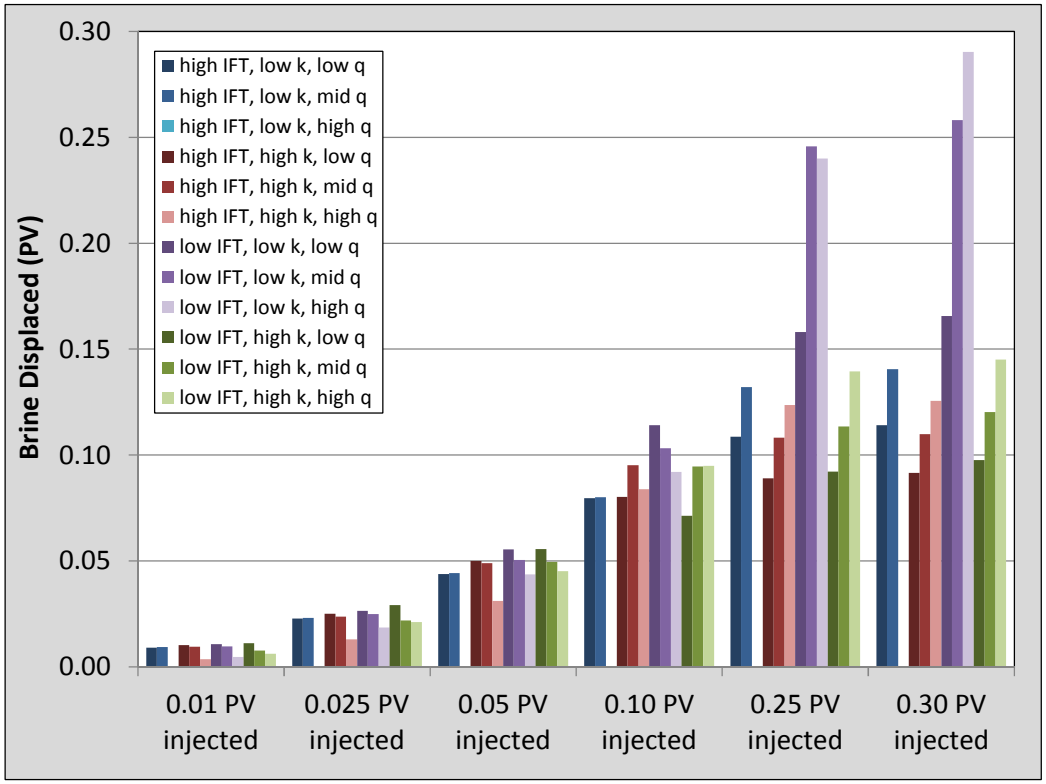

Figure 3.13 'Brine' displacement in experiments (averaged values).

3.5.2 Scaling of the experiments and field cases

Flow regimes occurring when CO_2 is injected into a deep geological formation control how much CO_2 can be effectively injected and stored in the formation. Reservoir parameters such as depth, temperature, permeability and capillary pressure have great influence on CO_2 flow within a reservoir. In order to compare results of the experiments with the field cases, two scaling parameters were used: capillary number (N_C) and capillary-to-gravity-ratio (R_{CG}). These dimensionless numbers incorporate fluid and rock properties. R_{CG} and N_C were calculated for both the experiments and field cases. The input parameters for calculation of scaling numbers for sedimentary basins, existing and planned storage sites, and test sites were obtained from the scientific literature. In case of experiments, for a given fluid system, only permeability and flow velocity controlled the dimensionless parameters. The range of the flow velocities (from 0.26 to 1.29 m/day) used in calculations for storage sites, was assumed

to be the same as in the laboratory experiments. Results of this analysis were first presented in Polak et al. (2011) (Paper II), and here they are revised and extended.

The capillary number, N_C, is defined as a ratio of viscous to capillary forces:

$$N_C = \frac{u \cdot \mu_i}{\gamma}$$

Equation 3.4

where: u – Darcy's flow velocity, m/s, defined as u=q/A, with q being injection rate, m^3/s, and A being the cross-sectional area of the model, m^2; μ_i – viscosity of the injected fluid, Pa·s; γ – interfacial tension (IFT), N/m.

The IFT (if not given) is calculated according to the equation (*Equation 3.5*) (Bennion and Bachu 2006b):

$$\gamma = \frac{59.335}{P^{0.2446}}$$

Equation 3.5

where: γ – IFT, mN/m; P – formation pressure, MPa.

The capillary to gravity force ratio, R_{CG}, (Holt and Vassenden 1996) is defined as:

$$R_{CG} = \frac{2\gamma}{\Delta\rho \cdot g \cdot h \cdot \sqrt{\frac{k}{\phi}}}$$

Equation 3.6

where: Δρ – density difference of the fluids, kg/m^3; g – acceleration of gravity, m/s^2; h – distance between model's inlet and outlet or formation thickness in the reservoir, m.

As N_C is a ratio of viscous to capillary forces and R_{CG} is a ratio of capillary to gravity forces, then $R_{CG} \cdot N_C$ is a ratio of viscous to gravity forces (R_{VG}). The R_{VG} is proposed because together with N_C clearly presents the direction of forces acting on the flow of the injected fluid into experimental model or reservoir. Parameters calculated for experiments are presented in Table 3.6. Forces acting on the fluid flow and location of the experiments in the N_C-R_{VG} space are presented in Figure 3.14.

Table 3.6 Calculated dimensionless parameters for experiments (table from Paper IV).

Case	$N_C \cdot 10^{-3}$	$R_{VG} \cdot 10^{-3}$
1A	0.0642	0.3316
1B	0.1605	0.8291
1C*	0.3210	1.6581
2A	0.0642	0.1658
2B	0.1605	0.4144
2C	0.3210	0.8288
3A	1.4794	0.5142
3B	3.6985	1.2856
3C	7.3970	2.5711
4A	1.4794	0.3133
4B	3.6985	0.7833
4C	7.3970	1.5665
*) simulation only		

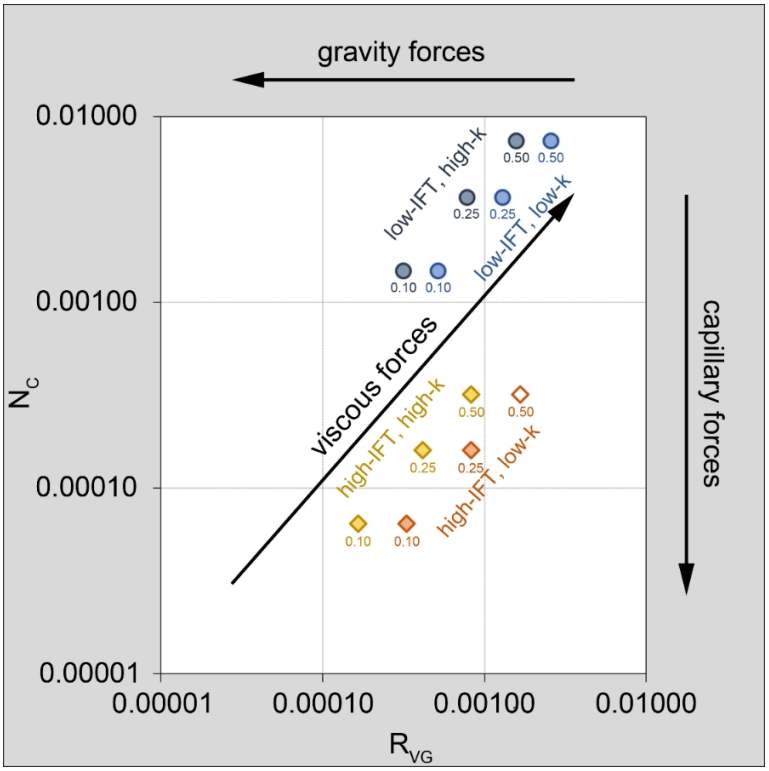

Figure 3.14 Experiments in N_C-R_{VG} space; distribution of the forces acting on the fluid flow in experiments; each case is marked with the injection rate value (cm^3/min); empty marker in high-IFT, low-k cases indicates an experiment which was not performed but for which simulation was made (figure from Paper IV).

The input parameters for sedimentary basins were obtained from Nordbotten et al. (2005). The authors provided eight sets of properties based on following parameters: depth (1000 and 3000 m, and pressure gradient of 10.5 MPa/km), temperature (gradient of 25 and 45 °C/km), and brine salinity. These properties determine the conditions in the reservoir formations and thus CO_2 viscosity and density, and IFTs. The generic storage formation in this study is assumed to have porosity of 15 %, permeability of 20 mD, and thickness of 30 m. Additionally, N_C and R_{VG} numbers were calculated for basins thickness of 100 and 200 m.

Parameters used in calculations of dimensionless numbers for existing or planned storage sites (Sleipner, Snøhvit, In Salah, and Gorgon) and for existing test sites (Nagaoka and Ketzin) are obtained from Michael et al. (2009), Pamukcu et al. (2011) and Gor and Prévost (2013). Remaining data was obtained from Bakk et al. (2012) for CO_2FieldLab, and from Braathen et al. (2012) for Longyearbyen CO_2 Lab project.

Some of the input parameters and results of calculations are listed in Table 3.7 and Table 3.8. One of the important parameters with significant influence on scaling of reservoirs was the vertical permeability value. Unlike in laboratory model, where the vertical permeability (k_v) equals horizontal permeability (k_h), in real reservoirs, k_v is usually a fraction of k_h, ranging typically between 0.10 and 0.01. In cases where k_v value for specific reservoir was not provided in the literature, the 0.10 factor was used in order to calculate k_v ($k_v = 0.1 \cdot k_h$). For calculations of CO_2 and brine densities and CO_2 viscosity in reservoir conditions, an Excel macro containing set of appropriate formulas has been used. This macro has been developed at SINTEF Petroleum AS by Lindeberg (2013). Calculations of the brine density are based on Spivey et al. (2004), the CO_2 density on Span and Wagner (1996), and viscosity of CO_2 on Fenghour et al. (1998). Dimensionless numbers calculated for field cases are listed in Table 3.9.

Figure 3.15 shows results of calculations of N_C and R_{VG} numbers for the experiments and field cases, and also forces that govern fluid flow in the reservoir and direction of their increasing importance. Here, the reason for using R_{VG} parameter is clearly visible, as it helps to show in better way the influence of the forces governing a flow in porous media. As could be expected from results of experiments, the high permeability would correlate with higher gravity forces. It can be seen in case of the Sleipner storage site (Figure 3.15) that gravity forces have significant influence on the flow of CO_2 due to reservoir's high permeability (~5 D). The same relation can be observed in case of Ketzin and CO_2FieldLab. The Longyearbyen CO_2 Lab looks to be close to the cases mentioned earlier but it has relatively low permeability. The reason for it is that the formation has relatively low temperature and pressure, approx. 25°C and 46 bar, respectively (Braathen et al. 2012). At these conditions CO_2 will be in

gaseous phase (see Figure 2.2) and therefore significantly less dense than brine. In such conditions influence of gravity forces will become more visible. Also, the IFT in such conditions will be high, what indicates stronger influence of capillary forces.

On the contrary to field cases, the laboratory experiments are dominated by viscous forces, especially those at low IFT. Nevertheless, the experimental N_C and R_{VG} numbers at high IFT and low injection rate agree reasonably well with calculations for some of the sedimentary basins and storage sites. Unfortunately, results showed that low-IFT experiments scale far off the field cases. However, one has to keep in mind that all calculations presented here are made for the same flow velocities as in experiments, and they are relatively low. This range of flow velocity is expected to occur in the reservoir far from the injection point. Further away from the injection point flow velocity is low and gravity forces are stronger (Taku Ide et al. 2007). The flow velocities in experiments are low and correspond to the flow in the field distant to the injection point. In the field case flow velocity would vary, depending on a distance from the injection well, and close to the well would be much higher. High flow velocity would shift calculated results in a direction of stronger viscous forces, the region where laboratory experiments are currently placed in Figure 3.15.

This scaling analysis highlights the importance of the various parameters on the process of site characterisation for CO_2 storage. For example, high permeability and porosity may seem at first as preferred conditions. However, if this does not come together with conditions at which CO_2 is in supercritical state (i.e. appropriate pressure and temperature), the storage capacity of the site could be limited. Representation of the reservoir conditions by means of the dimensionless scaling provides possibility of comparing various storage sites and predicting the flow regimes that may occur when CO_2 is injected.

Table 3.7 ***Parameters used in calculations of the dimensionless numbers for existing and planned storage sites.***

Project/ formation name	Location	Depth, m	Pressure, bar	Porosity	Permeability, mD	Thickness, m
Sleipner	North Sea, Norway	1000	103	0.37	5000	250
In Salah	Krechba, Algeria	1850	175	0.20	5	29
Snøhvit	Barents Sea, Norway	2550	285	0.13	450	60
Gorgon	Barrow Isl., WA, Australia	2300	220	0.20	25	200
Nagaoka	Nagaoka City, Japan	1100	119	0.25	6	60
Ketzin	Brandenburg, Germany	650	73	0.23	750	80
Longyearbyen CO_2 Lab	Svalbard, Norway	670	46	0.18	2	200
CO_2FieldLab	Svelvik, Norway	30	2	0.35	2000	30

Table 3.8 ***Parameters used in calculations of the dimensionless parameters for generic storage sites (based on Nordbotten et al. (2005)).***

Basin type	Depth, m	Pressure, bar	Porosity	Permeability, mD	Thickness, m
shallow, cold, low salinity	1000	10.50	0.15	20.00	30, 100, 200
shallow, cold, high salinity	1000	10.50	0.15	20.00	30, 100, 200
shallow, warm, low salinity	1000	10.50	0.15	20.00	30, 100, 200
shallow, warm, high salinity	1000	10.50	0.15	20.00	30, 100, 200
deep, cold, low salinity	3000	31.50	0.15	20.00	30, 100, 200
deep, cold, high salinity	3000	31.50	0.15	20.00	30, 100, 200
deep, warm, low salinity	3000	31.50	0.15	20.00	30, 100, 200
deep, warm, high salinity	3000	31.50	0.15	20.00	30, 100, 200

Table 3.9 ***Calculated dimensionless parameters for experiments (only for highest flow velocity from experiments - 1.29 m/day).***

	Storage site	N_C	R_{VG}
1	Sleipner	1.24E-05	9.01E-07
2	In Salah	1.65E-05	1.08E-04
3	Snøhvit	1.92E-05	7.32E-06
4	Gorgon	1.79E-05	1.03E-05
5	Nagaoka	1.29E-05	6.47E-05
6	Ketzin	1.13E-05	1.99E-06
7	Longyearbyen CO_2 Lab	3.17E-06	1.34E-05
8	CO_2FieldLab	4.21E-06	3.33E-06
9	shallow, cold, low salinity, 30 m	4.62E-05	3.05E-04
10	shallow, cold, high salinity, 30 m	4.62E-05	1.76E-04
11	shallow, warm, low salinity, 30 m	1.84E-05	4.95E-05
12	shallow, warm, high salinity, 30 m	1.84E-05	3.84E-05
13	deep, cold, low salinity, 30 m	6.41E-05	3.67E-04
14	deep, cold, high salinity, 30 m	6.41E-05	2.05E-04
15	deep, warm, low salinity, 30 m	4.14E-05	1.33E-04
16	deep, warm, high salinity, 30 m	4.14E-05	9.34E-05
17	shallow, cold, low salinity, 100 m	4.62E-05	9.15E-05
18	shallow, cold, high salinity, 100 m	4.62E-05	5.28E-05
19	shallow, warm, low salinity, 100 m	1.84E-05	1.48E-05
20	shallow, warm, high salinity, 100 m	1.84E-05	1.15E-05
21	deep, cold, low salinity, 100 m	6.41E-05	1.10E-04
22	deep, cold, high salinity, 100 m	6.41E-05	6.15E-05
23	deep, warm, low salinity, 100 m	4.14E-05	4.00E-05
24	deep, warm, high salinity, 100 m	4.14E-05	2.80E-05
25	shallow, cold, low salinity, 200 m	4.62E-05	4.57E-05
26	shallow, cold, high salinity, 200 m	4.62E-05	2.64E-05
27	shallow, warm, low salinity, 200 m	1.84E-05	7.42E-06
28	shallow, warm, high salinity, 200 m	1.84E-05	5.75E-06
29	deep, cold, low salinity, 200 m	6.41E-05	5.51E-05
30	deep, cold, high salinity, 200 m	6.41E-05	3.08E-05
31	deep, warm, low salinity, 200 m	4.14E-05	2.00E-05
32	deep, warm, high salinity, 200 m	4.14E-05	1.40E-05

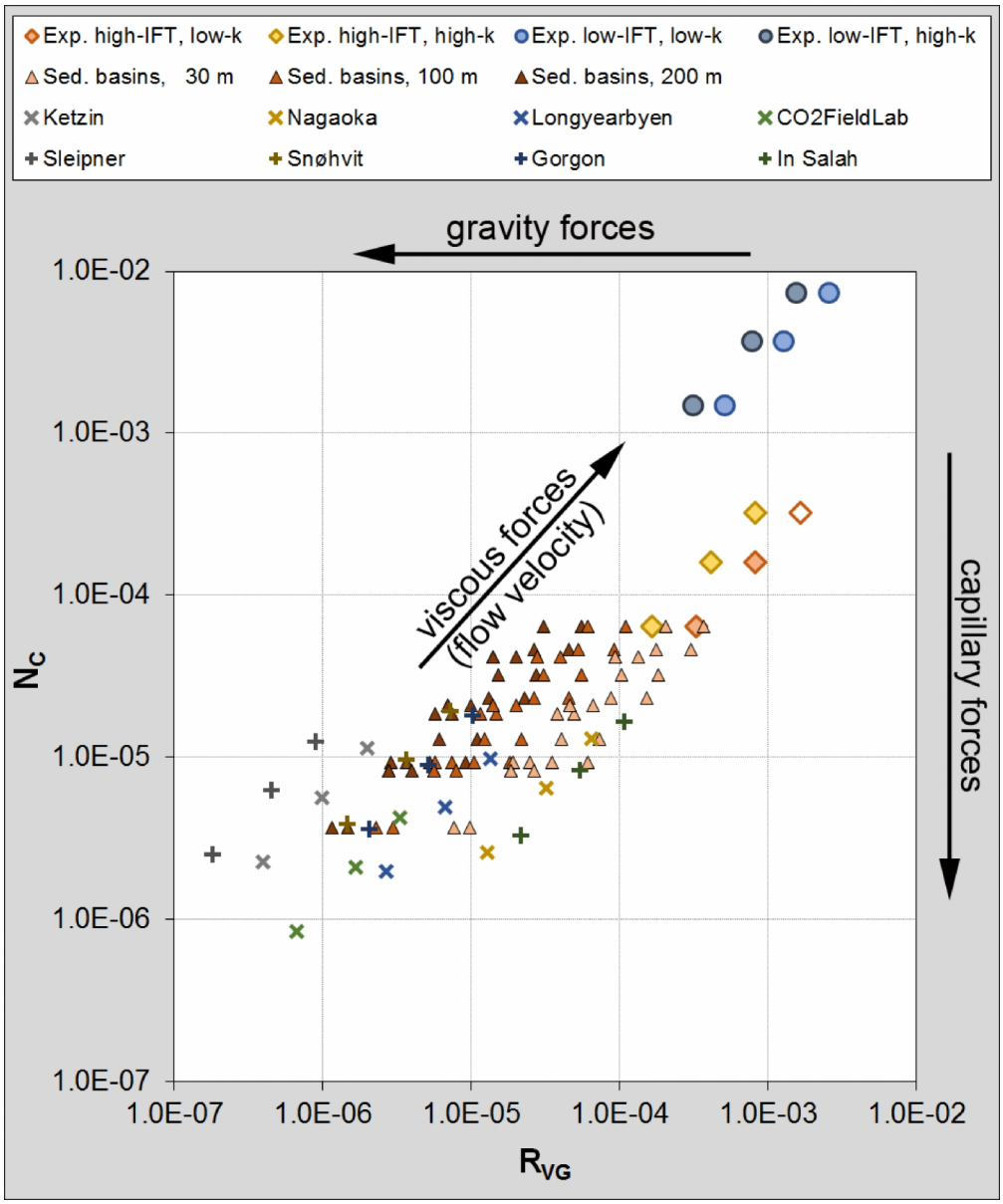

Figure 3.15 ***Representation of the experimental and field data in N_C-R_{VG} space and distribution of the forces acting on the fluid flow; direction of the increasing flow velocity is also indicated; note that calculations are made for the same flow velocities as in experiments; for simplicity all generic sedimentary basins are grouped according to their thickness.***

3.6 Simulations

Thorough description of simulations of laboratory experiments is presented in the Paper IV. In this chapter additional information and sensitivities are presented.

3.6.1 Grid properties in high-IFT simulations

Numerical modelling of the high-IFT cases was challenging. The flow channels, created in experiments by injected fluid, were difficult to reproduce in simulations. Modelling of these cases was approached in following ways:

1) simple simulation grid with no modifications,
2) introduction of randomly distributed high-permeable grid-blocks in the grid,
3) introduction of randomly distributed low-permeable grid-blocks in the grid,
4) introduction of randomly distributed impermeable micro-barriers in the grid.

A comparison of simulation results for two examples of simulations (case 1B – high-IFT, low-k, mid-q, and case 2B – high-IFT, high-k, mid-q) is shown in Figure 3.16 and Figure 3.17. The simulation input was the same in all cases except grid properties that were modified.

Figure 3.16 and Figure 3.17 reveal that simulations where the grid properties were not altered, the shape of the injection plume does not resemble the one from the experiments.

In the cases where randomly distributed high-permeable grid-blocks were introduced 5% of the grid-blocks were affected. These grid-blocks had permeability of 10^9 mD. This value was high, but it was necessary to highlight difference between these grid-blocks and the regular ones. As can be noticed in Figure 3.16 and Figure 3.17, these simulations produced plumes with more irregular shapes. Although it was step in the right direction, further increase in permeability did not bring any significant improvement and did not create distinct flow channels.

The next tested option was introduction of randomly distributed low-permeable grid-blocks. In the cases presented in Figure 3.16 and Figure 3.17 5% of the grid-blocks had permeability set to 10 mD. Results of simulations showed injection plume which was irregular in shape with clearly visible flow channels, especially at the earlier time of injection. Later, these channels were inhibited in the plume and the shape of plume itself was smoothened. Although the injection plume in these simulations was too wide, especially in the lower part, and the plume was to slow to reach the top of the model on time, these results were much more promising than in two previously tested approaches. The negative side of this type of grid modification is that it is very unlikely to observe such low permeability values in the experimental model. Also,

grid-blocks with very low permeability will store very little or no injected fluid and this will reduce available pore space. Therefore, another approach to modelling experiments was tested, where randomly distributed impermeable micro-barriers were introduced in the grid. The micro-barriers are based on a parameter called 'transmissibilty', which is a numerical simulation property that describes fluid flow between grid-blocks. It takes into account properties of the grid (permeability) and fluids (viscosity, density). Application of the transmissibility parameter in simulations determines flow across the contact surface of neighbouring grid-blocks. The parameter can be adjusted in order to control the flow from one grid-block to another without modifying properties of these grid-blocks. In this way, injected fluid can flow into any grid-block, and if it meets zero-transmissibility barrier on its way, it must pass it around in order to continue flowing. The modified grid had 2% of grid-blocks with randomly given zero-transmissibilitiy to each flow direction: from lower to upper grid-block, upper to lower, left to right and right to left. In total, approximately 8% of grid-block to grid-block transmissibilities were affected in the model (some of the grid-blocks could have transmissibility randomly modified in more than one direction). The simulation results show a plume development with irregular shape and noticeable branching, which was mostly inhibited at the later time. However, the overall shape, size, and time when plume reached the top of the model was satisfactory. Micro-barriers are only diverting the flow and do not slow it down like low permeable cells. Therefore this type of grid alteration was chosen to be used in all further simulations in high-IFT fluid system presented in this work.

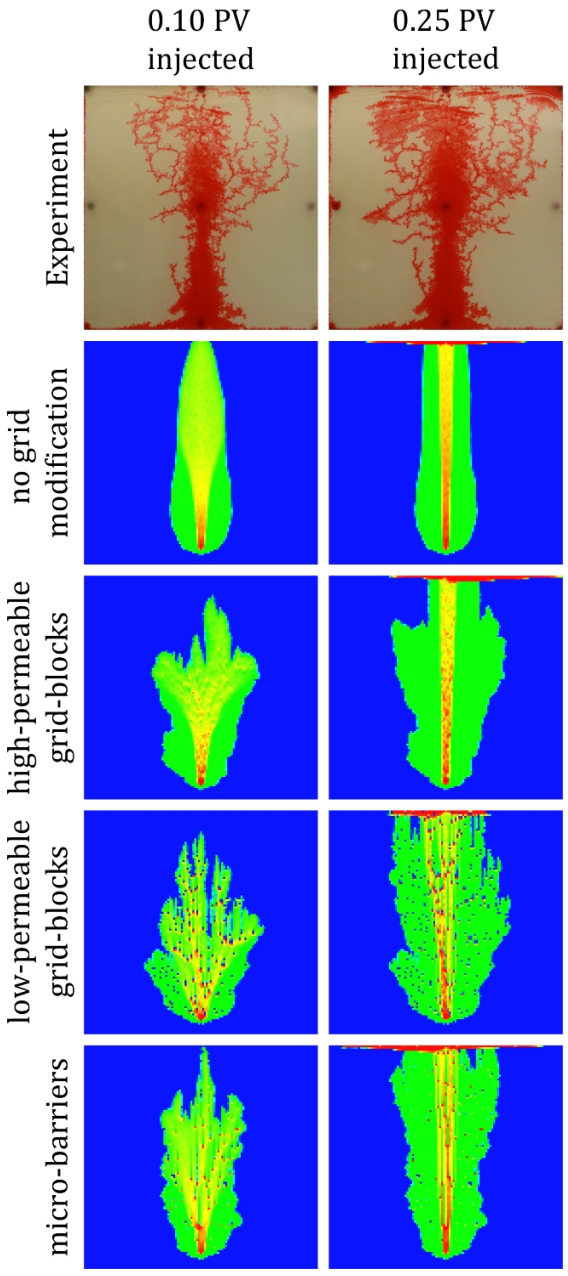

Figure 3.16 ***Results comparison of simulations in high-IFT system with different grid properties; case 1B (high-IFT, low-k, mid-q).***

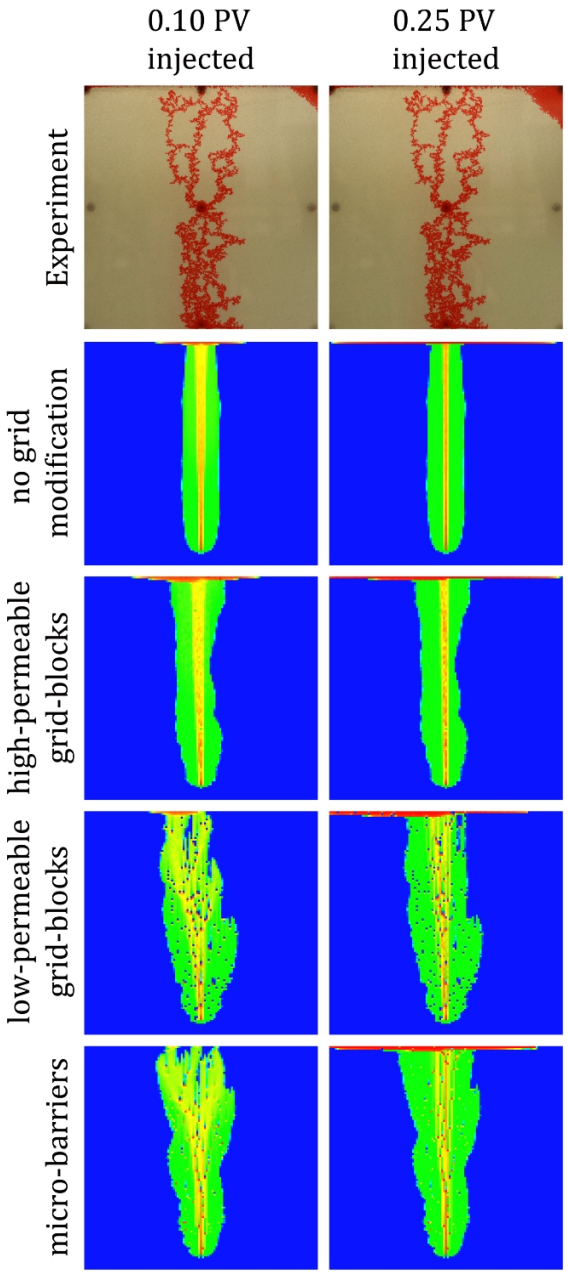

Figure 3.17 ***Results comparison of simulations in high-IFT system with different grid properties; case 2B (high-IFT, high-k, mid-q).***

3.6.2 Relative permeability curves

Detailed description of the relative permeability curves and discussion regarding parameters utilized in simulations is given in Paper IV. Here, plots with curves that were used are presented, as well as equations, applied in calculations.

Individual curves were used for matching production of the 'brine' in each experiment. A denser fluid was modelled as a water (wetting phase) and lighter as a gas (non-wetting phase). The relative permeability curves were calculated according to the Brooks and Corey's correlation (Brooks and Corey 1964; Corey 1954; Honarpour et al. 1994). Equations in following form were used in calculations:

$$k_{rw} = a(S_w^*)^b$$

Equation 3.7

$$k_{rnw} = c(1 - S_w^*)^d$$

Equation 3.8

$$S_w^* = \frac{S_w - S_{wi}}{1 - S_{wi} - S_{nwr}}$$

Equation 3.9

where: k_{rw} – wetting phase relative permeability; k_{rnw} – non-wetting phase relative permeability; a, b, c, d – empirical constants; S_w* – effective wetting phase saturation; S_w – wetting phase saturation; S_{wi} – wetting phase irreducible saturation; S_{nwr} – non-wetting phase residual saturation (minimal non-wetting phase saturation after wetting phase flooding).

Parameters applied in calculation of relative permeability curves are listed in Table 3.10. All curves used in simulations are presented in Figure 3.18.

Table 3.10 ***Parameters used in calculations of the relative permeability curves used in simulations (table from Paper IV).***

Parameter	Case					
	1A	1B	1C	2A	2B	2C
S_{wi}	0.20					
S_{nwr}	0.40					
a	1.00					
c	0.80					
b	2.50	1.50	1.00	4.50	3.15	2.50
d						

Parameter	Case					
	3A	3B	3C	4A	4B	4C
S_{wi}	0.10					
S_{nwr}	0.20					
a	1.00					
c	0.90					
b	3.90	3.25	2.65	4.75	3.40	2.50
d						

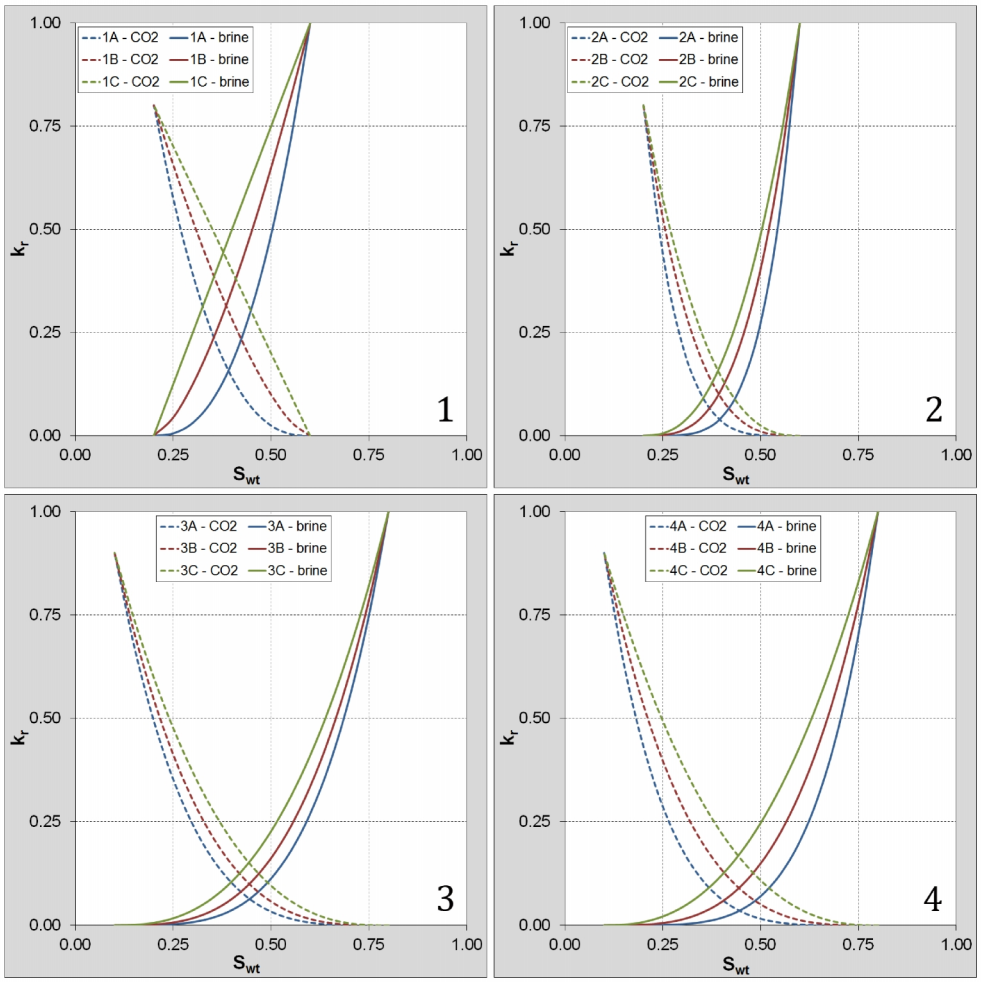

Figure 3.18. Relative permeability curves used in simulations for matching brine production from experiments.

3.6.3 Use of capillary pressure curve in simulation of experiments

In simulations of laboratory experiments, capillary pressure, P_c, was assumed to be zero. This assumption was made based on the test simulations, which shown that when P_c is used, the displacement front of the injection plume becomes very smooth. This was not in agreement with observations from experiments, and therefore, P_c curve in simulations was not applied. Results of simulations without P_c are described in details in Paper IV. Here, a comparison of simulation results with and without P_c for the high-IFT and low-IFT case is demonstrated.

The relative permeability curve used in simulations is of Brooks and Corey type (Brooks and Corey 1964). The following formula was utilized in calculations:

$$P_c = P_{ce} \cdot (S_w^*)^{-n}$$

Equation 3.10

where: P_{ce} – entry capillary pressure, bar; S_w^* – normalized water saturation (the same as in relative permeability calculations (see chapter 3.6.2, Equation 3.9); n – parameter related to pore-size distribution index.

The entry capillary pressure, P_{ce}, was calculated according to following equation:

$$P_{ce} = (\rho_w - \rho_{nw}) \cdot g \cdot h$$

Equation 3.11

where: ρ_w – density of wetting phase, kg/m^3; ρ_{nw} – density of non-wetting phase, kg/m^3; g – acceleration of gravity, m/s^2; h – distance between model's inlet and top outlet, m. The result of the Equation 3.11 will be given in Pa. The P_{ce} corresponds to a P_c at the wetting phase saturation of 1-S_{nwr}, which is the wetting phase saturation at residual saturation of the non-wetting phase.

Two capillary pressure curves were produced for each fluid system, and additionally, a constant P_c has been tested. The wetting phase irreducible saturation, S_{wi}, and non-wetting phase residual saturation S_{nwr} used for calculating normalized water saturation S_w^* were the same as in relative permeability calculations for respective fluid systems (chapter 3.6.2). P_{ce} was unique for each fluid system as densities of fluids were different in each of them. List of parameters used in calculations of the capillary pressure curves is presented in Table 3.11 and capillary pressure curves applied in simulations are shown in Figure 3.19.

Figure 3.19 shows comparison of simulation results with different capillary pressure curves. Although results presented here are only for cases with a mid-q injection rate (0.25 cm^3/min) and at the 0.10 PV injected, they are representative for all cases. Simulations with constant P_c (n=0, thus P_c=P_{ce}) were practically identical to those with P_c equal zero, e.g. total volume of displaced 'brine' was approx. $2 \cdot 10^{-4}$ lower). For that reason simulations with P_c=0 are not presented in figures.

As can be seen in Figure 3.20 the shape of the injection plume becomes more oval as the 'n' parameter increases. Also the contour of the plume, or the displacement front, changes shape and becomes less bifurcated in cases 1B and 2B (at n=0.01) and even smooth and rounded in all other cases. This is caused by the increasing P_c at lower water saturations as shown in Figure 3.19, especially at higher 'n' value.

Example of simulation with constant P_c=P_{ce}, where results are almost identical to simulation with P_c=0, may indicate that, the P_c in experiments indeed was very low and it could be neglected in simulations. For that reason all simulations presented in this work and in Paper IV have P_c=0.

In Paper III (Appendix C) (Bergmo et al. 2013) influence of changing capillary pressure curves on results in reservoir simulations of CO_2 storage is described and discussed.

Table 3.11 Parameters used in calculations of the capillary pressure curves.

Parameter	Fluid system		Units
	high-IFT	low-IFT	
ρ_w	1160.4	903.1	kg/m^3
ρ_{nw}	684.5	697.5	kg/m^3
g	9.81	9.81	m/s^2
h	0.28	0.28	m
P_{ce}	1307.20	564.74	Pa
	0.013072	0.005647	bar
S_{wi}	0.20	0.10	-
S_{nwr}	0.40	0.20	-
n	0, 0.1, 0.01	0, 0.1, 0.01	-

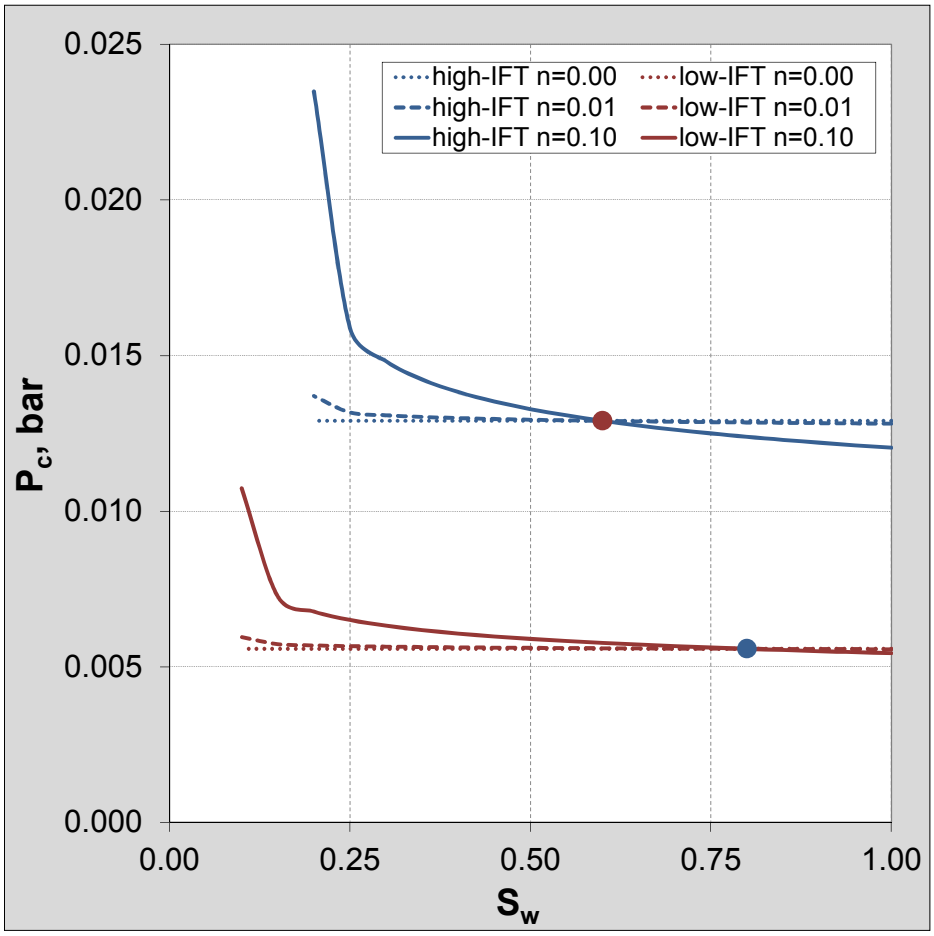

Figure 3.19 Capillary pressure curves used in simulations calculated with different 'n' parameter; marker indicates calculated P_{ce} at the $S_w=1-S_{nwr}$.

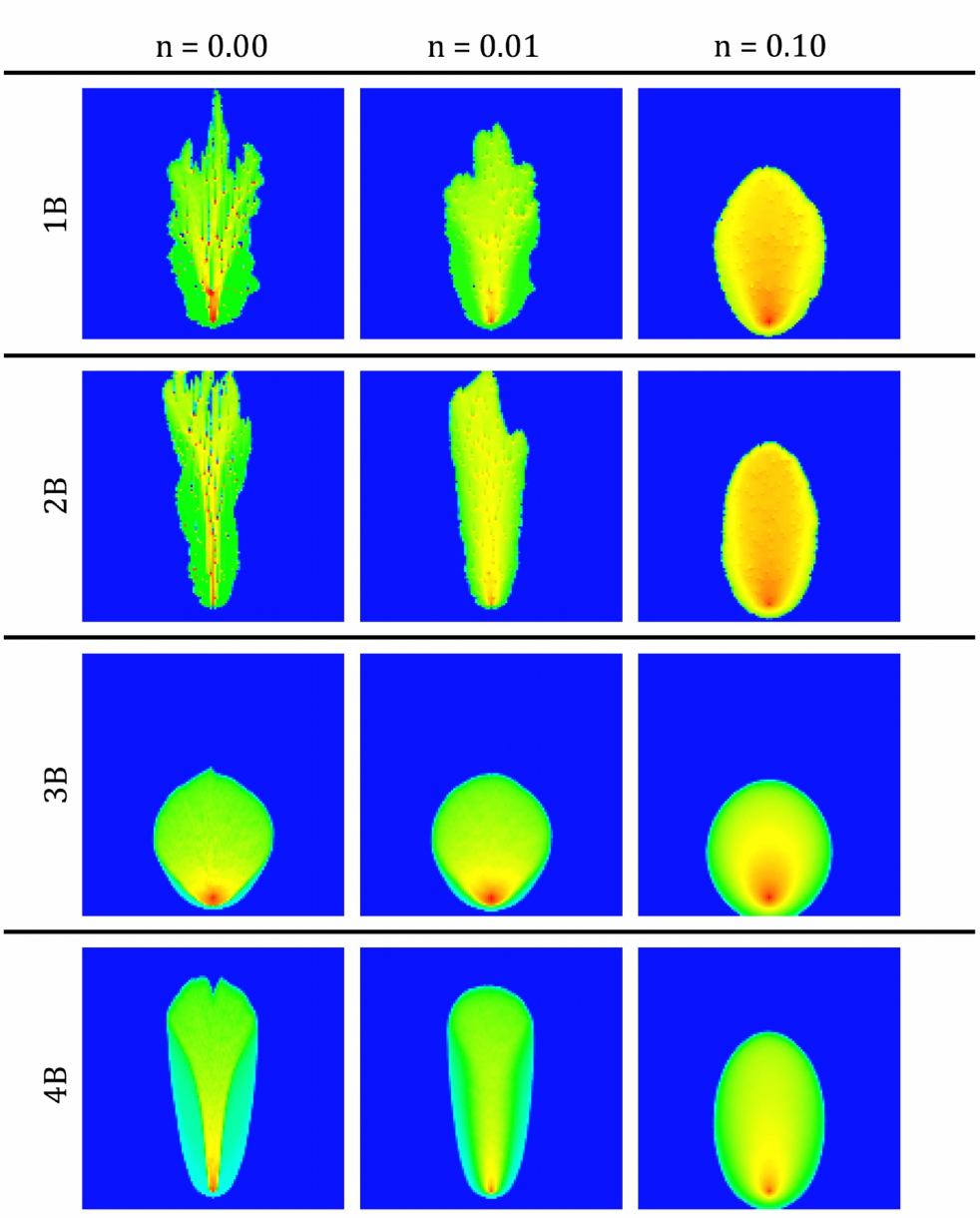

Figure 3.20 ***Results comparison of simulations with different capillary pressure curves (Figure 3.19); comparison made only for cases with a mid-q (0.25 cm^3/min) injection rate and at the 0.10 PV injected; curve at n=0.00 corresponded to constant value of capillary pressure equal to P_{ce}; results of simulations with curve at n=0.00 are practically identical to those with no capillary pressure.***

4 Summary of results

This chapter includes the summary of work performed during this PhD project. Papers are not presented in the chronological order but in a logical order, i.e. firstly are summarised findings that are related to the laboratory experiments and results of the simulations (Paper II and Paper IV) with supplementary results, which were not published. The next paper (Paper III) concerns numerical simulation study of CO_2 injection performed on a generic model and also on a model of possible storage site. The last paper (Paper I) concerns reservoir simulations of CO_2 storage in a possible storage site. This paper focuses on different type of geological setting than in Paper III and discusses the risks related to leakage through abandoned wells.

4.1 Paper II, Paper IV, and supplementary results

4.1.1 Paper II – An experimental investigation of the balance between capillary, viscous, and gravitational forces during CO_2 injection into saline aquifers

Paper II presents experimental investigation of the scaling laws describing CO_2 injection into geological formations. Quasi two-dimensional experiments were performed in glass-bead packs initially saturated with 'model-brine'. They demonstrate the influence of gravitational, viscous and capillary effects on the vertical flow of the injected 'model-CO_2'. The experiments were performed in the ambient conditions and the properties of fluids used in the experiments were analogous to the properties of CO_2 and brine at possible reservoir conditions. This means that fluid system with high interfacial tension (IFT) was used. Experiments were performed for a range of dimensionless capillary (N_C) and capillary-to-gravity (R_{CG}) numbers, which may describe conditions at existing storage sites. The use of dimensionless numbers links the laboratory experiments with the field scale observations, and hence these numbers can be applied for the screening of potential storage sites.

The experiments were characterised by gravity and viscous unstable floods. The effects of gravity forces were more pronounced in cases with a low injection rate and high permeability. In these cases fluid flow occurred more in the vertical direction causing that the plume of the injected fluid was the narrowest. As a result, less volume of the in-situ fluid was displaced compared to other cases.

At higher injection rates, the impact of viscous forces increased. This resulted in a larger injection plume and thus increase in 'brine' recovery. Higher injection rates caused also more fingering. Also when permeability of a porous medium was lower higher sweep efficiency in the displaced area was achieved.

Investigation of relationship between the PV of 'brine' displaced and the $R_{CG} \cdot N_C$ number, defined as ratio of viscous to gravity forces – R_{VG}, indicates that the volume of 'brine' displaced decreases due to increased gravity control in the displacement. This was due to the fact that the gravity instability creates smaller injection plumes with shorter flow paths compared to those more dominated by the viscous instability.

R_{CG} and R_{VG} numbers were also calculated for the field cases and compared to those from experiments. Calculations were made for the same range of the flow rates as those used in the experiments. Although at laboratory conditions properties of the used fluids correspond to properties of CO_2 and brine at possible reservoir conditions, the range of the existing storage sites was not reached in the scaling calculations. One of the field examples, the Sleipner case, scaled particularly far from experiments, showing strong influence of gravity forces. This was due to reservoir's high permeability and thickness. The laboratory experiments, however, are dominated by viscous and especially capillary forces, mainly due to the high IFT of the fluid system. The experiments that scaled close to some of the sedimentary basins were at the high permeability and low injection rate. By altering parameters of the experimental system, such as IFT of the fluids, injection rate, and permeability, it could be possible to scale the experiments to the conditions occurring in real storage sites.

4.1.2 Paper IV – Use of Low- and High-IFT Fluid Systems in Experimental and Numerical Modelling of CO_2 Storage in Deep Saline Formations

Results presented in Paper IV constitute continuation of the research work described in Paper II. In addition to high-IFT fluid system, the low-IFT system has been used and results from both systems were compared. Additionally, the laboratory experiments were modelled in the numerical simulator. The forces acting on the fluid flow were analysed and assessed by use of scaling parameters.

A vertical, 2D model filled with glass-beads was saturated with model 'brine' fluid. The model 'CO_2' was injected from the bottom of the experimental model, the produced effluent was collected and displaced volumes were measured. In total 11 cases with different combinations of parameters were investigated. The varied parameters were: IFT of the fluids, permeability of the model, and injection rate. Scaling parameters were used in order to assess forces acting on the flow of fluids in the experiments. These were capillary number (N_C) and capillary-to-gravity-ratio (R_{CG}).

The numerical simulations in high-IFT system were challenging, as simulator was unable to reproduce channelling observed in the high-IFT experiments. This was, however, to some degree, solved by modifications of the grid properties by introducing randomly distributed transmissibility micro-barriers. Such modifications were not necessary in case of low-IFT system, as simulator reproduced results of experiments accurately. In order to match 'brine' production in simulations, each case had its own set of relative permeability curves adjusted.

Based on the results of the experiments, it is possible to conclude that a low-IFT fluid system is more suitable for laboratory scale experiments than a high-IFT fluid system, because simulations reproduce more accurately experimental observations made at low-IFT. Also, experiments with a low-IFT fluid system are expected to better resemble field scale flow behaviour and distribution of fluids. Although the high-IFT fluid system had an IFT close to the value for a CO_2-brine system at possible reservoir conditions, the capillary forces dominated the flow in the laboratory model, what is less likely to be observe at the field scale.

The effects of gravity forces were stronger in cases with low injection rates and high permeability. Where gravity effects were dominating, less volume of the in-situ fluid was displaced. The flow occurred more in vertical direction, and thus, large part of 'brine' was bypassed. In the real-life applications this effect is not desired as it is preferred that the injected CO_2 displaces as much brine as possible. It also implies that formations with lower influence of gravity forces are more suitable for CO_2 storage. The increase in the injection rate causes that gravity forces are becoming weaker and viscous forces are stronger. In such conditions a higher total displacement of brine was obtained. Therefore, reservoirs where permeability is low and high injection rates are possible, could be the most suitable for storage of CO_2. At such conditions, however, the pressure increase due to injection can lead to damaging the geological formation by fracturing. This is undesired effect, which can cause early breakthrough of CO_2 to the pressure-releasing brine production wells, if such were used. Fracturing can also damage the sealing of the storage formation, which would compromise the safety of the storage site.

4.1.3 Supplementary results

Laboratory work

Dimensionless numbers used for scaling of the results link the laboratory experiments with the field-scale observations. Experiments were described by dimensionless capillary (N_C) and viscous-to-gravity-ratio (R_{VG}) numbers which incorporate fluid and porous media (rock) properties. Experimental dimensionless parameters for high-IFT system agree reasonably well with calculations for some generic sedimentary basins but they are relatively far from the existing storage sites. Calculations for the low-IFT fluid system scale even further away from the field cases. One of the parameters that strongly influences these results is flow velocity. The same flow velocity range was assumed in both experiments and field cases. As these velocities are relatively low, they are expected to occur in the reservoir far from the injection point, where gravity forces are dominating. If flow velocity used in calculations for field cases was higher (i.e. closer to injection point), the calculated scaling parameters would shift field cases closer to the experiments. In theory, it is possible to design conditions in which experiments would scale close to the field cases, but it is not achievable in current laboratory setting.

Simulations

The numerical modelling of high-IFT experiments was challenging, and it was necessary to alter grid parameters in order to obtain results resembling flow channels observed in experiments. A number of simulations was performed where various approaches to modelling of the flow channels were tested. Based on analysis of results it was decided that the most appropriate way of modelling high-IFT cases would be introduction of randomly distributed micro-barriers. These barriers did not modify properties of the grid-block but were diverting the flow and creating channel-like structures. Although this approach gave satisfactory results, the need for improving modelling of high-IFT system remained.

There were made sensitivities on use of the capillary pressure curves in simulations. Results showed that capillary pressure curve will negatively affect outcome of the simulations compared to laboratory experiments. When capillary pressure was used, the front of injection plume was becoming smoother which was the opposite of the observations in experiments. Also, the flow of the injected fluid was increasing horizontally and the plume was becoming significantly wider than in experiments. When capillary pressure was set to a constant value of the calculated capillary entry pressure the results were identical to those where capillary pressure was set to zero.

4.2 Paper III – Evaluation of CO_2 Storage Potential in Skagerrak

In Paper III results of the reservoir simulation study of possible CO_2 storage site within Skagerrak-Kattegat area between Denmark, Sweden and Norway are presented. Additionally, identification and analysis of parameters important for the migration speed and the dissolution rate of CO_2 in open dipping aquifers were investigated by a series of simulations on generic tilted reservoir models. The critical factors for safe storage are the fracturation pressure of the sealing cap rock and the parameters controlling lateral migration of the injected CO_2.

Three models were developed for three different storage sites in the saline aquifers and in each of them three horizontal injection wells were used for injecting 250 Mtonnes of CO_2 over the period of 25 years. One of the models is for the Hanstholm structure, which is a domal closure and has enough capacity to store all injected CO_2. However, due to injectivity problems, the pressure increase may rise above the fracturation pressure. This could be amended by introducing more injection wells or brine producing wells that would release the pressure.

The two remaining models were for the Gassum Formation. These were open dipping traps where the lateral migration speed of CO_2 was important for estimating capacity and safety of the storage. Therefore, a series of additional simulations on a synthetic tilted model were performed. They were investigating migration speed and dissolution rate as function of grid block resolution and capillary pressure.

Capillary pressure affects the migration speed and thickness of the CO_2 front. As there was no capillary pressure measurements available for the Gassum Formation, capillary pressure measured on Utsira sand was used as basis for sensitivity simulations. Simulations were performed with varying capillary pressure by multiplying the measured capillary pressure curve by factors 2, 4, 8, 16, and 32. Increase in the capillary entry pressure reduces distance of CO_2 migration because CO_2 has to overcome the capillary entry pressure before it can flow into a neighbouring grid-block. Therefore, if the grid layering is fine enough, the thickness of the migrating CO_2 front is larger.

The thickness of the migrating front in the simulations depends also on grid layer thickness and critical gas saturation (lowest gas saturation before it starts to flow) and they should be balanced to represent the effect of capillary pressure. By increasing the layer thickness the injection plume length will be reduced. This is due to increased thickness of the front and because the increased size of the grid-blocks will require a larger volume of CO_2 in each grid-block to overcome the critical gas saturation. This also slows down the speed of the migrating front. Smaller grid blocks reduce the gas

volume required to overcome the critical gas saturation, but this effect will be minor if the coarser grid resolution is sufficient to resolve the shape of the migrating CO_2.

In case of CO_2 dissolution into the formation water, it is dependent on the contact area between the CO_2 and formation water. This means that increased migration distance will result in an increase in CO_2 dissolution.

When finer grid-blocks are used in two of the presented storage models, the migration distance is increased and the injected CO_2 migrates out of the boundaries of the one of the models. Although the outcome of the reservoir simulations is influenced by uncertainty due to insufficient data, the performed analysis of parameters influencing simulation results gives additional insights on how results are sensitive to various parameters. This emphasises even more the need for thorough and comprehensive collection and preparation of data needed for CO_2 storage site characterisation.

4.3 Paper I – Reservoir simulation study of CO_2 storage and CO_2-EGR in the Atzbach-Schwanenstadt gas field in Austria

Paper I presents results of the reservoir simulations of short and long term CO_2 storage in the Atzbach-Schwanenstadt mature gas field in Austria. The work focuses on CO_2 distribution within reservoir during and after injection as well as on a storage safety. Potential for enhanced gas recovery (EGR) was also evaluated.

Simulations were performed in the compositional numerical simulator Eclipse 300 with an eight-component description used for the reservoir gas. As the field was producing gas for many years it was necessary to establish current state by matching history observation. The model was used then for predictions of CO_2 storage.

The total storage capacity of the field was estimated to be 14.5 million tonnes of CO_2 and was constrained by the volume of gas produced and the initial reservoir pressure. This was, however, only theoretical capacity as the actual capacity would be lower. The limiting factor was mainly low permeability which would restrict the distribution of CO_2 in the reservoir, and therefore not all available pore space could be reached by injected CO_2. The target injection rate was 300 000 tonnes of CO_2 per year. Normally this volume could be easily injected using only one well, but due to low permeability of the reservoir at least three injection wells were needed. If only one well was used, the CO_2 injection would dangerously increase pressure near the well, what could damage the reservoir and possibly a seal by fracturing.

Results of simulations show that 8.2 million tonnes of CO_2 could be stored over a period of 30 years. However, injection rates had to be reduced towards the end of that

period in order to keep pressure near the well bottom below the initial reservoir pressure. An attempt to produce natural gas from the reservoir during CO_2 injection did not give good results as produced gas was highly contaminated by the CO_2 soon after production started.

In order to investigate fate of the CO_2 in the reservoir after the storage process was finished the long-term reservoir simulations were made. The study focused on pressure changes and CO_2 concentration distribution in the reservoir, and additionally a case of hypothetical leakage through abandoned wells was considered. Results show that after injection stopped the movement of gas in the reservoir evens out the pressure, which was highest around injection wells. Also 10% of the CO_2 was dissolved in the immobile reservoir water.

As the CO_2 was continuing to flow in the reservoir after stop of injection, it could come in contact with some of the abandoned wells. Since these wells were abandoned according to regulations that do not consider exposure to CO_2 they may pose a risk of leakage. The investigated leakage cases showed that 5.6% of the injected CO_2 may leak over a period of 1500 years, which may be considered as a hazard in urban areas.

5 Discussion, conclusions, and recommendations for further work

Discussion and conclusions

This thesis focuses on experimental and numerical modelling of CO_2 storage in geological formations. Two main areas of the performed research can be distinguished here:

1) Laboratory flow experiments performed on 2D model, and numerical modelling of these experiments.
2) Full-field reservoir modelling on both generic models and real reservoirs.

The flow experiments performed in a 2D glass-bead-filled model showed the plume development and the flow patterns of the injected fluid ('CO_2') from the start of injection until it reached the top of the model reservoir. The experiments were described by a range of dimensionless numbers N_C and R_{CG}. The use of dimensionless numbers links the laboratory experiments with the field scale observations and hence these numbers can be applied for the screening of potential storage sites. Analysis and comparison of the scaling made for storage sites and laboratory experiments showed that they scale distantly from each other, however, some of the generic sedimentary basins did scale close to high-IFT experiments. In order to achieve scaling of the experiments closer to the existing or possible storage sites, the experimental system has to be optimized. The difficulty lies in finding a suitable pair of immiscible fluids with desired properties. Parameters that must be taken into account are IFT, viscosity (especially that of the lighter fluid), and density difference. Parameters that are fluid independent, i.e. permeability and flow velocity, are easier to control with glass-bead size and injection rate, respectively. Porosity in the value range that was measured in the experiments do not have much influence on the results of calculations. Also model's geometry is rather fixed.

The numerical simulations of the laboratory experiments were challenging in case of high-IFT system. Difficulty lies in mimicking the channels that are created by injected fluid. The high IFT is responsible for stronger influence of the capillary forces and hence creation of these flow channels. Various approaches were tested in modelling of the high-IFT system, with relatively good results obtained by introduction of randomly distributed micro-barriers. In case of modelling flow in low-IFT system, the numerical simulator reproduced well experimental observations.

The full-field reservoir simulations concerned possible storage in deep saline aquifers and mature gas field. Although these are two very different geological settings the common focus was on parameters that influence storage capacity and migration of the injected CO_2 in the reservoir, i.e. capillary pressure and permeability. Results of simulations made on generic models showed that one has to be very careful in hastily drawing conclusions from modelling. Great care must be taken when capillary pressure curves are used because results of simulations are very sensitive to this parameter. Also grid resolution is an important factor, that if not used correctly, it might give false results.

The permeability of the reservoir is one of the parameters that influence the distribution of the forces acting on the fluid flow. It is desired that system is dominated by viscous forces and this corresponds to low permeability. This causes that injected CO_2 contacts more reservoir water, which in turn, enhances dissolution. However, when permeability field of the reservoir is highly heterogeneous, CO_2 will flow in channels with higher permeability, thus large part of the reservoir will be omitted by CO_2 and not all available storage capacity will be utilized. Additionally, low permeability might cause increase of pressure in the near-well zone, what can have negative influence on the performance of the storage site.

To summarise the work presented in this thesis, the following conclusions can be drawn:

1) The laboratory experiments using a low-IFT fluid system are expected to better resemble field scale behaviour in terms of the flow and distribution of fluids.
2) A high-IFT fluid system is less suitable for laboratory scale experiments compared to a low-IFT fluid system, as it is difficult to accurately reproduce experimental observations in numerical simulations. Series of simulation sensitivities concluded that the best way of representing high-IFT fluid system in simulations is by introducing in the grid randomly distributed micro-barriers.
3) Although the high-IFT fluid system used in experiment had an IFT close to the value for a CO_2-brine system at possible reservoir conditions, the capillary

forces have dominated the flow in the laboratory model. It is less likely to observe this kind of behaviour at a field scale.

4) Experiments confirmed that effects of gravity are stronger when injection rates are low and permeability is high. When gravity effects dominate the flow, less volume of the in-situ fluid is displaced. The flow occurs more in vertical direction, and thus, large part of brine is bypassed. During injection of CO_2 into geological formations it is preferred that CO_2 displaces as much brine as possible since it enhances CO_2 dissolution in brine. Therefore reservoirs characterised by low influence of gravity forces are more suitable for CO_2 storage. This will normally relate to low permeability and high injection rates.
5) The viscous forces are stronger when the injection rate increases. At such conditions the displacement of brine in the laboratory experiments increased and this effect was emphasised by lower permeability. Therefore reservoirs with low permeability and high injection rates are expected to be the most suitable for storage of CO_2. However, such conditions can lead to pressure increase due to injection and this can possibly damage the geological formation by fracturing. This could cause breakthrough of CO_2 to the brine producing wells, if such are used, or even damage the sealing of the reservoir formation, which could compromise safety of the storage site.
6) Dimensionless analysis of the experiments and reservoir cases showed that the experimental capillary number and viscous-to-gravity ratio at high-IFT and low injection rate agree reasonably well with calculations for some of the sedimentary basins and storage sites. However, low-IFT experiments scale far from the field cases. It should be noted, that this is a case when the range of flow velocities is assumed to be the same in field cases and in experiments. Velocities used in experiments are normally expected to occur in the reservoir far from the injection point where the gravity forces dominate.
7) The scaling analysis shows importance of various parameters in the process of site characterisation for CO_2 storage. Representation of the reservoir conditions by means of the dimensionless analysis provides possibility of comparing various storage sites and predicting the flow regimes that may occur when CO_2 is injected.
8) Capillary pressure in the laboratory experiments was negligibly small and was not used in the numerical modelling. However, in the field application capillary pressure is an important parameter that controls migration speed and thickness of the CO_2 front. Results of the reservoir simulations proved to be very sensitive to this parameter.

9) Low permeability of the storage site will have negative impact on the storage capacity and well injectivity. Due to low permeability injected CO_2 will not be able to reach all parts of the reservoir, hence not all available pore space will be available for CO_2. Limited injectivity due to low permeability will have to be amended by lowering injection rate in order to avoid increase of pressure in the near-well zone, or introduction of additional injection wells.

Recommendations for further work

Further work should encompass optimization of the experimental setup, including both porous medium and sets of fluids. 2D model construction can be adjusted in order to make it easier to operate. Especially process of removing and re-filling glass-beads was complicated.

To obtain wider range of experimental results, new sets of fluids should be tested. Particularly interesting would be set of fluids with intermediate IFT compared to those presented in this thesis. Another possibility would be a test with injection of fluids at very low or nearly-zero-IFT (<1 mN/m). In such case only viscosity and density of the fluids would differentiate fluids from each other. These conditions would limit influence of the capillary forces as they are related to the IFT. While working with such fluids, distinguishing them in the model after injection would be most likely challenging. At the very low IFT, the fluids would most likely begin to dilute each other, as these are near miscible conditions, and distinguishing displacement front in the model could be difficult. In such case image analysis might be helpful. Computer software/scripts could be used for analysing colour intensity of the dyed injected fluid and give information on its concentration.

Another experiment worth to perform could be based on fluid system with viscosity ratio equal or close to one. This would limit the influence of the viscous forces on the results of experiments.

Additionally, investigation on a set of fluids with properties that would scale the experiments close to real reservoirs presented in Figure 3.15 in chapter 3.5.2 should be undertaken. Currently such set of fluids has not been found, although attempts were made in this project. Ether was used as an injected fluid and water as a displaced fluid, but due to volatility of ether the experiments were not successful.

Altering the experimental setup, at least in theory, could possibly give combination of parameters that would scale experiments close to real storage sites. However, in practice it is difficult to materialize such system in ambient conditions. From a theoretical analysis the following combination of parameters would meet requirements for such a system: very low injection rate (< 0.10 cm^3/min), high permeability (100 D

and more), low viscosity of the injected fluid (approx. 0.2 mPa·s or less), high density difference between injected and displaced fluid (500 kg/m^3 or more), and longer distance from inlet to top of the model reservoir (50 cm or more). Such experiments were not possible with the current model, partly due to fixed size of the model and partly due to not sufficient accuracy of the instruments (pumps, balances, and pressure gauge) for such measurements. Additionally, injection with such a low rate would be very time consuming. However, the outcome of the experiment at such conditions is predictable. It would result in very thin channel/finger slowly rising up in the model, as the gravity forces would strongly dominate the flow. This would allow scaling of the experiment close to, or even on par with, the existing storage sites in which the flow is mainly dominated by gravity forces.

If experiments were performed in horizontally placed model it would eliminate the influence of gravity forces from the experiments. Then, by increasing the tilt angle, the effect of increasing gravity forces on the system could be evaluated.

The numerical simulations study of laboratory experiments revealed that Eclipse 100 struggles with representation of some of the experiments. It could therefore be beneficial to investigate other available software or develop new tools, more suitable for modelling of such processes.

These are only some of the possible directions of continuing and extending the research started in this project. The results of this work are encouraging as they are contributing to the better understanding of the flow processes that may occur during CO_2 injection into a geological formation. Additionally, presented methodology is applicable in the site characterization process. Improvements in measurements and modelling of the flow parameters in the CO_2-water systems will increase confidence in assessment of the capacity and safety of the storage site.

List of symbols and abbreviations

A – cross-section surface area, m^2
a, b, c, d – empirical constants in relative permeability calculations
d_b – glass-bead diameter, m
ECBM – enhanced coal bed methane
EOS – equation of state
GHG – greenhouse gases
g – acceleration of gravity, m/s^2
Gt – gigatonnes, 10^9 tonnes
γ – interfacial tension, IFT, mN/m
h – distance between model's inlet and top outlet, m
H – a solid, non-stoichiometric CO_2-clathrate-hydrate ($CO_2 \cdot 7.5\ H_2O$)
IFT – interfacial tension, mN/m
IPCC – The Intergovernmental Panel on Climate Change
k – permeability, m^2 or mD or D
k_h – horizontal permeability, m^2 or mD or D
k_{rnw} – non-wetting phase relative permeability
k_{rw} – wetting phase relative permeability
k_v – vertical permeability, m^2 or mD or D
L – glass bead pack length, m
L_{aq} – a CO_2 bearing water-rich liquid (aqueous phase)
L_{CO2} – a CO_2-rich liquid phase
μ – fluid viscosity, Pa·s or mPa·s
n – amount of substance of gas, moles
N_C – capillary number
P – pressure, bar
P_c – capillary pressure, bar
P_{ce} – entry capillary pressure, bar
Δp – pressure drop, Pa
ϕ – porosity
Ø – diameter of assembly screws, mm
q – flow rate, m^3/s
Q_1, Q_2 – the first and the second quadrupole point
R – gas constant, 8.3144621(75) J/mol·K
R_{CG} – ratio of capillary to gravity forces
R_{VG} – ratio of viscous to gravity forces
ρ_{nw} – density of non-wetting phase, kg/m^3
ρ_w – density of wetting phase, kg/m^3
Δρ – density difference of the fluids, kg/m^3
S_{nwr} – non-wetting phase residual saturation
S_w – wetting phase saturation
S_w* – effective wetting phase saturation
S_{wi} – wetting phase irreducible saturation
T – Temperature, °C or K
u – Darcy's flow velocity, m/s
V – volume, m^3
V – a CO_2-rich vapour phase

References

Akervoll, I., Lindeberg, E., Lackner, A.: Feasibility of Reproduction of Stored CO_2 from the Utsira Formation at the Sleipner Gas Field. Energy Procedia **1**(1), 2557-2564 (2009). doi:http://dx.doi.org/10.1016/j.egypro.2009.02.020

Angus, S., Armstrong, B., De Reuck, K.: Carbon dioxide. International Thermodynamic Tables of the Fluid State–3, IUPAC. In. Pergamon Press: Oxford, (1976)

Arts, R., Eiken, O., Chadwick, A., Zweigel, P., van der Meer, L., Zinszner, B.: Monitoring of CO_2 injected at Sleipner using time-lapse seismic data. Energy **29**(9–10), 1383-1392 (2004). doi:http://dx.doi.org/10.1016/j.energy.2004.03.072

Baines, S.J., Worden, R.H.: The long-term fate of CO_2 in the subsurface: natural analogues for CO_2 storage. In: Baines, S.J., Worden, R.H. (eds.) Geological Storage of Carbon Dioxide, vol. Special Publications. pp. 59-85. Geological Society, London (2004)

Bakk, A., Girard, J.-F., Lindeberg, E., Aker, E., Wertz, F., Buddensiek, M., Barrio, M., Jones, D.: CO_2 Field Lab at Svelvik Ridge: Site Suitability. Energy Procedia **23**(0), 306-312 (2012). doi:http://dx.doi.org/10.1016/j.egypro.2012.06.055

Baklid, A., Korbøl, R., Owren, G.: Sleipner Vest CO_2 disposal, CO_2 injection into a shallow underground aquifer. Paper presented at the SPE Annual Technical Conference and Exhibition, 6-9 October 1996, Denver, Colorado, USA,

Beaubien, S.E., Lombardi, S., Ciotoli, G., Annuziatellis, A., Hatziyannis, G., Metaxas, A., Pearce, J.M.: Potential hazards of CO_2 leakage in storage systems—Learning from natural systems. In: Rubin, E.S., Keith, D.W., Gilboy, C.F., Wilson, M., Morris, T., Gale, J., Thambimuthu, K. (eds.) Greenhouse Gas Control Technologies 7. pp. 551-560. Elsevier Science Ltd, Oxford (2005)

Bennion, D.B., Bachu, S.: Dependence on Temperature, Pressure, and Salinity of the IFT and Relative Permeability Displacement Characteristics of CO_2 Injected in Deep Saline Aquifers. Paper presented at the SPE Annual Technical Conference and Exhibition, San Antonio, Texas, USA,

Bennion, D.B., Bachu, S.: The Impact of Interfacial Tension and Pore Size Distribution/Capillary Pressure Character on CO_2 Relative Permeability at Reservoir Conditions in CO_2-Brine Systems. Paper presented at the SPE/DOE Symposium on Improved Oil Recovery, Tulsa, Oklahoma, USA, 04/22/2006

Berg, S., Ott, H.: Stability of CO_2–brine immiscible displacement. International Journal of Greenhouse Gas Control **11**(0), 188-203 (2012). doi:http://dx.doi.org/10.1016/j.ijggc.2012.07.001

Bergmo, P.E.S., Polak, S., Aagaard, P., Frykman, P., Haugen, H.A., Bjørnsen, D.: Evaluation of CO_2 Storage Potential in Skagerrak. Energy Procedia **37**(0), 4863-4871 (2013). doi:http://dx.doi.org/10.1016/j.egypro.2013.06.396

Braathen, A., Baelum, K., Christiansen, H., Dahl, T., Eiken, O., Elvebakk, H., Hansen, F., Hanssen, T., Hochmann, M., Johansen, T.: The Longyearbyen CO_2 Lab of Svalbard, Norway–initial assessment of the geological conditions for CO_2 sequestration. Norwegian Journal of Geology **92**, 353-376 (2012)

Brooks, R., Corey, A.: Hydraulic properties of porous media, Hydrology Papers, No. 3, Colorado State University, Ft. Collins, Colo (1964)

Chadwick, R.A., Arts, R., Bernstone, C., May, F., Thibeau, S., Zweigel, P. (eds.): Best practice for the storage of CO_2 in saline aquifers. British Geological Survey Occasional Publication No. 14, Keyworth, Nottingham (2008)
Cinar, Y., Riaz, A., Tchelepi, H.A.: Experimental Study of CO_2 Injection Into Saline Formations. SPE Journal **14**(4), 588-594 (2009). doi:10.2118/110628-pa
CO2CRC: Storage Capacity Estimation, Site Selection and Characterisation for CO_2 Storage Projects. In., vol. CO2CRC Report No. RPT08-1001. Cooperative Research Centre for Greenhouse Gas Technologies, Canberra, (2008)
Corey, A.T.: The interrelation between gas and oil relative permeabilities. Producers monthly **19**(1), 38-41 (1954)
European Commission: CO_2 Capture and Storage Projects. In. Directorate-General for Research; Sustainable Energy Systems, Luxembourg: Office for Official Publications of the European Communities, (2007)
Fenghour, A., Wakeham, W.A., Vesovic, V.: The viscosity of carbon dioxide. Journal of Physical and Chemical Reference Data **27**(1), 31-44 (1998)
Gor, G.Y., Prévost, J.H.: Effect of CO2 Injection Temperature on Caprock Stability. Energy Procedia **37**(0), 3727-3732 (2013). doi:http://dx.doi.org/10.1016/j.egypro.2013.06.267
Gunter, W.D., Bachu, S., Benson, S.: The role of hydrogeological and geochemical trapping in sedimentary basins for secure geological storage of carbon dioxide. In: Baines, S.J., Worden, R.H. (eds.) Geological Storage of Carbon Dioxide, vol. Special Publications. pp. 129-146. Geological Society, London (2004)
Holt, T., Vassenden, F.: Physical Gas/Water Segregation Model. In: Skjæveland, S.M., Skauge, A., Hinderaker, L., Sisk, C.D. (eds.) RUTH 1992-1995 - a Norwegian research program on improved oil recovery - program summary. p. 446 s. Norwegian Petroleum Directorate, Stavanger (1996)
Honarpour, M., Koederitz, L., Harvey, A.H.: Relative permeability of petroleum reservoirs. Society of Petroleum Engineers, [S.l.] (1994)
IEA-GHG: New IEA GHG Study Report: 'Aquifer Storage – Development Issues'. Greenhouse Issues **January 2009**(92), 10-12 (2009)
IPCC: Summary for Policymakers. In: Climate Change 1995: The Science of Climate Change. Contribution of Working Group I to the Second Assessment of the Intergovernmental Panel on Climate Change. In: Houghton, J.T., Meira Filho, L.G., Callender, B.A., Harris, N., Kattenberg, A., Maskell, K. (eds.). Cambridge University Press, Cambridge, UK, (1995)
IPCC: Summary for Policymakers. In: Climate Change 2001: The Scientific Basis. Contribution of Working Group I to the Third Assessment Report of the Intergovernmental Panel on Climate Change. In: Houghton, J.T., Ding, Y., Griggs, D.J., Noguer, M., van der Linden, P.J., Dai, X., Maskell, K., Johnson, C.A. (eds.). Cambridge University Press, Cambridge, UK and New York, NY, USA, (2001)
IPCC: IPCC Special Report on Carbon Dioxide Capture and Storage. Prepared by Working Group III of the Intergovernmental Panel on Climate Change. In: Metz, B., Davidson, O., de Coninck, H.C., Loos, M., Meyer, L.A. (eds.). Cambridge University Press, Cambridge, UK and New York, NY, USA, (2005)
Kaviany, M.: Principles of heat transfer in porous media, 2nd ed. Mechanical engineering series. Springer, New York (1995)
Lindeberg, E.: Calculation of thermodynamic properties of CO_2, CH_4, H_2O and their mixtures also including salt with the Excel macro "CO_2 Thermodynamics". In. (2013)

Lindeberg, E., Bergmo, P.: The long-term fate of CO_2 injected into an aquifer. In: Gale, J., Kaya, Y. (eds.) Proceedings of the 6th International Conference on Greenhouse Gas Control Technologies (GHGT-6), Kyoto, Japan. pp. 489-494. Pergamon, v.I, (2003)
Lindeberg, E., Vuillaume, J.-F., Ghaderi, A.: Determination of the CO_2 storage capacity of the Utsira formation. Energy Procedia **1**(1), 2777-2784 (2009). doi:http://dx.doi.org/10.1016/j.egypro.2009.02.049
Little, M.G., Jackson, R.B.: Potential impacts of leakage from deep CO2 geosequestration on overlying freshwater aquifers. Environmental science & technology **44**(23), 9225-9232 (2010)
Løvoll, G., Méheust, Y., Måløy, K.J., Aker, E., Schmittbuhl, J.: Competition of gravity, capillary and viscous forces during drainage in a two-dimensional porous medium, a pore scale study. Energy **30**(6), 861-872 (2005)
Maldal, T., Tappel, I.M.: CO2 underground storage for Snøhvit gas field development. Energy **29**(9–10), 1403-1411 (2004). doi:http://dx.doi.org/10.1016/j.energy.2004.03.074
Marini, L.: Geological Sequestration of Carbon Dioxide: Thermodynamics, Kinetics, and Reaction Path Modeling. Developments in Geochemistry 11, vol. 11. Elsevier, Amsterdam, The Netherlands; Oxford, UK (2007)
Michael, K., Allinson, G., Golab, A., Sharma, S., Shulakova, V.: CO_2 storage in saline aquifers II-Experience from existing storage operations. Energy Procedia **1**(1), 1973-1980 (2009)
Mølnvik, M.J., Berstad, D., Brunsvold, A., Langørgen, Ø., Dahl, P.I., Ditaranto, M., Grimstad, A.-A., Kim, I., Aarlien, R.: BIGCO2 R&D Platform – Objectives and Achievements. Energy Procedia **23**(0), 313-322 (2012). doi:http://dx.doi.org/10.1016/j.egypro.2012.06.078
NOAA Earth System Research Laboratory: http://www.esrl.noaa.gov/gmd/ccgg/trends/. (2014). Accessed February 2014
Nordbotten, J.M., Celia, M.A., Bachu, S.: Injection and Storage of CO_2 in Deep Saline Aquifers: Analytical Solution for CO_2 Plume Evolution During Injection. Transport in Porous Media **58**(3), 339-360 (2005)
Pamukcu, Y., Hurter, S., Jammes, L., Vu-Hoang, D., Pekot, L.: Characterizing and predicting short term performance for the In Salah Krechba field CCS joint industry project. Energy Procedia **4**(0), 3371-3378 (2011). doi:http://dx.doi.org/10.1016/j.egypro.2011.02.259
Pearce, J., Czernichowski-Lauriol, I., Lombardi, S., Brune, S., Nador, A., Baker, J., Pauwels, H., Hatziyannis, G., Beaubien, S., Faber, E.: A review of natural CO_2 accumulations in Europe as analogues for geological sequestration. In: Baines, S.J., Worden, R.H. (eds.) Geological Storage of Carbon Dioxide, vol. Special Publications. pp. 29-41. Geological Society, London (2004)
Polak, S., Cinar, Y., Holt, T., Torsæter, O.: An experimental investigation of the balance between capillary, viscous, and gravitational forces during CO_2 injection into saline aquifers. Energy Procedia **4**, 4395-4402 (2011). doi:10.1016/j.egypro.2011.02.392
Polak, S., Grimstad, A.-A.: Reservoir simulation study of CO_2 storage and CO_2-EGR in the Atzbach-Schwanenstadt gas field in Austria. Energy Procedia **1**(1), 2961-2968 (2009). doi:DOI: 10.1016/j.egypro.2009.02.072
Riddiford, F.A., Tourqui, A., Bishop, C.D., Taylor, B., Smith, M.: A Cleaner Development: The in Salah Gas Project, Algeria. In: Gale, J., Kaya, Y. (eds.) Greenhouse Gas

Control Technologies - 6th International Conference. pp. 595-600. Pergamon, Oxford (2003)
Rochelle, C.A., Czernichowski-Lauriol, I., Milodowski, A.E.: The impact of chemical reactions on CO_2 storage in geological formations: a brief review. In: Baines, S.J., Worden, R.H. (eds.) Geological Storage of Carbon Dioxide, vol. Special Publications. pp. 87-106. Geological Society, London (2004)
Rumpf, H., Gupte, A.R.: The influence of porosity and grain size distribution on the permeability equation of porous flow. Chemie Ing. Techn. (Weinheim) (Transl. into ENGLISH) **43**(6), 367-375 (1975)
Saadatpoor, E., Bryant, S.L., Sepehrnoori, K.: Effect of Heterogeneous Capillary Pressure on Buoyancy-Driven CO_2 Migration. Paper presented at the SPE/DOE Symposium on Improved Oil Recovery, 20-23 April 2008, Tulsa, Oklahoma, USA,
Schechter, D.S., Zhou, D., Orr Jr, F.M.: Capillary Imbibition and Gravity Segregation in Low IFT Systems. Paper presented at the SPE Annual Technical Conference and Exhibition, Dallas, Texas, 01/01/1991
Span, P., Wagner, W.: A new equation of state for carbon dioxide covering the fluid region from the triple point temperature to 1100K at pressures up to 800MPa. Journal of Physical Chemistry **25-6**, 1509-1596 (1996)
Spivey, J., Mccain, W., North, R.: Estimating density, formation volume factor, compressibility, methane solubility, and viscosity for oilfield brines at temperatures from 0 to 275 C, pressures to 200 MPa, and salinities to 5.7 mole/kg. Journal of Canadian Petroleum Technology **43**(7), 52-61 (2004)
Stocker, T.F., D. Qin, G.-K. Plattner, L.V. Alexander, S.K. Allen, N.L. Bindoff, F.-M. Bréon, J.A. Church, U. Cubasch, S. Emori, P.F., P. Friedlingstein, N. Gillett, J.M. Gregory, D.L. Hartmann, E. Jansen, B. Kirtman, R. Knutti, K., Krishna Kumar, P.L., J. Marotzke, V. Masson-Delmotte, G.A. Meehl, I.I. Mokhov, S. Piao, V. Ramaswamy, D., Randall, M.R., M. Rojas, C. Sabine, D. Shindell, L.D. Talley, D.G. Vaughan and S.-P. Xie (eds.): Technical Summary. Cambridge University Press, Cambridge, United Kingdom and New York, NY, USA (2013)
Stumm, W., Morgan, J.J.: Aquatic chemistry: chemical equilibria and rates in natural waters, 3rd ed. Environmental science and technology. Wiley, New York (1996)
Taku Ide, S., Jessen, K., Orr Jr, F.M.: Storage of CO_2 in saline aquifers: Effects of gravity, viscous, and capillary forces on amount and timing of trapping. International Journal of Greenhouse Gas Control **1**(4), 481-491 (2007)
U.S. EPA: Carbon Dioxide as a Fire Suppressant: Examining the Risks. (2000). 2014
Wendland, M., Hasse, H., Maurer, G.: Experimental pressure-temperature data on three-and four-phase equilibria of fluid, hydrate, and ice phases in the system carbon dioxide-water. Journal of Chemical & Engineering Data **44**(5), 901-906 (1999)
Zweigel, P., Arts, R., Lothe, A.N., Lindeberg, E.: Reservoir geology of the Utsira formation at the first industrial-scale underground CO_2 storage site (Sleipner area North Sea). In: Baines, S.J., Worden, R.H. (eds.) Geological Storage of Carbon Dioxide, vol. Special Publications. pp. 165-180. Geological Society, London (2004)

Paper I

Available online at www.sciencedirect.com
ScienceDirect
Energy Procedia 1 (2009) 2961–2968
Energy Procedia
www.elsevier.com/locate/procedia

GHGT-9

Reservoir simulation study of CO_2 storage and CO_2-EGR in the Atzbach-Schwanenstadt gas field in Austria

Szczepan Polak [a]*, Alv-Arne Grimstad [a]

[a] *SINTEF Petroleum Research, 7465 Trondheim, Norway*

Abstract

The Atzbach-Schwanenstadt gas field has been investigated in the CASTOR project with respect to its suitability for safe, long-term underground CO_2 storage.
Storage capacity of the reservoir has been estimated to 14.5 million tonnes of CO_2. Potential nearby CO_2 sources emit together about 300 000 tonnes of CO_2 per year. Assuming that reservoir would be filled up until its initial reservoir pressure the available storage capacity would be sufficient to store all CO_2 produced during the next 48 years. Results from the reservoir simulation of the storage showed that during 30 years of injection 8.2 million tonnes of CO_2 could be stored.
A CO_2-EGR effort in the field could in theory increase gas production and therefore enlarge the available storage capacity for CO_2. However, none of the conducted reservoir simulations could prove that CO_2 injection would enhance gas recovery at the Atzbach-Schwanenstadt field. CO_2 breakthrough to the production wells is very quick and occurs almost immediately after start of injection. The fraction of CO_2 in produced gas increases rapidly and this limits production of the clean gas. Compared to the simulation with no CO_2 injection, EGR cases give lower production of the clean gas. Therefore use of CO_2 for the enhanced gas recovery is not recommended for the Atzbach-Schwanenstadt field.
The long-term storage simulation shows that reservoir pressure stabilizes shortly after injection stops. During the period of 1500 years after the end of injection only 10% of injected CO_2 will dissolve in the immobile reservoir water.
In a scenario of potential leakage four abandoned wells were selected to mimic leaking wells. Simulation results show that if CO_2 reaches the abandoned wells, and this would lead to leakage, as much as 5.6% of injected CO_2 could escape from the reservoir during a period of 1500 years.

Keywords: CO_2 storage; CASTOR; Atzbach-Schwanenstadt; Reservoir Simulation; Long-term simulation

1. Introduction

As one of four case studies, the Atzbach-Schwanenstadt gas field, located in Upper Austria and operated by Rohöl-Aufsuchungs AG (RAG), has been investigated in the CASTOR project with respect to its suitability for safe,

* Corresponding author. Tel.: +47-95205446; fax: +47-73591246.
E-mail address: Szczepan.Polak@iku.sintef.no

doi:10.1016/j.egypro.2009.02.072

long-term underground CO_2 storage. This paper presents results of the reservoir simulations of short and long term CO_2 injection predictions as well as evaluation of potential for enhanced gas recovery (EGR).

2. Methodology

All simulations were performed using the compositional simulator Eclipse 300. An eight-component description (including CO_2) is used for the reservoir gas. Petrel software was used for construction of the geological model, data integration, history matching analysis and results visualization of the CO_2 injection simulations.

3. Input data

In order to quantify the amount of CO_2 that can be stored in the reservoir, a geological model of the area has been made [1] on which a simulation model was based. The digital geological model ranges from the base of Hall Formation (Miocene) to upper Eocene (Figure 4.1.a), with a special focus on the main reservoir zone of the Upper Puchkirchen Formation (from Oligocene to Miocene) [1]. The reservoir simulation model focuses on the zone A4 (Figure 4.1.b) which includes only the central part of the field, where gas productivity is best and a relatively uniform gas-water contact exists. The top of the reservoir is limited by the 'gas-top' surface (Figure 4.1.b). This surface is constructed from the well observation of the uppermost occurrence of the hydrocarbon gas in wells [2].

4. History matching simulation

Production from the field started in 1963 and this was also the start of the history matching simulation. The last production report used in the simulation was from December 2006. Since the field is still in production it has been assumed that reservoir simulation should continue until 2010 before possible CO_2 injection could take place. There were 28 wells producing during the history of the field. The volume of the gas initially in place (GIIP) provided by RAG was estimated to be 4 353 million Sm^3. The total observed field gas production by December 2006 was 3 666 million Sm^3 [3].

The input parameter used for the history matching was the observed gas production in the wells. In the history matching the intention was to obtain a match of the GIIP and wells bottom hole pressure (BHP). Due to the fact that water in the reservoir was highly immobile the volume of produced water was negligibly small. Therefore water production was not taken into consideration in the history matching.

Since the reservoir boundaries are not exactly defined in the geological model the reservoir model has been divided into two regions. For the GIIP calculation the Region 1 indicated in Figure 4.2 has been used, as suggested by RAG. The remaining part of the model – Region 2 – has been set to low permeability so any gas inflow from this part of the model to the GIIP region is negligible.

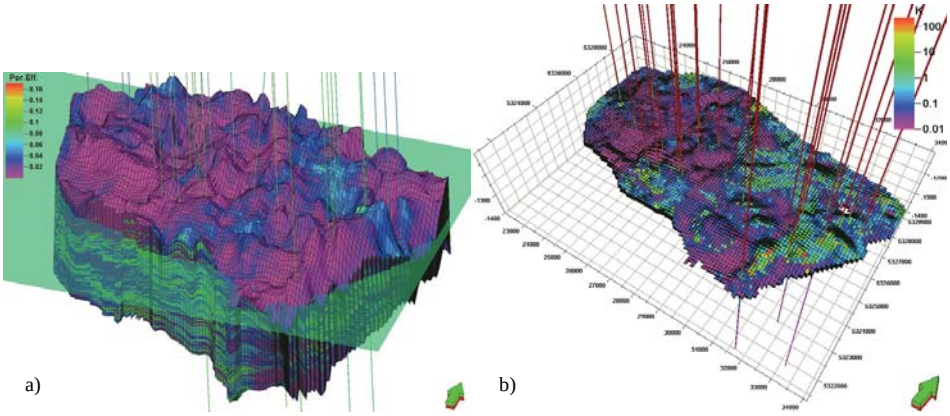

Figure 4.1. a) Effective porosity model showing the locations of producing wells in the field [2]; color scale represents effective porosity; the transparent green plane shows gas-water contact at 1210 mss; vertical exaggeration=20x. b) Simulation grid showing the A4 zone above the gas-water contact and below gas-top surface [2]; color scale represents horizontal permeability; vertical exaggeration=10x.

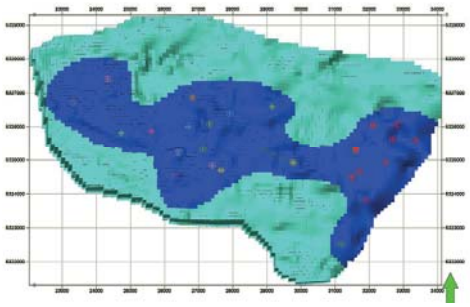

Figure 4.2. Top view of the reservoir model [2]; the dark blue area (Region 1) represents the part of the field used in GIIP calculation; the light blue area represents the low-permeability outer part (Region 2); symbols show well head location of the production wells.

5. CO_2 storage and EGR

5.1. CO_2 storage capacity

Calculation of the CO_2 storage capacity of the Atzbach-Schwanenstadt field was based on the volume of produced gas. It was estimated that pore volume available for CO_2 storage corresponds to as much as 14.5 million tonnes of CO_2. However, the actual capacity will be lower and will depend on injection rate as well as location and number of injection wells. Low permeability will limit the distribution of the CO_2 in the reservoir and therefore not all available pore space will be reached by injected CO_2.

Potential nearby CO_2 sources are a paper mill and a fertilizer plant. Combined, they emit about 300 000 tonnes of CO_2 per year, and thus the available storage capacity would be sufficient to store all CO_2 produced during the next 48 years assuming that reservoir would be filled up until its initial reservoir pressure. The reservoir storage capacity as a function of reservoir pressure is presented in Figure 5.3.

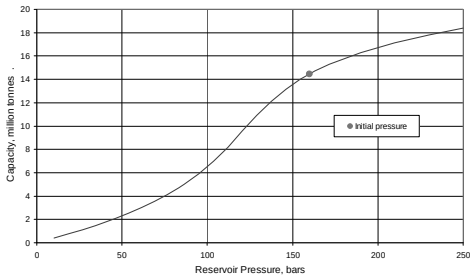

Figure 5.3. The Atzbach-Schwanenstadt CO_2 storage capacity vs. reservoir pressure.

5.2. CO_2 storage and EGR simulations

The paper mill and fertilizer plant together can deliver up to 300 000 tonnes of CO_2 per year to the site. This gives a daily injection rate of approximately 820 tonnes. This volume of CO_2 could be injected using only one injection well. However, it was assumed that pressure in the reservoir during CO_2 injection should not exceed initial reservoir pressure in order to prevent possible seal fracturing. Therefore, in order to make injection safe, the BHP limit for injection wells has been set to the initial reservoir pressure of 160 bars. Also, if the EGR is going to be applied then several injection wells should be considered in order to make the EGR process more efficient.

Four different injection scenarios were investigated, with and without EGR, and with injection into old or new wells. CO_2 injection started in 2010 in all simulation cases and it lasted 30 years.

Results from the storage base case show that 8.2 million tonnes of CO_2 could be stored during 30 years of injection (Figure 5.4.a). In this scenario, injection rates need to be reduced towards the end of the injection period in order to keep injection pressure below the initial reservoir pressure.

The goal of the EGR simulation was to find out if CO_2 injection can stimulate (increase) gas production. Re-injection of produced CO_2 was not considered. Two economic limits were set on gas production wells from 2010: 1) if the gas production falls below 525 Sm^3/day then the production well is shut (economic limit given by RAG) and 2) if the mole fraction of CO_2 in produced gas increases above 50% then well connections which exceed this limit will be shut.

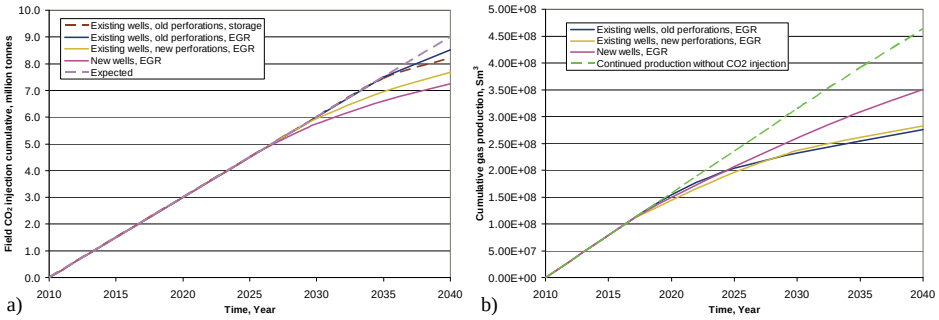

Figure 5.4. a) Field CO_2 injection cumulative; for comparison curve named 'Expected' shows cumulative CO_2 injection with rate of 300 000 tonnes per year [2]. b) Cumulative gas production after 2010 in EGR simulations and without CO_2 injection [2].

A CO_2-EGR effort in the field could in theory increase gas production and therefore enlarge the available storage capacity for CO_2. However, none of the conducted reservoir simulations could prove that CO_2 injection would enhance gas recovery at the Atzbach-Schwanenstadt field (see Figure 5.4.b). CO_2 breakthrough to the production wells is very quick and occurs almost immediately after start of injection. The fraction of CO_2 in produced gas increases rapidly and this limits production of the clean gas. Compared to the simulation with no CO_2 injection, EGR cases give lower production of the clean gas. Therefore use of CO_2 for the enhanced gas recovery is not recommended for the Atzbach-Schwanenstadt field.

6. Long term reservoir simulation

The goal of the long term reservoir simulation was to investigate fate of the CO_2 in the reservoir after completion of the storage process. The study focused on pressure changes and CO_2 concentration distribution in the reservoir. In addition to the case were CO_2 behaviour in the reservoir was tracked during the first 1500 years after injection, two hypothetical leakage scenarios have been considered. All long term simulations were continuations of the storage base case presented in chapter 5.2.

6.1. Long term storage

Due to differences in injectivity for the three injection wells (Figure 6.6), there was considerable variation in the pressure in Region 1 at the end of injection. The pressure in the compartment where well ISCH-015 is located reaches the maximum allowed pressure of 160 bar while pressure around the other two injection wells was lower. Simulation shows that after stop of injection movement of gas in the reservoir evens out this pressure variation (Figure 6.5.a). Pressure equilibration between Region 1 and Region 2 takes longer time and is still ongoing after 1500 years (Figure 6.5.a, Figure 6.6.a and b). During period of 1500 years after the end of injection only 10% (Figure 6.5.b) of the injected CO_2 will dissolve in the immobile reservoir water.

The movement of gas due to lateral pressure gradients also causes a re-distribution of the injected CO_2. A large increase in the mole fraction of CO_2 in the reservoir gas is observed in a region midway between wells IATZ-002 and ISCH-015 (Figure 6.6.c and d). After the first 500 years, when the pressure gradient almost has disappeared (Figure 6.5.a), the changes are much slower.

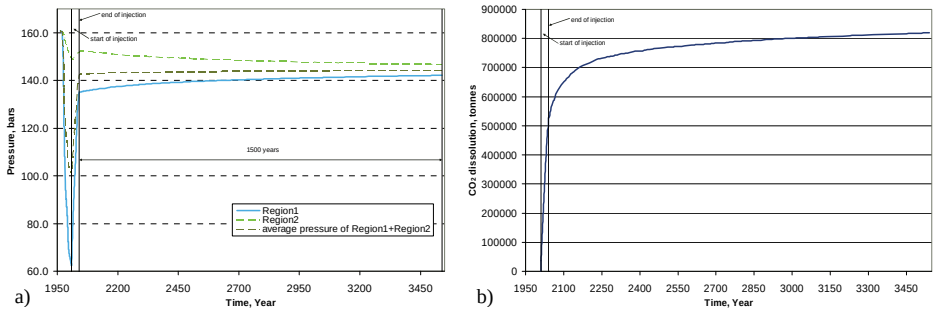

Figure 6.5. a) Reservoir pressure development during gas production, CO_2 injection and long-term CO_2 storage [4]. b) CO_2 dissolution in the reservoir water [4].

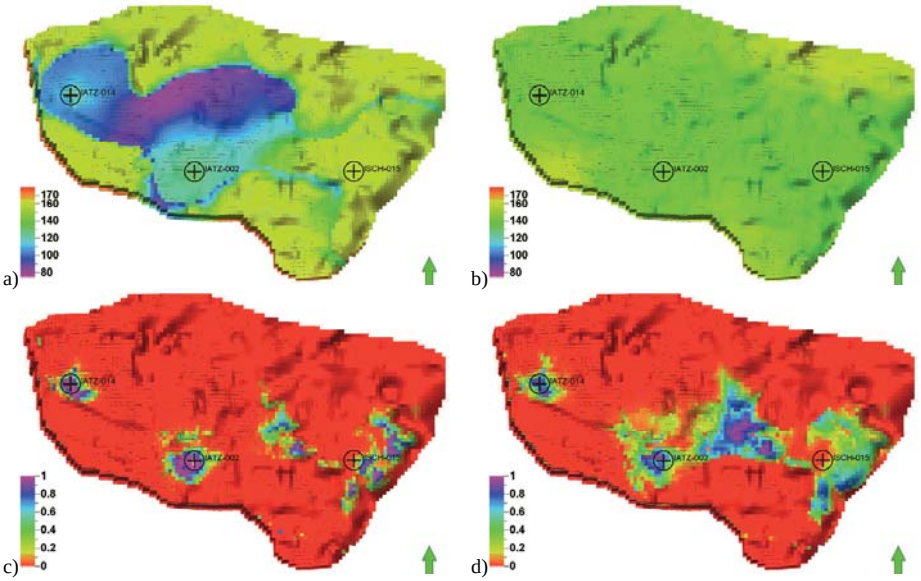

Figure 6.6. Reservoir pressure at the end of injection (a) and after 1500 years from the end of injection (b) [4]. CO_2 mole fraction distribution in the reservoir at the end of injection (c) and after 1500 years from the end of injection (d) [4].

6.2. Leakage simulations

Re-distribution of the injected CO_2 may lead to contact with wells abandoned according to regulations that do not consider exposure to CO_2. Therefore two hypothetical leakage scenarios have been investigated where such wells start leaking when the CO_2 concentration around them exceeds 10%: 1) leakage controlled by limit on BHP and rate

of leaked gas and 2) leakage controlled only by limit on BHP. It is assumed that even if leakage occurs it will not be large enough to cause significant change in the reservoir pressure close to the leaking well. Thus, in the simulations BHP is not allowed to fall below 90 bars. This is close to the pressure around the four potentially leaking wells at the end of the injection period.

In the leakage scenarios it is seen that only one well, ATZ-004, is contacted by CO_2 in high enough concentrations to trigger significant leakage (Figure 6.7.a). This happens approximately 60 years after end of injection (Figure 6.7.b). This well then continues to leak throughout the studied post-injection period, with a gradually higher volume fraction of CO_2. The leaked fraction after 1500 years is approximately 5.6% of the stored CO_2 (Figure 6.7.b).

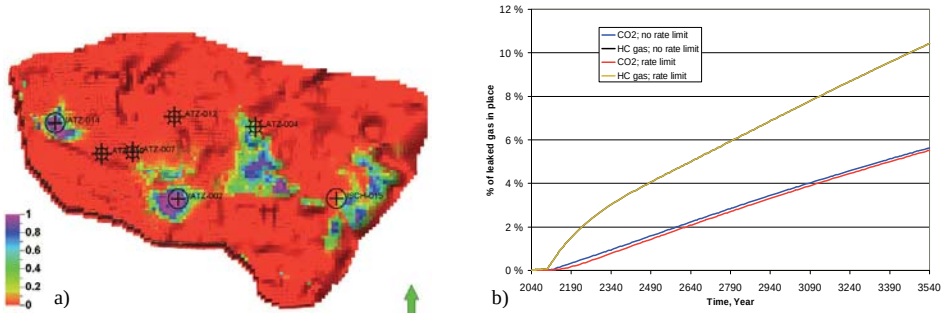

Figure 6.7. a) CO_2 mole fraction distribution in the reservoir during leakage 50 years after the end of injection [4]. b) Cumulative leakage of CO_2 and HC gas in fraction of amount present in the reservoir at the end of injection period; note that two curves for HC gas overlap each other [4].

7. Discussion and conclusions

The Atzbach-Schwanenstadt gas field offers promising potential for CO_2 storage. Its total available storage capacity of 14.5 million tons of CO_2 would be sufficient to store all CO_2 produced during the next 48 years by the nearby paper mill and fertilizer plant. However, the actual capacity will be lower and will depend on injection rate as well as location and number of injection wells. Low permeability will limit the distribution of the CO_2 in the reservoir therefore not all available pore space will be reached by injected CO_2.

A CO_2-enhanced gas recovery effort in the field could in theory increase gas production and therefore enlarge the available storage capacity for CO_2. However, none of the conducted reservoir simulations could prove that CO_2 injection would enhance gas recovery. Injected CO_2 breakthrough to the production wells is very quick and occurs almost immediately after start of injection. Content of the CO_2 in produced gas increases rapidly and this limits production of the clean gas. Compared to the simulation with no CO_2 injection, EGR cases give lower production of the clean gas. Therefore use of CO_2 for the enhanced gas recovery is not recommended for the Atzbach-Schwanenstadt field. Possibly, positive effect of the CO_2 use for EGR could be obtained after the field would become depleted and could not produce with economical rates. Then CO_2 injection would increase reservoir pressure and this could stimulate gas production. Nevertheless high contamination of produced gas by CO_2 should be expected.

Long term simulation shows that after stop of injection movement of gas in the reservoir evens out pressure variation. Pressure equilibration between Region 1 and Region 2 takes longer time and is still ongoing after 1500

years. During the period of 1500 years after the end of injection only 10% of the injected CO_2 will dissolve in the immobile reservoir water.

Regarding potential leakage, it is expected that the Atzbach-Schwanenstadt as a natural gas reservoir will be safe for CO_2 storage as long as the CO_2 injection does not increase the reservoir pressure above the initial pressure and the integrity of the wells will be kept.

In the potential leakage scenarios it is seen that only one well is contacted by CO_2 in high enough concentrations to trigger significant leakage. The simulated leakage rates would be enough to fill an average-sized house per day. Apart from this simple calculation, however, the HSE impact of the leaking CO_2 has not been investigated further in the present study.

Acknowledgements

The CASTOR project has been founded by the European Union together with industrial partners. The support by the project partners is gratefully acknowledged.

References

1. J. Zweigel, S. Pannetier-Lescoffit, S. Mjaaland, P. Zweigel, S. Polak, Geological subsurface model for the Atzbach-Schwanenstadt gas field (Austria) - A contribution to the CASTOR project, Report 54.5306.00/01/05, SINTEF Petroleum Research, Trondheim, Norway, 2005.
2. S. Polak, Reservoir simulation for the Atzbach-Schwanenstadt gas field (Austria) - A contribution to the CASTOR project, Report 54.5306.50/03/08, SINTEF Petroleum Research, Trondheim, Norway, 2008.
3. T. Clemens, Atzbach - Schwanenstadt status quo A2/1 sands, Report AG-B-09-2004, Rohöl-Aufsuchungs AG (RAG),Vienna, Austria, 2004.
4. S. Polak, A.-A. Grimstad, Long-term reservoir simulation for the Atzbach-Schwanenstadt gas field (Austria) - A contribution to the CASTOR project, Report 54.5306.50/04/08, SINTEF Petroleum Research, Trondheim, Norway, 2008.

Paper II

Available online at www.sciencedirect.com
ScienceDirect
Energy Procedia 4 (2011) 4395–4402
Energy Procedia
www.elsevier.com/locate/procedia

GHGT-10

An experimental investigation of the balance between capillary, viscous, and gravitational forces during CO_2 injection into saline aquifers

Szczepan Polak[a,b,c,d,*], Yildiray Cinar[c,d], Torleif Holt[a] and Ole Torsæter[b]

[a]*Department of Petroleum Engineering and Applied Geophysics, Norwegian University of Science and Technology (NTNU), NO-7491 Trondheim, Norway*
[b]*Seismic and Reservoir Technology Department, SINTEF Petroleum Research, P.O. Box 4763 Sluppen, NO-7465 Trondheim, Norway*
[c]*Cooperative Research Centre for Greenhouse Gas Technologies (CO2CRC), GPO Box 463, Canberra, ACT 2601, Australia*
[d]*The School of Petroleum Engineering, The University of New South Wales (UNSW), Sydney NSW 2052, Australia*

Abstract

Understanding of the processes which take place within a reservoir during and after CO_2 injection is essential for successful selection of a storage site for carbon capture and storage. Flow regimes that occur when CO_2 is injected into a geological formation control how much CO_2 can be effectively injected and stored in the formation. This paper presents an experimental investigation of the scaling laws which describe CO_2 injection into saline aquifers. Quasi two-dimensional experiments were performed in initially water-filled glass-bead packs to demonstrate the influence of gravitational, viscous and capillary effects on the vertical flow of CO_2. The properties of fluids used in the experiments are analogous to the properties of CO_2 and brine at possible reservoir conditions. Experiments are performed for a range of dimensionless capillary and CGR numbers which may describe conditions at existing storage sites. The use of dimensionless numbers links the laboratory experiments with the field scale observations and hence these numbers can be applied for the screening of potential storage sites. The experiments represent gravity and viscous unstable floods with fractal-like fronts. The gravity effects were more pronounced in cases with a low injection rate and high permeability, causing less brine displacement. Higher injection rates caused more fingering and increased total displacement.

CO_2 storage, dimensionless numbers, glass-bead packs, analogous fluids

* Corresponding author. Tel.: +47 73591398; fax: +47 73591246.
e-mail address: szczepan.polak@ntnu.no

doi:10.1016/j.egypro.2011.02.392

1. Introduction

Selection of a geological storage site for carbon capture and storage must be preceded by accurate understanding of the flow processes that take place within the reservoir during and after CO_2 injection. The characteristics of flows that occur when CO_2 is injected into a deep geological formation control how much CO_2 can be effectively injected and stored within the formation. There have been numerous analytical and numerical studies on site characterization for CO_2 injection/storage based on scaling laws [1-3] that characterize the simultaneous flow of CO_2-brine in subsurface formations. However, little experimental data have been reported that shed light on the nature of the drainage process which applies to the CO_2 injection [4]. This paper presents an experimental investigation of the scaling laws which describe CO_2 injection into saline aquifers.

Quasi two-dimensional experiments were performed in initially water-filled glass-bead packs that demonstrate the influence of gravitational, viscous and capillary effects on the vertical flow of CO_2. Models used in experiments represent a homogeneous porous medium. Analogous fluids were used in the experiments and their properties correspond to the properties of CO_2 and brine at possible reservoir conditions. Experiments are described by dimensionless capillary and capillary-to-gravity-ratio (CGR) numbers which incorporate fluid and rock properties.

Flow regimes that occur when CO_2 is injected into a deep geological formation control how much CO_2 can be effectively injected and stored in the formation. Reservoir parameters such as depth, temperature, permeability and capillary pressure have great influence on CO_2 flow within a reservoir. Therefore experiments are performed for a range of capillary and CGR numbers which may describe conditions at existing storage sites. The use of dimensionless numbers links the laboratory experiments with the field scale observations and hence these numbers can be applied for the screening of potential storage sites.

2. Experimental setup

Synthetic porous medium and analogous fluids were used in the experiments. The porous medium was made of two vertical glass plates with space between them which was packed with glass beads. A glass bead model of uniform bead size represented a homogeneous porous medium. The glass-bead size controlled the permeability of the bead packs.

Analogous liquids were used in the experiments - a mixture of distilled water and glycerol, and n-heptane. This mixture separates into two phases at ambient conditions and, unlike the CO_2-brine system, allows the phase properties to be varied simply by changing the compositions. The analogy was made based on the comparisons of density difference and viscosity ratios as well as capillary and CGR numbers calculated from the physical properties of both the analogous liquids at ambient conditions and CO_2-brine systems at possible reservoir conditions [5, 6]. The n-heptane-rich phase is less dense and less viscous than the glycerol-rich phase and represents the CO_2 while the glycerol-rich phase is analogous to the aquifer brine. The density difference of 476 kg/m^3 between the analogous fluids falls in the range of the density difference between CO_2 and brine at possible reservoir conditions while the viscosity ratio of 30.8 of the phases stays within the range of the viscosity ratios at reservoir conditions for CO_2-brine systems [5]. The interfacial tension for the analogous fluids is measured to be 34 mN/m and is within a range of values (27-49 mN/m) measured for CO_2 and brine at in-situ conditions [7].

The quasi two-dimensional, vertical glass model used in experiments was packed with glass beads. Physical properties of the experimental model are presented in Table 1. The glass-bead model was initially saturated with a mixture of glycerol and water, which is analogous to brine. The red dyed n-heptane-rich phase, analogous to CO_2, was injected from the bottom of the model to displace glycerol-rich water. One pore volume (PV) of the n-heptane-rich phase was injected at a constant rate in every experiment. The produced fluids were collected at the top of the model. During experiments the injection pressure, the mass of the injected and produced fluids and the breakthrough time were recorded. In order to visualize the changes in saturations, pictures were taken during the experiments. The schematic of the experimental setup is shown in Figure 1.

Table 1 Physical properties of the experimental model.

Height [cm]	31.13
Distance from inlet to outlet [cm]	29.60
Width [cm]	29.75
Thickness [cm]	0.19
Pore volume [cm^3]	67.75

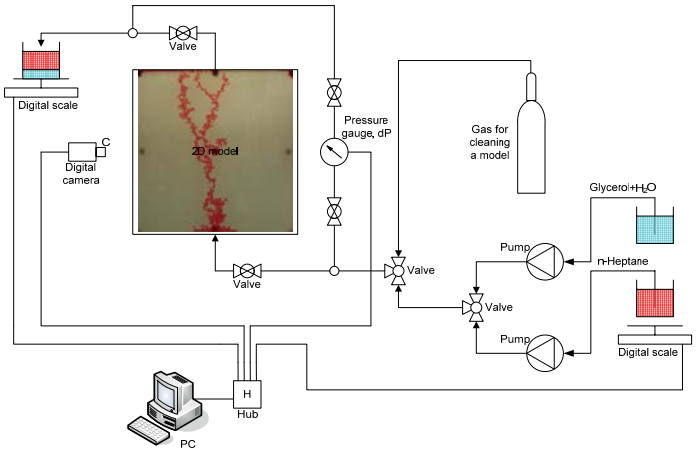

Figure 1 Schematic of the experimental setup.

3. Experiments

The experiments were performed at ambient conditions. Only permeability (k) and injection rate (q) were varied and all the other parameters were kept constant. The red dyed n-heptane-rich phase (CO_2) was injected into the model which was fully saturated with the glycerol-rich phase (aquifer brine). Table 2 lists the properties of fluids used in experiments.

Table 2 Properties of fluids used in experiments.

Fluid	Density [kg/m^3]	Viscosity [mPa·s]
glycerol-rich phase (brine)	1160.4	12.557
n-heptane-rich phase (CO_2)	684.5	0.408

The porosity of the model was measured to be 0.39 which was consistent with theoretical value for the glass beads poured into a bed (random packing) [8]. Two different sizes of glass beads were used: 0.2 mm and 0.4 mm.

These correspond to the theoretical permeability of 40.2 and 161.0 Darcy, respectively. The permeability was calculated with Rump and Gupte equation [9]:

$$k = \frac{\phi^{5.5}}{5.6} d^2 \quad (1)$$

where: ϕ - porosity; d - glass bead diameter, m.

Table 3 states the different scenarios of various permeability and injection rates which were investigated and the parameters used in calculations. There were 14 experiments performed in total and here the averaged results are presented for each case. Note that the *low k, high q* scenario has not been successfully performed due to the high pressure increase which could cause the model to burst. Also due to slightly higher permeability along the boundaries of the model and therefore preferential flow path, after the breakthrough, sometimes part of the injected fluid went along boundaries which affected the displacements. This however had no influence on the results of the experiments and final calculations of the presented cases but was a major issue in the attempts to perform the *low k, high q* case.

For a given fluid system, only permeability and flow velocity controlled the dimensionless parameters, hence only these parameters were varied to obtain different dimensionless numbers. The capillary number (N_C) is defined as the ratio of viscous to capillary forces:

$$N_C = \frac{u \cdot \mu_i}{\gamma} \quad (2)$$

where: u - flow velocity, m/s, defined as $u=q/A$, with A being the cross-sectional area of the model, m^2; μ_i - viscosity of injected fluid, Pa·s; γ - interfacial tension (IFT), N/m. The range of the flow velocities (from 0.26 to 1.29 m/day) used in calculations for storage sites is assumed to be the same as in the laboratory experiments.

The capillary to gravity force ratio (CGR) [10] is defined as:

$$CGR = \frac{2\gamma}{\Delta\rho \cdot g \cdot h \cdot \sqrt{\frac{k}{\phi}}} \quad (3)$$

where: $\Delta\rho$ - density difference of the fluids, kg/m^3; g - acceleration of gravity, m/s^2; h – distance between model's inlet and outlet or formation thickness in the reservoir, m.

Table 3 Sets of experimental parameters and dimensionless numbers calculated for the experiments.

Case	Case description	Glass bead diameter, d [mm]	Permeability, k [D]	Porosity, ϕ	Injection rate, q [cm^3/min]	Flow velocity, u [m/s] ($\cdot 10^{-6}$)	CGR	N_C ($\cdot 10^{-6}$)	$N_C \cdot CGR$ ($\cdot 10^{-6}$)
1A	low k, low q	0.2	40.2	0.39	0.10	2.99	4.8440	0.0358	0.1736
1B	low k, mid q	0.2	40.2	0.39	0.25	7.47	4.8440	0.0896	0.4340
2A	high k, low q	0.4	161.0	0.39	0.10	2.99	2.4220	0.0358	0.0868
2B	high k, mid q	0.4	161.0	0.39	0.25	7.47	2.4220	0.0896	0.2170
2C	high k, high q	0.4	161.0	0.39	0.50	14.93	2.4220	0.1792	0.4340

4. Results of the experiments

Figure 2 shows the changes in saturation during injection (pictures taken after injection of 0.01, 0.10, 0.50 and 1.00 PV, and at the moment of breakthrough). Experiments represent gravity and viscous unstable floods. In all displacements fractal-like fronts can be observed. The flow paths are shorter in the high-permeability cases than in low permeability ones. Saturation changes during the experiments were calculated from mass balance of the injected and produced fluids, and density difference of the fluids. However, it is not straightforward to see the saturation changes by inspection of the pictures due to the resolution.

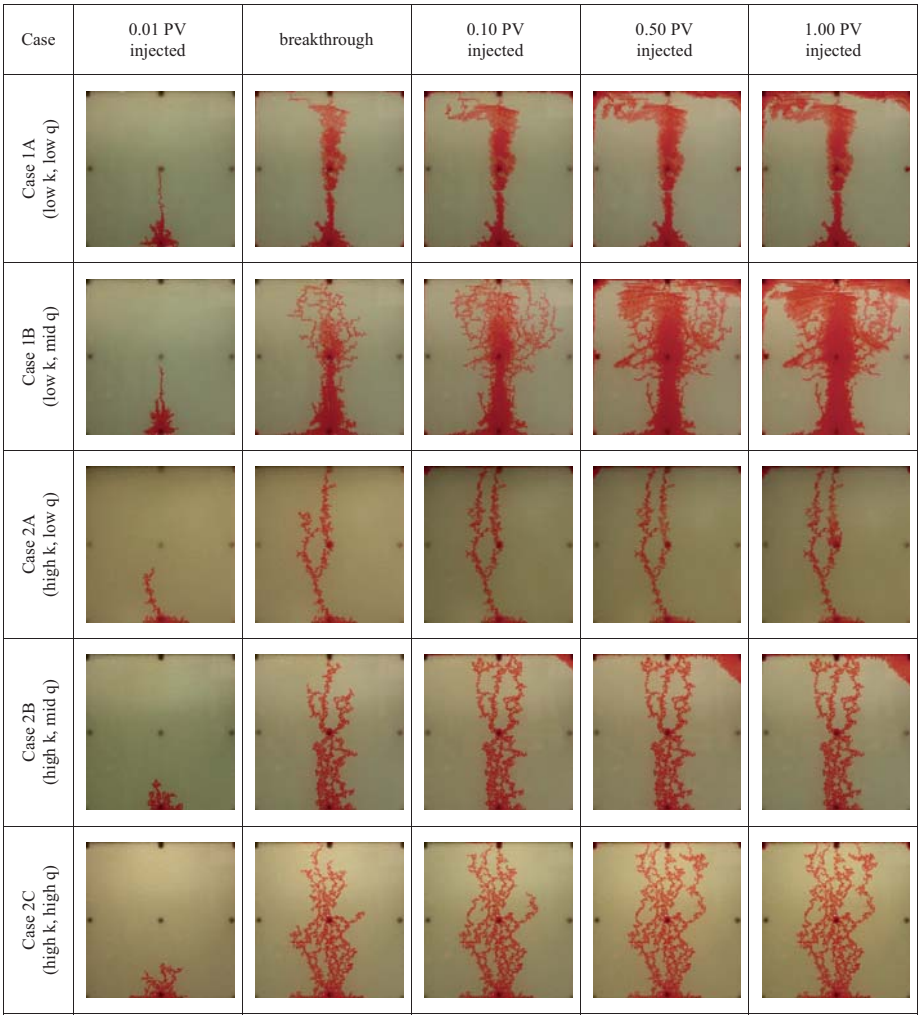

Figure 2 Examples of saturation maps at different stages of displacement. Figures are representative for experiments within each case.

At the *high k, low q* (Case 2A) the plume of the injected fluid was the narrowest. This is mainly because gravity effects were more pronounced in this case than in the others, forcing the fluid to flow more in the vertical direction (Figure 2, Case 2A). As a result, less volume of the in-situ fluid was displaced compared to the *high k, mid* and *high q* cases (Figure 2, Figure 3a, Cases 2B and 2C).

When the injection rate was raised, the impact of viscous forces increased resulting in a larger plume and growth in recovery (Figure 2 and Figure 3a). At *high k, high q* (Case 2C) the plume's lateral extent became larger and the flow paths at the front became longer than in other *high k* cases (Figure 2). Consequently, a large part of the brine was bypassed resulting in an early breakthrough. However, at later times, a lot of the bypassed brine was also produced and Case 2C obtained the highest recovery in all *high k* cases. Comparing results from cases with the same injection rate and different permeability (Case 1A vs. Case 2A and Case 1B vs. Case 2B, Figure 3a) it is apparent that *low k* cases have higher sweep efficiency in the displaced area.

Figure 3b shows the relation between the brine displaced and the $CGR \cdot N_C$ number which is the ratio of viscous forces and gravity forces. The results show that the brine displaced after 1 PV of n-heptane has been injected decreases as the gravity control in the displacement increases. The reason for this observation is that gravity instability creates smaller plume, thus shorter flow paths, compared to the viscous instability. In case of brine displacement at the breakthrough there is no clearly visible regularity. Although volumes of displaced brine at the breakthrough in presented cases seem rather random, with no clear dependency on the $CGR \cdot N_C$ number, the absolute differences are not large and values of displaced volumes are close to each other.

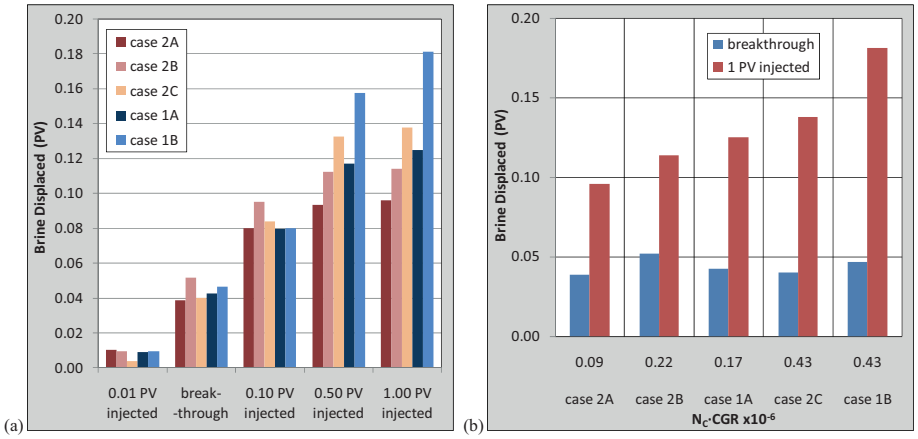

Figure 3 Brine displacement (a) and dimensionless numbers vs. recovery (b). Note that in (b) cases are ordered by increasing final recovery and not by $N_C \cdot CGR$ parameter.

Figure 4a shows CGR and $N_C \cdot CGR$ numbers calculated for the experiments and field cases. The input parameters for sedimentary basins were obtained from [5]. The authors provided eight sets of properties based on following parameters: depth (1000 and 3000 m, and pressure gradient of 10.5 MPa/km), temperature (gradient of 25 and 45 °C/km), and brine salinity. These properties determine the conditions in the reservoir formations and thus CO_2 viscosity and density, and IFTs. The generic storage formation in this study is assumed to have porosity of 15 %, permeability of 20 mD, and thickness of 30 m. Parameters used in calculations of dimensionless numbers for existing storage sites are obtained from [6]. Calculations for both, the storage sites and sedimentary basins, are made for the range of the flow rates used in the experiments. IFT is calculated according to the equation $IFT=59.335/P^{0.2446}$ (P - formation pressure, MPa) from [11]. The large difference between basins and existing storage sites that can be seen in Figure 4a is caused mainly by two parameters: permeability and formation thickness. By increasing them, basins would be shifted on the plot towards existing storage sites leaving behind the experiments. In order to get experiments scaled closer to the storage sites the fluid system has to be changed to a system with significantly lower IFT, e.g. around 1 mN/m.

Figure 4b shows forces that govern fluid flow in the reservoir and direction of the increase of their importance. As could be expected, in the Sleipner case (Figure 4a), gravity forces have significant influence on flow of CO_2 due to reservoir's high permeability (~5 D) and thickness (~250 m). On the contrary, the laboratory experiments are dominated by viscous and especially capillary forces, mainly due to the high IFT of the used fluids. Nevertheless, the experimental CGR and $N_C \cdot CGR$ numbers at the high permeability and low injection rate agree reasonably well with calculations for some of the sedimentary basins.

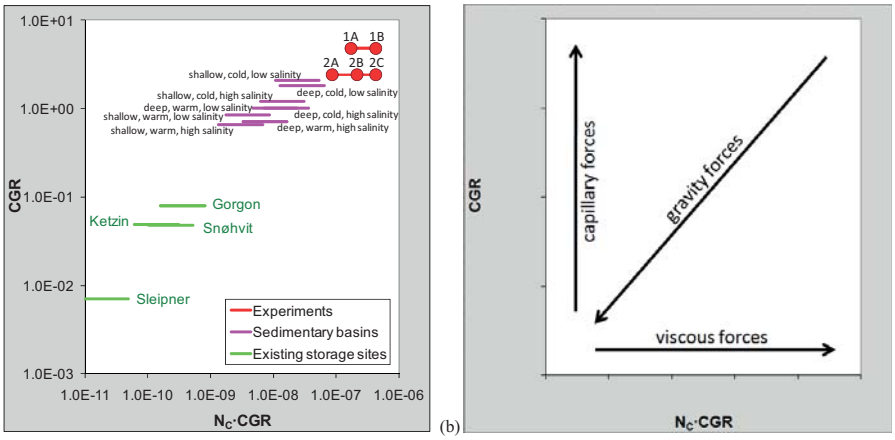

Figure 4 Representation of the experimental and field data by N_C and CGR (a) and forces that govern fluid flow in the reservoir (b).

5. Conclusions

The experiments described in this paper represent gravity and viscous unstable floods. In all displacements fractal-like fronts were observed. The flow paths were shorter in the high-permeability cases than in low-permeability cases. The gravity effects were more pronounced in cases with the low injection rate and high permeability. In such cases, the flood was forced to occur more in the vertical direction which resulted in less volume of the in-situ fluid displaced. When the injection rate increased (stronger viscous forces) more fingering and higher total displacement were obtained.

A plot of the brine displaced and the $CGR \cdot N_C$ for all experiments clearly shows that the volume of brine displaced decreases as the gravity forces are rising. This observation is consistent with the conclusion made by Kopp et al. [3].

Although at laboratory conditions fluids which were used resemble CO_2 and brine at possible reservoir conditions, the range of the existing storage sites was not reached in the scaling calculations. However, by lowering the IFT of the fluids, reducing injection rate, and increasing permeability it can be possible to scale the experiments to the conditions occurring in real storage sites.

Acknowledgements

The authors gratefully acknowledge SINTEF Petroleum Research and The School of Petroleum Engineering (UNSW) for making their facilities available to perform this research. The first and second authors also acknowledge the funding provided by the Australian Government through the CRC Program to support CO2CRC research.

This publication forms a part of the BIGCO2 project, performed under the strategic Norwegian research program CLIMIT. The authors acknowledge the partners: Statoil, GE Global Research, Statkraft, Aker Clean Carbon, Shell, TOTAL, ConocoPhillips, ALSTOM, the Research Council of Norway (178004/I30 and 176059/I30) and Gassnova (182070) for their support.

References

- [1] Taku Ide S, Jessen K, Orr Jr FM. Storage of CO_2 in saline aquifers: Effects of gravity, viscous, and capillary forces on amount and timing of trapping. International Journal of Greenhouse Gas Control 2007; 1:481-91.
- [2] Wood DJ, Lake LW, Johns RT, Nunez V. A Screening Model for CO_2 Flooding and Storage in Gulf Coast Reservoirs Based on Dimensionless Groups. SPE Reservoir Evaluation & Engineering 2008; Volume 11, Number 3:513-20.
- [3] Kopp A, Class H, Helmig R. Investigations on CO_2 storage capacity in saline aquifers: Part 1. Dimensional analysis of flow processes and reservoir characteristics. International Journal of Greenhouse Gas Control 2009; 3:263-76.
- [4] Cinar Y, Riaz A, Tchelepi HA. Experimental Study of CO_2 Injection Into Saline Formations. SPE Journal 2009; 14:588-94.
- [5] Nordbotten JM, Celia MA, Bachu S. Injection and Storage of CO_2 in Deep Saline Aquifers: Analytical Solution for CO_2 Plume Evolution During Injection. Transport in Porous Media 2005; 58:339-60.
- [6] Michael K, Allinson G, Golab A, Sharma S, Shulakova V. CO_2 storage in saline aquifers II-Experience from existing storage operations. Energy Procedia 2009; 1:1973-80.
- [7] Bennion DB, Bachu S. Dependence on Temperature, Pressure, and Salinity of the IFT and Relative Permeability Displacement Characteristics of CO_2 Injected in Deep Saline Aquifers. SPE Annual Technical Conference and Exhibition, San Antonio, Texas, USA 2006.
- [8] Dullien FAL. Porous media / fluid transport and pore structure. 2nd ed. San Diego: Academic Press; 1992.
- [9] Kaviany M. Principles of heat transfer in porous media. 2nd ed. New York: Springer; 1995.
- [10] Holt T, Vassenden F. Physical Gas/Water Segregation Model. In: Skjæveland SM, Skauge A, Hinderaker L, Sisk CD, editors. RUTH 1992-1995 - a Norwegian research program on improved oil recovery - program summary, Stavanger: Norwegian Petroleum Directorate; 1996, p. 446 s.
- [11] Bennion DB, Bachu S. The Impact of Interfacial Tension and Pore Size Distribution/Capillary Pressure Character on CO_2 Relative Permeability at Reservoir Conditions in CO_2-Brine Systems. SPE/DOE Symposium on Improved Oil Recovery, Tulsa, Oklahoma, USA 2006.

Paper III

Available online at www.sciencedirect.com

SciVerse ScienceDirect

Energy Procedia 37 (2013) 4863 – 4871

Energy Procedia

GHGT-11

Evaluation of CO_2 storage potential in Skagerrak

Per E. S. Bergmo[a,*], Szczepan Polak[a], Per Aagaard[b], Peter Frykman[c], Hans A. Haugen[d] and Dag Bjørnsen[d]

[a]*SINTEF Petroleum Research, S.P.Andersens v. 15b, N7465 Trondheim, Norway*
[b]*University of Oslo, Dept. of Geosciences, P.O.Box 1047 Blindern, 0316 Oslo, Norway*
[c]*Geological Survey of Denmark and Greenland, Øster Voldgade 10, DK-1350 Copenhagen, Denmark*
[d]*Tel-Tek, Kjølnes Ring 30, N-3918 Porsgrunn, Norway*

Abstract

Within the Skagerrak-Kattegat region up to 14 Mt of CO_2 can annually be captured from power and industry sources. To establish a CCS infrastructure in the region it is necessary to identify and characterize potential CO_2 storage sites. Initial screening of the region has revealed large aquifers in the Upper Triassic Gassum Formation. In dynamic simulation studies 250 Mt of CO_2 were injected into the Gassum Formation over a period of 25 years. Identification and analysis of parameters that affect CO_2 storage capacity were performed. Parameters important for the migration speed and the dissolution rate of CO_2 in open dipping aquifers were investigated by a series of simulations on generic tilted reservoir models.

Selection and/or peer-review under responsibility of GHGT

CO_2 storage; CO_2 storage capacity; Skagerrak; Gassum Formation; Hanstholm structure; open dipping traps;

1. Introduction

The Skagerrak-Kattegat area between Denmark, Sweden and Norway has no previous record of oil exploration or other activities which could have resulted in extensive mapping of the sub-surface. The data coverage is therefore scarce compared to regions in the North Sea and the density of data is decreasing as one moves eastward in Skagerrak. Initial screening of possible CO_2 storage sites in the region has been performed based on published work, new interpretations of seismic lines and interpretation of available well logs.

* Corresponding author. Tel.: +47-73591394; fax: +47-73591246.
E-mail address: per.bergmo@sintef.no.

1876-6102
Selection and/or peer-review under responsibility of GHGT
doi:10.1016/j.egypro.2013.06.396

The screening has revealed large open/semi-closed dipping aquifers in the Upper Triassic Gassum and Haldager Formations [1], which is evaluated for CO_2 storage. The present contribution presents reservoir simulations of CO_2 injection into the Gassum and Haldager Formations in the area north and north-east of the Fjerritslev Trough [2]. In addition a model of the Hanstholm structure offshore Denmark has been constructed on which initial simulations have been performed for estimating storage capacity. The reservoir simulations are part of an interdisciplinary project with the overall goal to establish a basis for large-scale handling of CO_2 in this area, including regional CO_2 sources and capture possibilities, transportation and infrastructure, possible storage sites as well as legal aspects related to the whole CCS chain [3].

The Gassum Formation is overlain by thick marine mudstones of the Fjerritslev Formation, which is characterized by large lateral continuity, forming a highly competent cap rock unit probably making the Gassum Formation one of the most promising reservoirs for CO_2 storage in the study area. The sandstone of the Haldager Formation consists of fluvial and shallow marine sandstones interbedded with thin mudstones. The thickness of Haldager Formation sandstone towards northwest under the Norwegian channel as taken from one well drilled in the Norwegian sector (IKU well 13/1-U-1) in the study area is 32 m and the net/gross ratio of 0.5. The average thickness of Haldager Formation sandstone in the offshore Danish wells is about 25 m, with an average porosity of more than 26 % and a net/gross ratio of 0.5 – 0.8. The Haldager Formation sandstone is overlain by the marine mudstones of the Børglum Formation. Regional distribution of the mudstones with good sealing capacity above makes also the Haldager Sand Formation a good potential reservoir for CO_2 storage in the area. Here we only present results from simulations of CO_2 injection into the Gassum formation and it is assumed that the Fjerritslev Formation is sealing.

2. Models

Three locations in the Skagerrak region have been investigated for CO_2 injection in this study. Two open dipping aquifer models in the Gassum Formation (Model1, Model2) with homogenous net thickness were made. In addition a model of the Hanstholm structure just south of Model1 has been constructed on which initial simulations were performed for estimating storage capacity.

Outline of the model areas for Model1, Model2 and Hanstholm on a top Gassum Fm. surface is shown in Figure 1. Location of Model1 and Model2 was decided based on the concept of storing CO_2 in an open dipping trap. The injection points should therefore be located down flank of a gentle dipping formation. The main short term mechanism for trapping CO_2 is assumed to be capillary trapping of CO_2 as residual phase. In addition, the long migration distance of the injected CO_2 will enhance the dissolution of CO_2 into the formation water. The Hanstholm structure is assumed to be a closed structure and was chosen for its size. The main short term trapping mechanism is assumed to be capillary trapping by the assumed sealing cap rock.

Reservoir properties are based on petrophysical logs from 12 Danish wells (including 6 offshore wells). No wells penetrate the model areas and average properties of the wells have been used. No thickness maps of formations were available when the reservoir models were built and a constant effective thickness was assumed. The model thicknesses are equal to the average net thickness in the well logs (not weighted) giving 50 and 20 meter thickness for Gassum and Haldager respectively. The basic assumption then is that the injected CO_2 will mainly migrate along and below the sealing cap rock at the top of the formations.

Average effective porosity from the well logs is 22.5 % but a linear correlation to depth was applied based on average porosity and depth points in the wells. The range of porosity in the two models is

between 21.3 % and 28.5 %. Permeability was correlated to porosity by a relationship developed by GEUS for this study based on their regional database. Permeability varies between 200 and 650 mD. Average net permeability from wells is 210 mD.

The open dipping trap models (Model1 and Model2) cover a large depth range and hence one can expect a relatively large variation in temperature and salinity of the formation water. A salinity gradient of 75.6 ppm NaCl per meter and a temperature gradient of 31 °C/m were assumed based on regional models and well data. In order to model the effect of this on density and viscosity of the formation water and solubility of the injected CO_2, 6 pVT regions (having constant temperature and salinity) were generated for Model1 and Model2.

Viscosity and density of the formation water was calculated for each region based on [4] and [5]. The solubility of CO_2 in brine is calculated from a correlation by Spycher et al. [6]. The density of CO_2 is based on an equation of state for CO_2 developed by Span and Wagner [7]. The viscosity of CO_2 was calculated from a correlation by Fenghour et al. [8].

Due to the relatively large grid block sizes linear relative permeability curves for brine and CO_2 phases were used. Residual CO_2 was set to 20 % and residual brine was set to 7 %. Measurement on cores from the Utsira Sand at the Sleipner CO_2 injection site (unconsolidated sand stone) indicates residual CO_2 saturation of 25% [9]. Assuming 20% might be on the low side (i.e. will underestimate trapped CO_2) but no measurements were available for the Gassum sandstone.

Initial hydrostatic conditions were assumed, with open/semi-closed boundaries up-dip towards north (Model1) and northwest (Model2). The open boundaries to the north were modeled by production wells producing at constant pressure giving amount of CO_2 migrating out of the model as produced CO_2.

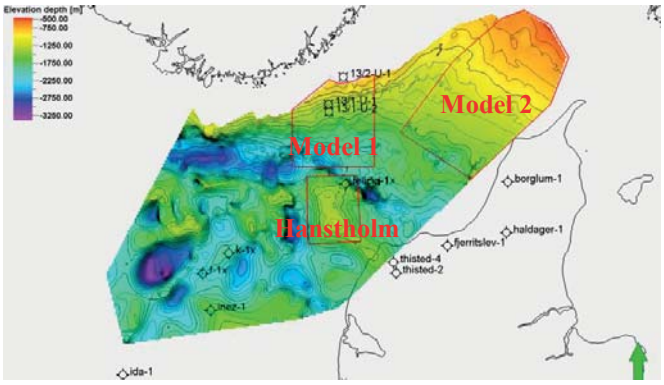

Figure 1. Outline of the model areas for Model1, Model2 and Hanstholm shown on a top Gassum Fm. surface.

3. Results, base case

In all three models, a total of 250 million tonnes of CO_2 is injected down-flank using three horizontal injection wells over a period of 25 years. Total simulated time is 4000 years.

3.1. Model1 and Model2

Injection took place by 3 horizontal injection wells perforated in the bottom layer with distance between injection wells 8 – 10 km. The wells have perforation intervals of 800-1000 meters. Injection depth was approximately 2410 m (Model1) and 1708 m (Model2). The well injection rate was 3.33 Mt/year = $4.88 \cdot 10^6$ Sm^3/day/well giving a total of 10 Mt/year.

The results of the simulations on the open dipping traps are shown in Figure 2 and Figure 3 as distribution of CO_2 saturation. For Model1, CO_2 reaches the northern border after 400 years, and after 4000 years 7.5 % has escaped. The rest is capillary trapped (~74.5%) or dissolved (~18%). Figure 2 shows CO_2 saturation in Model1 after 25 years (stop of injection), after 400 years when the first CO_2 has reached the open boundary to the North and after 4000 years. The open boundary is modeled with constant hydrostatic pressure.

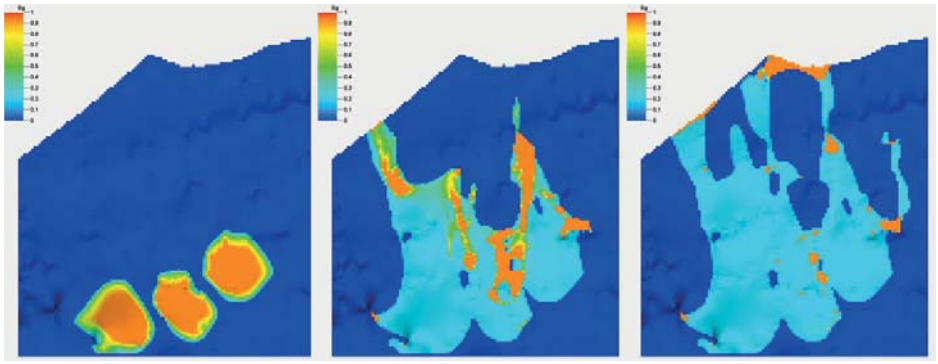

Figure 2. Plume development, shown as CO_2 saturation, for Model1 after 25, 400, and 4000 years after injection stop.

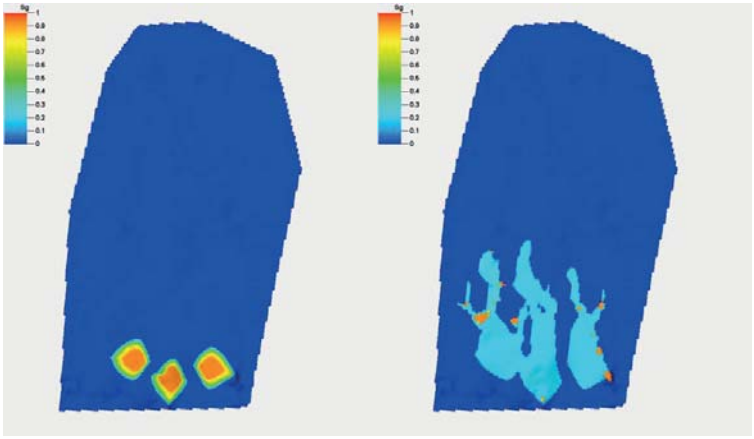

Figure 3. Plume development, shown as CO_2 saturation, for Model2 after 25 and 4000 years after injection stop.

For Model2, even after 4000 years, all the CO_2 stays within the model boundaries. A total of ~24% is dissolved after 4000 years, while the rest is capillary trapped (residual). Figure 3 shows distribution of injected CO_2 after 25 and 4000 years.

3.2. Hanstholm

The results of simulation of CO_2 injection in the Hanstholm structure is shown in Figure 4. Three horizontal injection wells were located down flank on the western and north-western side of the structure. The injected CO_2 migrates towards the top of the structure and 12.5% is dissolved into the formation water after 4000 years. Figure 4 shows CO_2 distribution after 25, 400 and 4000 years.

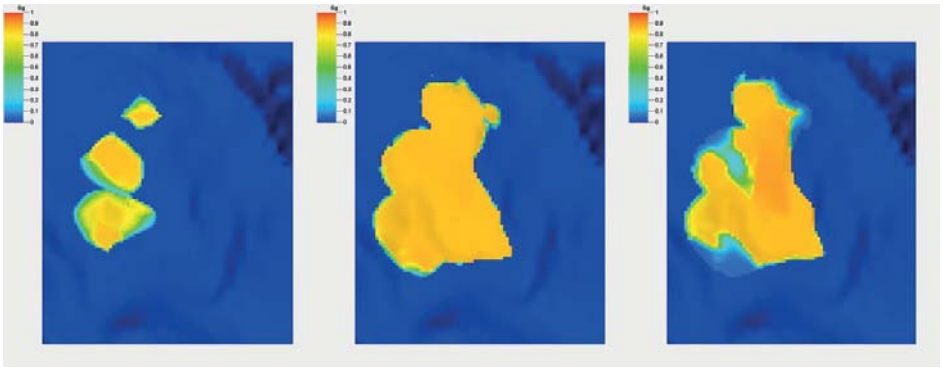

Figure 4. Distribution of injected CO_2 in the Hanstholm structure after 25, 400, and 4000 years (from left to right).

3.3. Evaluation of injectivity and storage potential

The injectivity is mainly a function of the permeability in the regions close to the injection wells. If the injectivity is low the bottom hole pressure (BHP) of the injection well will be high since a higher pressure is needed to push the injection phase at a given rate into the reservoir. Typical parameters affecting permeability for sand stone reservoirs are burial history and depth (diagenesis), shale content and porosity. A general observation is that the injectivity reduces with increasing depth and increasing shale content.

The increase in BHP for the three horizontal injection wells for Model1 and Model2 is around 90 bar in both cases. A safe pressure with respect to fracturing of the cap rock is assumed to be around 75 % of the lithostatic pressure but a detailed characterisation of the overburden is needed to estimate this. Estimating a safe pressure increase has not been performed at this stage but the difference between hydrostatic and lithostatic pressure increase with depth enabling a higher safe pressure increase with depth. A first estimate of safe pressure below the cap rock can be calculated by assuming an average density of the overlying formations. An estimate for Model1 and Model2 gives safe pressure increases of approximately 108 and 76 bars respectively if assumed sea depth is 100 meter and overburden density is 2000 kg/m^3. No maps of sea depth in the injection areas were available but increasing sea depth to 400 meter gives corresponding safe pressure increases of 86 and 54 bars.

If the pressure increase is too high several options exists to reduce it. Increase number of injection wells, produce formation water (will need production wells) and in the case of Model1 and Model2, inject

part of the CO_2 into the shallower Haldager formation. A simulation where 1/3 of the CO_2 is injected into the Haldager formation in Model2 has been set up and the results indicate that the injected CO_2 stays just inside the model area in Haldager after 4000 years and the maximum BHP increase in Haldager is approximately 65 bar and the BHP increase in Gassum is reduced from 90 to 80 bar.

The present simulations indicate that the open dipping traps in the Gassum formation can permanently store 250 Mt CO_2 by residual trapping. More detailed mapping of reservoir and overburden is required for better estimate of safe pressure, required number of injection (and production) wells and better estimates of CO_2 migration in the trap.

The bottom hole pressure increase in the Hanstholm structure when using 3 horizontal injection wells are approximately 140 bar. This is too high although the pressure increase below the cap rock (some distance away from the well perforations) will be lower. The option of increasing the number of injection wells and/or introduce water production wells down flank should therefore be considered. As for the other models a more detailed characterization of the cap rock and overburden is required to determine the safe pressure increase. The structure is however large enough to contain 250 Mt CO_2 assuming the cap rock is sealing.

4. Parameter sensitivities

In the open dipping traps of Model1 and Model2 the lateral migration speed of CO_2 is important for estimating capacity and safety of the storage site. A series of simulations on a synthetic tilted model were performed to investigate migration speed and dissolution rate as function of grid block resolution and capillary pressure. The synthetic model is 1500 by 10 000 meters and has a thickness of 50 m. The tilt of the model is 2° and the top of the model is at 1000 meter depth (shallow part). Porosity and horizontal permeability is 22.5 % and 210 mD respectively. Vertical to horizontal permeability ratio is 0.1 and the injection is down flank in one vertical well perforating the bottom layers. Injection rate was 100 000 tonnes of CO_2 per year for three years, total pore volume of the model is around $1.7 \cdot 10^6$ m^3. Grid resolution and capillary pressure were varied in the sensitivity simulations.

Capillary pressure will affect the migration speed and thickness of the CO_2 front. No capillary pressure measurements were available and capillary pressure measured on Utsira sand was used as basis for sensitivity simulations. The Utsira capillary entrance pressure (no gas saturation) equals to 0.01 bars. Simulations were performed with varying capillary pressure by multiplying the measured capillary pressure curve by factors 2, 4, 8, 16, and 32. It is assumed that the capillary pressure in Gassum will be higher than the capillary pressure in Utsira due to the reservoir's grain-size, sorting and assumed cementation (smaller pore throats).

The effect of increasing the capillary pressure on CO_2 distribution is shown in Figure 5a for the model with a grid block size of 100 by 100 meters and layer thickness below the top equal to 0.5 meter. It can be seen that an increase in the capillary entry pressure will reduce the total migration distance of the injected CO_2. This is because the migrating CO_2 has to overcome the capillary entry pressure before it can flow into a neighbouring grid block. Thickness of the migrating CO_2 front will thus be larger if the grid layering is fine enough to capture this. Capillary effects are a pore scale phenomenon and since large scale models have to be coarsely gridded the effect of the capillary pressure is scaled into the grid block size and the critical gas saturation (i.e. the minimum gas saturation necessary for the gas to be mobile). No simulation tests have been performed on how the distribution of CO_2 will depend on critical and residual gas saturation.

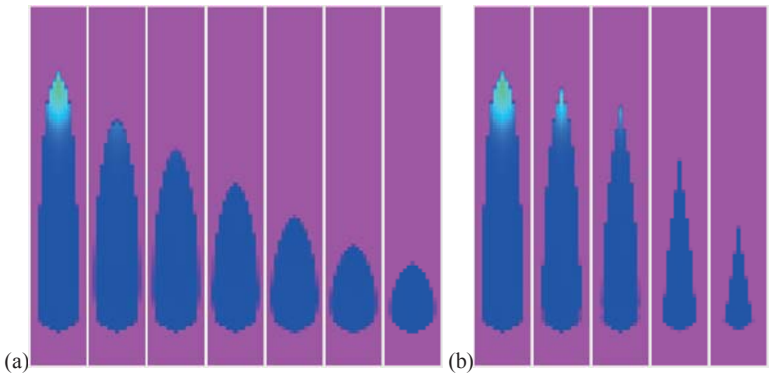

Figure 5. (a) Effect of capillary pressure on migration distance. Capillary entrance pressure in the different simulations was (from left to right): 0 (no capillary pressure), 0.01, 0.02, 0.04, 0.08, 0.16 and 0.32 bar. Plots show CO_2 distribution after migration has stopped (capillary trapped as residual CO_2); (b) Effect of layer thickness below the top, from left; 0.5 m, 0.75 m, 1 m, 2 m, 5 m layer thickness. Areal grid block size is 100 by 100 m simulated with no capillary pressure.

The injected CO_2 will due to buoyancy forces migrate along the top of the model. The thickness of the migrating front will in the simulations depend on grid layer thickness and critical gas saturation. These should be balanced to represent the effect of capillary pressure. However, both of these parameters are unknown. Figure 5b displays the effect of refining the layers below the top of the model from 5 to 0.5 meter layer thickness. Increasing the layer thickness will reduce the plume length. This is due to increased thickness of the front (one layer in the grid) and because the increased size of the grid blocks will require a larger volume of CO_2 in each grid block to overcome the critical gas saturation. This will slow down the speed of the migrating front. No sensitivity on the gas distribution by refining the areal grid block size has been investigated. Having smaller grid blocks will reduce the gas volume required to overcome the critical gas saturation but this effect will be minor if the coarsest grid resolution is sufficient to resolve the shape of the migrating CO_2.

Dissolution of CO_2 into the formation water is a function of the contact area between the CO_2 phase and under-saturated formation water. In practice this will depend on how large volume CO_2 has swept because almost all the dissolved CO_2 is present in the residual non-mobile water. An increase in migration distance will result in an increase in dissolved CO_2.

Simulations with refined layer thickness below the top were performed for Model2. Base case simulations which had 5 meter layer thickness would correspond to a very high capillary entry pressure. Results of refining the layers at the top to 1 and 2 meters are shown in Figure 6. The migration distance for the refined models is increased but the injected CO_2 is still within the boundaries of the model. Similar increase in migration distance should be expected for Model1 with the consequence that more CO_2 migrates out of the boundaries of the model.

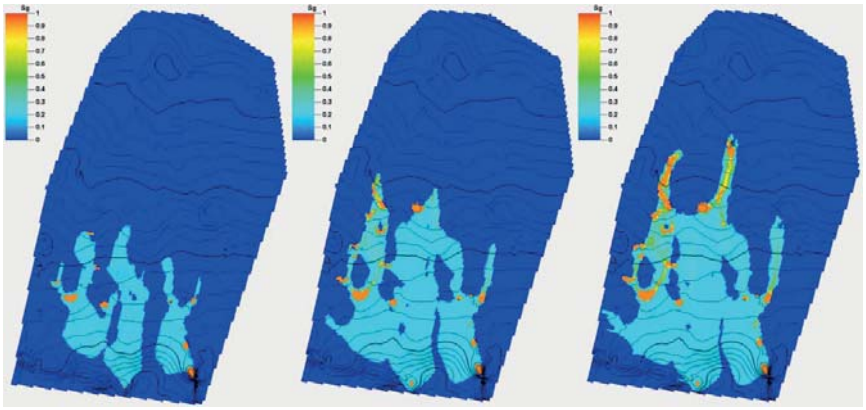

Figure 6. Distribution of injected CO_2 after 4000 years for the base case model with uniform layer thickness of 5 m in the whole model (left) and for refined layer thickness below the top equal to 2 m (middle) and 1 m (right).

5. Conclusions

Simulations indicate that the Late Triassic Gassum Formation has the capacity for storing at least the 250 million tonnes of CO_2 from the mapped industrial sources in the Skagerrak-Kattegat area but it must be emphasized that there are large uncertainties in the constructed models due to scarcity of data. The most critical factors for safe storage are the fracturation pressure of the sealing cap rock and the parameters controlling lateral migration of the injected CO_2. The induced pressure increase in the Hanstholm model is higher than the estimated safe pressure increase for the cap rock integrity but the formation may still be suitable for storage by increasing the number of injection and water production wells. Further characterization of the cap rock and overburden is required to give a better estimate of fracturation pressure in all three target areas. Sea bottom depth may be a limiting factor for the open dipping traps since a thinner overburden will reduce the fracturation pressure of the cap rock.

The main results indicate that the north-eastern part of the Gassum formation on the Danish side is the most promising target for injection of 250 Mt of CO_2. This is based on the observation that all the injected CO_2 is capillary trapped or dissolved within the model boundaries, the injection pressure is thought to be in the safe pressure range and the option of injecting part of the CO_2 into the shallower Haldager formation is available. This option is also possible for the model on the Norwegian side but simulations indicate that the injected CO_2 can migrate to the northern boundary of the formation where further migration is uncertain. The location is still worth investigating further since small changes in flow parameters can change the maximum plume size of the injected CO_2. These parameters are at the present uncertain and more data is needed for better characterization of the target formation.

The Hanstholm structure has a domal closure that can hold the injected amount of CO_2 but simulation results from the current model indicate injectivity problems with the applied high injection rates. Introducing a larger number of injection wells and/or production wells could change this and if it is possible to build confidence in the sealing properties of the cap rock, Hanstholm could be the preferred target. Further characterization of the target formations and the overburden could also change the ranking of the models (cap rock integrity and safe pressure increase).

Acknowledgements

The work presented in this paper received financial support from industry and Gassnova under the Climit programme (Project number 194492). The publication has been produced with support from the NORDICCS Centre, performed under the Top-level Research Initiative CO_2 Capture and Storage program, and Nordic Innovation. The authors acknowledge the following partners for their contributions: Statoil, Gassco, Norcem, Reykjavik Energy, and the Top-level Research Initiative (Project number 11029).

References

[1] Fawad M, Sassier C, Jarsve EM, Aagaard P, Faleide JI, Nielsen LH, Kristensen L, Bergmo PES. A Potential CO_2 Storage Play in Skagerrak – Depositional Environment and Reservoir Geology of the Gassum Formation. Poster presentation at *TCCS-6*, Trondheim 2011.

[2] Bergmo PES, Pham Van TH, Nielsen LH, Kristensen L, Fawad M, Faleide JI, Aagaard P. A Potential CO_2 Storage Play in Skagerrak – Injection Strategy and Capacity of the Gassum Formation. Poster presentation at *TCCS-6*, Trondheim 2011.

[3] Haugen HA *et al.* CCS in the Skagerrak/Kattegat area. *Energy Procedia* 4, 2324-2331; 2011.

[4] Spivey JP, McCain WD Jr, North R. Estimating Density, Formation Volume Factor, Compressibility, Methane Solubility, and Viscosity for Oilfield Brines at Temperatures from 0 to 275°C, Pressures to 200 MPa, and Salinities to 5.7 mole/kg. *JCPT* (July 2004). [PETSOC 04-07-05]

[5] Kestin J, Khalifa HE, Abe Y, Grimes CE, Sookiazian H, Wakeham WA. Effect of pressure on the viscosity of aqueous sodium chloride solutions in the temperature range 20-150°C. J. Chem. Eng. Data, 23, 328–336; 1978.

[6] Spycher N, Pruess K, Ennis-King J. CO_2-H_2O Mixtures in the Geological Sequestration of CO_2. II. Partitioning in Chloride Brines at 12−100°C and up to 600 bar. *Geochimica et Cosmochimica Acta*, Vol. 69, No. 13, pp. 3309–3320; 2005.

[7] Span R, Wagner W. A new equation of state for carbon dioxide covering the fluid region from the triple-point temperature to 1100 K at pressures up to 800 MPa. *J. Phys. Chem. Ref. Data*, Vol. 25, No. 6, 1509-1596; 1996.

[8] Fenghour A, Wakeham WA, Vesovic V. Viscosity of Carbon dioxide. *J. Phys. Chem. Ref. Data*, Vol. 27, No. 1; 1998.

[9] Akervoll I, Lindeberg E, Lackner A. Feasibility of reproduction of stored CO_2 from the Utsira formation at the Sleipner gas field. Proceedings of the 9th International Conference on Greenhouse Gas Control Technologies, Washington, USA; 2008.

Paper IV

Submitted to Journal of Transport in Porous Media on 22.03.2014

Names of the authors:
Szczepan Polak, Yildiray Cinar, Torleif Holt, Ole Torsæter

Title:
Use of Low- and High-IFT Fluid Systems in Experimental and Numerical Modelling of CO_2 Storage in Deep Saline Formations

Affiliations:
Szczepan Polak, Ole Torsæter
Norwegian University of Science and Technology NTNU, 7491 Trondheim, Norway

Yildiray Cinar
Cooperative Research Centre for Greenhouse Gas Technologies CO2CRC, GPO Box 463, Canberra, ACT 2601, Australia

Torleif Holt
SINTEF Petroleum AS, Postboks 4763 Sluppen, 7465 Trondheim, Norway

Corresponding author:
Szczepan Polak, e-mail address: szczepan.polak@zoho.com, telephone number: (0047) 95 205 446

Abstract
Storage of CO_2 in deep saline formations is currently the most promising option for mitigating the impact of climatic changes. Therefore, it is important to understand flow processes and distribution of forces acting underground on injected CO_2. To demonstrate the influence of gravitational, viscous, and capillary forces on the flow of CO_2, special experiments were designed. Laboratory experiments and numerical simulations were performed, where fluid representing CO_2 was injected into a 2D porous medium saturated with fluid representing brine. Two sets of fluids characterized by different interfacial tension (IFT) were tested. Results demonstrate that at increasing injection rate viscous forces become stronger, what leads to a higher total displacement of brine. Such performance is preferred at field scale, since it facilitates dissolution and residual trapping of CO_2. Gravity effects were more pronounced in cases with low injection rates and high permeability and are demonstrated by lower volumes of the in-situ fluid displacement. Therefore,

reservoirs giving low influence of gravity forces are more suitable for CO_2 storage. The high-IFT fluid system had an IFT corresponding to the value of CO_2-brine systems at possible reservoir conditions. However, the fluid flow in the laboratory model was dominated by capillary forces, which is less likely to be observed at field scale. The low-IFT fluid system resembled better field scale flow behaviour. The laboratory experiments were also modelled using numerical reservoir simulation software. While modelling of observations from high-IFT system was challenging, simulations for low-IFT displacements showed accurate reflection of experiments.

Keywords
CO_2 storage, glass-bead models, laboratory experiments, dimensionless numbers, numerical modelling

1 Introduction

Since the late 19th century, the Earth's surface temperature has increased and the evidence on climate change has grown substantially (Stocker et al. 2013). The main cause of the climate change is attributed to deforestation and increase in anthropogenic emissions of CO_2 and other greenhouse gases in the atmosphere originating from fossil fuel combustion. Since the start of the industrial revolution in the mid-18th century mankind has produced approximately 337 billion metric tonnes of CO_2 and half of this amount was emitted since mid-1970s (Boden et al. 2010). Currently CO_2 emissions from fossil fuels are approximately 8.4 billion metric tonnes (Gtonnes) per year (Boden et al. 2010). As the emission of CO_2 is predicted to increase in the future (IPCC 2007) it is important to find an efficient method of limiting its release to the atmosphere.

Storage of CO_2 in deep geological formations is one of the measures for mitigating the impact of climatic changes (IPCC 2005). Currently the most promising option for the geological CO_2 storage are thought to be deep saline formations, due to their large, immediately available capacity (IPCC 2005). Saline formations are sedimentary rock formations saturated with brine which is not suitable neither for human consumption nor for agriculture (e.g. IPCC 2005). Global storage capacity in saline aquifers was estimated to be in a range of 1000-10000 Gtonnes (IPCC 2005; IEA-GHG 2008). This could mean that all CO_2 produced in this century (assuming current yearly levels) could be stored underground if the capacity of the saline aquifers would be efficiently used and storage sites would prove to be safe.

Every potential geological storage site considered for use in carbon capture and storage (CCS) must be carefully investigated and the flow processes taking place within such reservoirs must be understood. The characteristics of flows that occur

when CO_2 is injected into a deep geological formation control how much CO_2 can be effectively injected and stored within the formation. Understanding of processes that take place within a saline formation during and after CO_2 injection is essential in order to select a suitable storage site. Flow regimes that occur when CO_2 is injected into a geological formation control how much CO_2 can be stored in the formation. Therefore, selection of a geological storage site for CO_2 must be preceded by an accurate understanding of the flow processes that take place within the reservoir during and after injection.

In recent years numerous analytical and numerical studies have been undertaken that concern site characterization for CO_2 injection/storage and describe the simultaneous flow of CO_2 and brine in subsurface formations (e.g. Nordbotten et al. 2005; Taku Ide et al. 2007; Wood et al. 2008; Kopp et al. 2009). However, little experimental data have been reported that shed light on the nature of the drainage process which applies to CO_2 injection. Fluid flow in parameter range appropriate for CO_2 storage in saline aquifers has been studied in both 2D (Hele-Shaw-like) and cylindrical models filled with glass-beads (e.g. Cinar et al. 2009; Islam et al. 2013). Systems with high interfacial tension (IFT) fluids at ambient conditions were commonly used in order to model flow patterns under CO_2 injection. Such experimental set-up provides information on the behaviour of fluid displacement in addition to the data which can be used in the numerical simulations. Furthermore, experimental procedures can be successfully employed in order to verify results of analytical and numerical studies. The main advantage of these experiments is the possibility to visually assess the behaviour of the fluids in the model.

CO_2 and brine are immiscible at reservoir conditions and they form a high-IFT fluid system where CO_2-brine IFT falls between 20 and 56 mN/m (Bennion and Bachu 2006; Chiquet et al. 2007). Therefore, the high-IFT system is usually a first choice when one tries to mimic CO_2 and brine interaction. Past work on fluid flow in high-IFT systems often demonstrated by the means of Hele-Shaw cell (e.g. Saffman and Taylor 1958; Homsy 1987; Løvoll et al. 2005; Duan and Wojtanowicz 2007) indicates that the most visible feature is the pronounced fingering of injected fluid which dominates the flow. At lower IFT, however, it is possible to observe a more stable and uniform displacement front in addition to finer, viscous fingering. Further, as it was demonstrated previously (Cinar et al. 2006; Asghari and Torabi 2008; Islam et al. 2013), it is problematic to simulate accurately laboratory-scale high-IFT experiments in commercial fluid flow simulators. Nevertheless, in this work, we present an approach for simulating a high-IFT system that resembles effects observed in the experiments. In addition to the high-IFT system, a low-IFT system was investigated in order to observe finer details of fluid flow behaviour on a smaller scale. Furthermore, it has been demonstrated that the low-IFT system is more suitable for simulations at the laboratory scale.

Additionally, the paper presents findings obtained during experimental examination of the flow processes that normally take place within a saline formation during CO_2 injection. In the procedures, CO_2 is represented by a model fluid injected into a model system of saline aquifer. Influence of low- and high-IFT fluid systems on the flow patterns is demonstrated as well as results of the numerical simulations from modelling of the laboratory experiments.

2 Material and methods

Quasi two-dimensional experiments were performed in a synthetic porous medium initially filled with a water-rich phase. The model was made of two vertical glass plates with space between them packed with glass-beads. Models used in the experiments represented homogeneous porous media where the glass-bead size controlled their permeability. Two sets of fluids with different IFT were used in the experiments.

In the field applications, CO_2 is normally injected at the bottom of the geological formation. Even in a supercritical state, it is less dense than in-situ brine, and it will always migrate up towards the top of formation. In such a case, gravity forces will cause instabilities in the displacement front. Additionally, high viscosity difference between fluids at the reservoir conditions points on instability caused by viscosity difference. Therefore gravity and viscous unstable floods were most suitable to experimentally model CO_2 injection into brine filled formations. Experiments were designed in a way that demonstrates the influence of gravitational, viscous and capillary forces on the vertical flow of CO_2. Further, experiments were modelled by means of ECLIPSE 100, a commercial numerical reservoir simulation software.

2.1 Experimental setup

The model consisted of two glass plates of 40x40x1.45 cm each. Between the glass plates a polypropylene frame was placed. Along the inner side of the frame an O-ring seal was attached (Ø=0.262 cm). Thickness of the frame was 0.20 cm and the outer dimensions were equal to the glass plates. The frame was additionally covered with elastic silicone in order to increase the tightness of the model. This added to the overall thickness of the frame and when the model was assembled, the dimensions of the porous part of the model were 30x30 cm with a thickness of 0.260 cm. The 'back' plate of the model had 8 holes with connectors and tubing installed. The distance from the inlet, located at lower centre, to the top of the model was 28 cm. The plates and the frame were clamped together with screws. The assembled model was placed on a vibrating table and the glass-beads were

poured in through one of the connector's opening until model was completely filled.

Once the model was filled with glass-beads it was placed vertically in a holder. The experimental setup consisted of the following elements: tubing and set of valves and connectors to direct the flow of the fluids to and from the model; two piston pumps used for injecting the fluids into the model (one pump for each fluid); two digital balances used for measuring mass of the injected and produced fluids; a digital differential pressure transducer for measuring the pressure difference between inlet and outlet of the 2D cell; a digital camera for taking pictures of changes in fluids saturation in the model during experiments; a PC with a logging program; a cylinder with pressurised CO_2 used for flushing the model before saturating it with the water-rich phase and for drying the model after cleaning. A schematic of the experimental setup is shown in Fig. 1.

Data acquisition was made by a logging program run on the PC to which the digital balances and the differential pressure transducer were connected. The logging program was developed using the graphical programming tool LabVIEW (National Instruments). The software collected readings from instruments at given time intervals. After the experiments were performed the log files were transformed, analysed, and used for calculations in MATLAB and Excel. The camera was also controlled by the PC and pictures were taken at given time intervals.

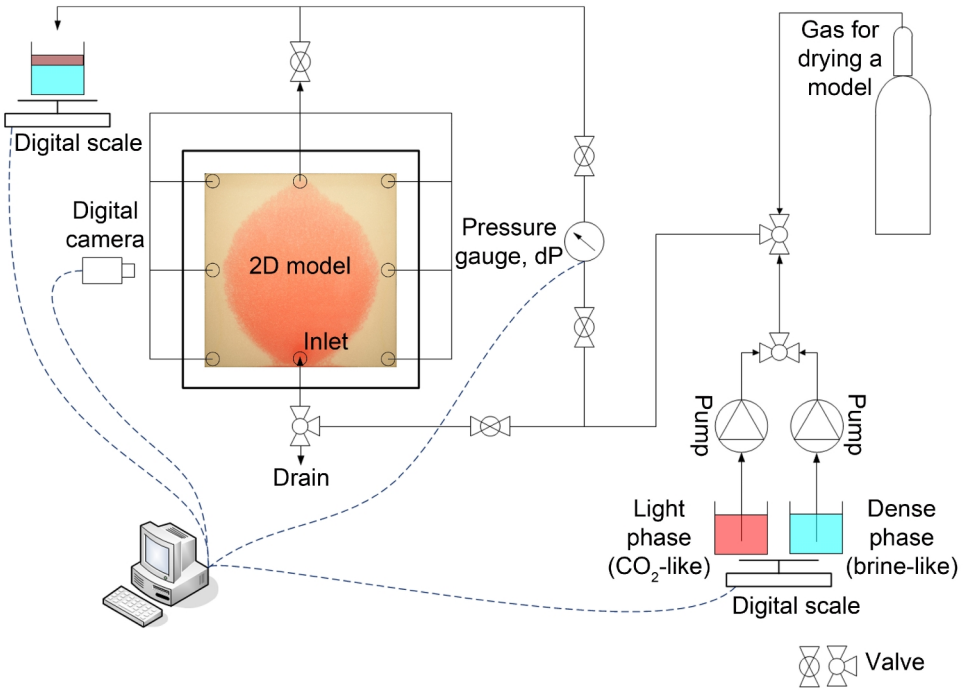

Fig. 1 Schematic of the experimental setup. Note that inlet and outlets of the model are placed on the 'back' side

2.2 Properties of the porous medium

The model's porous medium consisted of regular soda-lime glass-beads. Both mono-dispersed and range sizes were used in experiments, i.e.: 200, 180-250, 300-400, and 400 micron.

Porosity of the model was estimated in each experiment by measuring the volume of the injected dense fluid until the model was fully saturated. Porosity and thus pore volume measurements were carried out each time the model was re-packed and re-saturated. On average the measured porosity was equal to 0.39.

The glass-bead size controlled the permeability (k) of the model. The theoretical values of permeability for each glass-bead size range used in experiments were calculated with both the Rumpf and Gupte (R-G) equation (Rumpf and Gupte 1975) (Eq.1) and Kozeny-Carman equation (K-C) (Eq.2) (Kaviany 1995):

$$k = \frac{\phi^{5.5}}{5.6} d_b^2 , \qquad (1)$$

$$k = \frac{\phi^3}{180(1-\phi)^2} d_b^2 , \qquad (2)$$

where: k - permeability, m^2; ϕ - porosity; d_b - glass-bead diameter, m.

In order to verify calculated values, the permeabilities were also measured experimentally in a 1D model (tube filled with glass-beads) and calculated according to Darcy's flow equation (Eq.3):

$$k = \frac{q\mu L}{A\Delta p} , \qquad (3)$$

where: k - permeability, m^2; q - flow rate, m^3/s; μ - fluid viscosity, Pa·s; L – glass bead pack length, m; A - pack's cross section surface area, m^2; Δp - pressure drop measured along the pack, Pa.

Although the R-G equation is said to offer better fit with experimental data than the K-C model, all calculations presented here are based on permeability values calculated according to the K-C equation. The reason for choosing K-C values is that they fall in between measurements from 1D model (minimum) and R-G calculated values (maximum). Permeabilities measured in the 1D laboratory tests are considered too low for the conditions present in the 2D model. The 1D glass-bead pack used for measuring permeabilities was much thicker than the bead layer in the 2D model and thus the 'wall-effect' influence on fluid flow was significantly lower. Also, the glass-beads, whose size is given as a range, had a certain size distribution and thus, smaller beads filled the spaces between the larger ones reducing in this way the permeability. There were no permeability measurements in 1D pack performed on mono-dispersed glass-beads due to insufficient quantities

available. Values of the K-C calculated permeabilities are shown in Table 1. Note that permeability values are given in Darcy unit (D), where 1 D = $1 \cdot 10^{-12}$ m^2.

Table 1 Sets of experimental cases with parameters used in calculations

Case	Case description	IFT, mN/m	Glass bead diameter, d_b, micron	Permeability, K-C equation, k, D	Porosity, ø	Injection rate, q, cm^3/min
1A	high-IFT, low-k, low-q	34	200	34.5	0.390	0.10
1B	high-IFT, low-k, mid-q	34	200	34.5	0.390	0.25
1C*	high-IFT, low-k, high-q	34	200	34.5	0.390	0.50
2A	high-IFT, high-k, low-q	34	400	141.7	0.390	0.10
2B	high-IFT, high-k, mid-q	34	400	141.7	0.390	0.25
2C	high-IFT, high-k, high-q	34	400	141.7	0.390	0.50
3A	low-IFT, low-k, low-q	1	180-250	40.9	0.394	0.10
3B	low-IFT, low-k, mid-q	1	180-250	40.9	0.394	0.25
3C	low-IFT, low-k, high-q	1	180-250	40.9	0.394	0.50
4A	low-IFT, high-k, low-q	1	300-400	108.5	0.388	0.10
4B	low-IFT, high-k, mid-q	1	300-400	108.5	0.388	0.25
4C	low-IFT, high-k, high-q	1	300-400	108.5	0.388	0.50

*) simulation only

2.3 Fluid systems

Two sets of the experimental fluids were prepared. One set was a mixture of distilled water, glycerol, and n-heptane (Cinar et al. 2009), and another set was a mixture of 2% solution of $CaCl_2$ (brine), iso-propanol, and iso-octane (Schechter et al. 1991; Holt and Vassenden 1996). Both mixtures separate into two phases at ambient conditions: (1) the water-rich, dense and more viscous phase which represents formation brine in the experiments, and (2) the hydrocarbon-rich, lighter and less viscous phase which represents CO_2. The hydrocarbon-rich phase was dyed in red with Sudan IV dye. The water-rich phase had no dye added.

The first pair of fluids characterises high density difference (476 kg/m^3) and high IFT value (34 mN/m) and is called the high-IFT system. The reason for choosing this pair of fluids was their properties which were analogous to the properties of the CO_2 and brine at possible reservoir conditions. The analogy was made based on the comparison of the density difference, viscosity ratios, and IFT values which all

were within a range of values reported for CO_2 and brine at in-situ conditions (Nordbotten et al. 2005; Bennion and Bachu 2006; Chiquet et al. 2007; Michael et al. 2009). Experiments performed on high-IFT system and analysis of the balance between forces acting on the flow were described in Polak et al. (2011). Here they are included as a part of a more comprehensive study.

The second pair of fluids has lower density difference (206 kg/m^3) and low IFT (1 mN/m) and is called the low-IFT system. The advantage of using this pair of fluids was reduced values of the capillary pressure and thus lower entry pressure for the injected fluid. Also lower value of the IFT was expect to be expressed by domination of viscous forces which typically govern the flow in the field scale (Berg and Ott 2012).

Detailed composition and properties of fluid systems used in experiments are presented in Table 2. Fluids' density was measured with an Anton Paar DMA46 densimeter, viscosity with an Ubbelohde viscometer, and IFT with a Du Noüy type ring tensiometer.

Table 2 Composition and properties of fluids used in experiments

System	Composition	Phases	Density, kg/m^3	Density difference, kg/m^3	Viscosity, mPa·s	Viscosity ratio	IFT, mN/m
High IFT	distilled water (23 wt%) glycerol (44 wt%) n-heptane (33 wt%)	glycerol-rich phase (BRINE)	1160	475	12.56	30.8	34.0
		n-heptane-rich phase (CO_2)	685		0.41		
Low IFT	2% $CaCl_2$ brine (29.1 wt%) isopropanol (34.3 wt%) isooctane (36.6 wt%)	water-rich phase (BRINE)	903	205	3.56	6.4	1.0
		isooctane-rich phase (CO_2)	698		0.56		

2.4 Experiments

Prior to saturating the model with the water-rich phase, it was flushed with CO_2. The reason for using CO_2 was that the IFT between CO_2 and injected water-rich phase is lower than between air and water-rich phase, thus the injected fluid displaced gas more efficiently from the pores and avoided leaving any gas pockets behind. Also, any CO_2 trapped in pores was eventually dissolved in brine. Both the water-rich phase and non-wetting phase were injected from the bottom-middle hole (inlet) of the model (Fig. 1). All remaining holes (outlets) were connected to the

common tubing and kept open during saturating the model with the water-rich phase. After each experiment, the model was washed with isopropanol, drained, dried and saturated again with the water-rich phase before a new experiment.

The glass-bead model was initially saturated with the denser water-rich phase that represents formation brine. The red-dyed, lower density fluid, representing CO_2 was then injected using a piston pump from the bottom of the model. The lighter phase was injected at a constant rate in every experiment until it reached the top of the model. In some cases injection time was extended in order to see how displacement patterns could change during longer injection periods. Injection time corresponded to the fraction of the model's pore volume (PV) injected and varied between 0.25 and 1.00 PV. All experiments were performed at ambient conditions. For a given fluid system only permeability (k) and injection rate (q) were varied and all other parameters were kept constant. The flow velocities (Darcy's velocity 'u') observed in experiments were within a range of 0.26-1.29 m/day which corresponds to the flow velocities expected during CO_2 storage processes in real reservoirs (Berg and Ott 2012). In order to create conditions analogous to an open reservoir, the outlets located at the edges of the model were open during the experiments and thus injected fluid could displace the brine in all directions which were available in the 2D-model. During the experiments, the injection pressure, the mass of the injected and produced fluids, the time when injected fluid reached the top of the model, and the time when injected fluid left the model were recorded.

Table 1 gives different combinations of permeability and injection rates which were investigated, and the parameters used in calculations. There were in total 11 different cases investigated in the laboratory and each case was done between two to four times depending on the results repeatability. If the results from two similar experiments were consistent, no more experiments with that parameter combination was done. In this article averaged results of each case are presented. Observations from the laboratory experiments are documented in Fig. 3 through Fig. 6. Note that the high-IFT, low-k, high-q scenario was not done due to the high injection pressure which could have caused the model to burst.

In order to assess forces acting on the flow of fluids in the experiments, scaling parameters were used: capillary number (N_C) and capillary-to-gravity-ratio (R_{CG}). Both these dimensionless numbers incorporate properties of fluid and porous medium. For a given experimental fluid system, only permeability and flow velocity controlled the dimensionless parameters. The capillary number, N_C, is defined as a ratio of viscous to capillary forces (Eq.4):

$$N_C = \frac{u \cdot \mu_i}{\gamma}, \qquad (4)$$

where: u - Darcy's flow velocity, m/s, defined as u=q/A, with q being injection rate, m^3/s, and A being the cross-sectional area of the model, m^2; μ_i - viscosity of the injected fluid, Pa·s; γ - interfacial tension (IFT), N/m.
The capillary to gravity force ratio, R_{CG}, (Holt and Vassenden 1996) is defined as (Eq.5):

$$R_{CG} = \frac{2\gamma}{\Delta\rho \cdot g \cdot h \cdot \sqrt{\frac{k}{\phi}}}, \qquad (5)$$

where: $\Delta\rho$ - density difference of the fluids, kg/m^3; g - acceleration of gravity, m/s^2; h - distance between model's inlet and outlet or formation thickness in the reservoir, m.
Since the N_C is a ratio of viscous to capillary forces and R_{CG} is a ratio of capillary to gravity forces, thus $R_{CG} \cdot N_C$ is a ratio of viscous to gravity forces (R_{VG}). The R_{VG} parameter was established because together with N_C clearly presents the direction of forces acting on the flow of the fluids in the experimental model. These forces and location of the experiments in the N_C-R_{VG} space are presented in Fig. 2. Values of the calculated dimensionless parameters are summarised in Table 3.
The observation from Fig. 2 is that viscous forces are correlated with injection rates. When the injection rate increases the influence of viscous forces also increases. It is also clearly seen that at high IFT capillary forces are stronger than at low IFT. The influence of the gravity forces is increasing with decreasing injection rate as well as increasing permeability.
This means that the effect of the gravity forces will be larger at the lower injection rates and especially at high-k cases. This agrees with observations made, among others, by Alhamdan et al. (2012).

Table 3 Calculated dimensionless parameters

Case	$N_C \cdot 10^{-3}$	$R_{VG} \cdot 10^{-3}$
1A	0.0642	0.3316
1B	0.1605	0.8291
1C*	0.3210	1.6581
2A	0.0642	0.1658
2B	0.1605	0.4144
2C	0.3210	0.8288
3A	1.4794	0.5142
3B	3.6985	1.2856
3C	7.3970	2.5711
4A	1.4794	0.3133
4B	3.6985	0.7833
4C	7.3970	1.5665
*) simulation only		

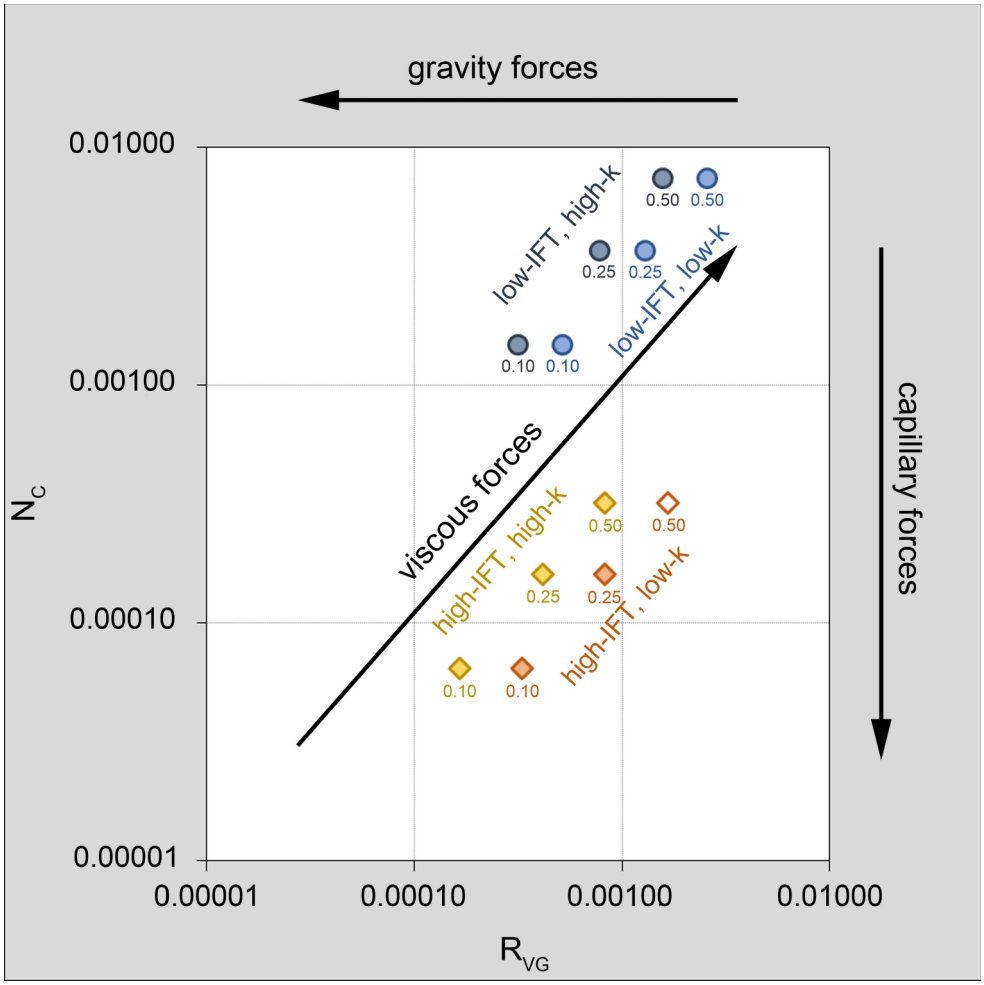

Fig. 2 Experiments in N_C-R_{VG} space; distribution of the forces acting on the fluid flow in experiments; each case is marked with the injection rate value (cm^3/min); empty marker in high-IFT, low-k cases indicates an experiment which was not performed but for which simulation was made

3 Simulations

Numerical simulations were performed in ECLIPSE 100 software. The dimensions of the simulation model were exactly the same as of the physical one. Grid resolution was 121 x 1 x 121, and thus grid-block size was 0.248 x 0.260 x 0.248 cm. The total number of grid-blocks was 14 641. The porosity, permeability, and fluid properties were the same as in the respective laboratory experiments (Table 1). In order to introduce heterogeneity related to sorting of the beads, the permeability did not have a constant value. Permeability of the model had a normal distribution, with mean equal to the calculated permeability and standard deviation equal to 10% of the mean value.

During the numerical simulations it proved to be difficult to model the experiments with the high-IFT system, which were dominated by capillary forces (Fig. 2). The simulations were improved by modifying the simulation grid. The modified grid had 2% of grid-blocks with randomly given zero-transmissibilitiy to each flow direction: from lower to upper grid-block, upper to lower, left to right and right to left. This gave in total approximately 8% of affected grid-block to grid-block transmissibilities in the model (it could happen that one grid-block has modified transmissibility in more than one direction). The advantage of this solution, over e.g. modifying permeability or deliberately setting up high permeable channels, is that it does not affect flow properties of the model, and instead, it creates micro-barriers, which injected fluid must pass around in order to flow to the top of the model, and possibly creates channels. The fluid injected into the porous medium choses to flow in the highest permeable paths. Since the ECLIPSE 100 cannot simulate at the pore level, each grid-block represents averaged properties of the porous media. Removing transmissibilities between some of the grid-block might seem artificial, but it is necessary in order to represent those parts of porous media where glass-beads are better sorted and thus less permeable. In combination with a high viscosity difference between non-miscible fluids (high IFT), and a considerable density difference, this created flow channels. Introduction of micro-barriers through reduced transmissibilities for the high-IFT system was thus an approach that took these conditions into account. With the low-IFT system, the displacements were more uniform and flow channels were not visible. It was therefore not necessary to use the same kind of grid modification as in the high-IFT cases. The numerical simulations reproduced the experiments well.

In the simulations, a denser fluid was modelled as water (wetting phase) and lighter as gas (non-wetting phase). The relative permeability curves were calculated according to the Brooks and Corey's correlation (Corey 1954; Brooks and Corey 1964; Honarpour et al. 1994). Equations in following form were used in calculations (Eqs.6,7,8):

$$k_{rw} = a(S_w^*)^b \,, \qquad (6)$$

$$k_{rnw} = c(1 - S_w^*)^d \,, \qquad (7)$$

$$S_w^* = \frac{S_w - S_{wi}}{1 - S_{wi} - S_{nwr}} \,, \qquad (8)$$

where: k_{rw} – wetting phase relative permeability; k_{rnw} – non-wetting phase relative permeability; a, b, c, d – empirical constants; S_w^* – effective wetting phase saturation; S_w – wetting phase saturation; S_{wi} – wetting phase irreducible

saturation; S_{nwr} – non-wetting phase residual saturation (minimal non-wetting phase saturation after wetting phase flooding).

The coefficients ‘a’ and ‘c’ correspond to relative permeabilities at end-point saturations S_{wi} and S_{nwr}, respectively. ‘a’ is equal to a maximum k_{rw} at wetting phase saturation equal to 1- S_{nwr}, and ‘c’ is equal to maximum k_{rnw} at wetting phase irreducible saturation (S_{wi}). The relative permeability between constrained end-points, is controlled by the Corey’s exponents ‘b’ and ‘d’. These coefficients were used here in order to match brine displacement in the simulations. For simplicity, the coefficients have been assumed to have the same value for both wetting and non-wetting phase in a given case, i.e. ‘b’=‘d’. Higher exponent values result in a more concave relative permeability curve (lower relative permeability), while lower exponent values result in a less concave curve (higher relative permeability). Exponents where found to be specific to each case and were adjusted based on simulation results, where the matching criteria was ‘brine’ displacement relative to PV of ‘CO_2’ injected. Remaining parameters were estimated based on observations made in experiments and optimised in a number of simulations. Analysing the ‘b’ and ‘d’ parameters used in simulation, a general conclusion is that relative permeabilities became more concaved with decreasing injection rates. Straightening of the curves in case of high-IFT system comparing to low-IFT system is most likely related to the use of micro-barriers in the grid. Barriers limited the flow somewhat, and thus straighter relative permeabilities facilitated flow of the fluid. Additionally, S_{nwr} is higher for the high-IFT cases, which also slowed down the flow of the non-wetting phase. All parameters used in calculations of relative permeability curves are listed in Table 4.

The effect of the capillary pressure, P_c, was tested, but it is not included here. Use of the P_c in simulations, especially those in high-IFT system, caused smoothening of the displacement front, which was the opposite of the observed effect.

Table 4 Parameters used in calculations of the relative permeability curves used in simulations

Parameter	Case					
	1A	1B	1C	2A	2B	2C
S_{wi}	0.20					
S_{nwr}	0.40					
a	1.00					
c	0.80					
b	2.50	1.50	1.00	4.50	3.15	2.50
d						

Parameter	Case					
	3A	3B	3C	4A	4B	4C
S_{wi}	0.10					
S_{nwr}	0.20					
a	1.00					
c	0.90					
b	3.90	3.25	2.65	4.75	3.40	2.50
d						

4 Results

The experiments showed the plume development and the flow patterns of the injected fluid from the start of injection until the plume reached the top of the model reservoir. They represented gravity and viscous unstable floods and, in all cases fingering was observed at the displacement fronts. The fingering was especially pronounced in the high-IFT system, where the fingers transformed more into channel-like structures. Fingering was also visible in the low-IFT system, although fingers were much shorter in these cases.

Changes in fluid saturation during injection of the lighter fluid (model-CO_2) are shown in Fig. 3 through Fig. 6. Pictures presented here were taken after injection of 0.01, 0.10, and 0.25 of the model's PV. Saturation changes, i.e. the fraction of the PV injected, during the experiments were calculated from the mass balance of the injected and produced fluids. It should be noted that it is not straightforward to see a magnitude of the saturation changes by inspection of the pictures due to their resolution and not uniform lighting conditions for all experiments. Results of the modelling by numerical simulations of the laboratory experiments are also presented in Fig. 3 through Fig. 6, next to the respective experiment.

The main criteria in the numerical modelling were to match the observed production of the water-rich phase ('brine') and based on that, compare the distribution of the fluids in the model at corresponding relative time-steps (fraction of the PV injected). Results of the 'brine' production matching are presented in Fig. 7.

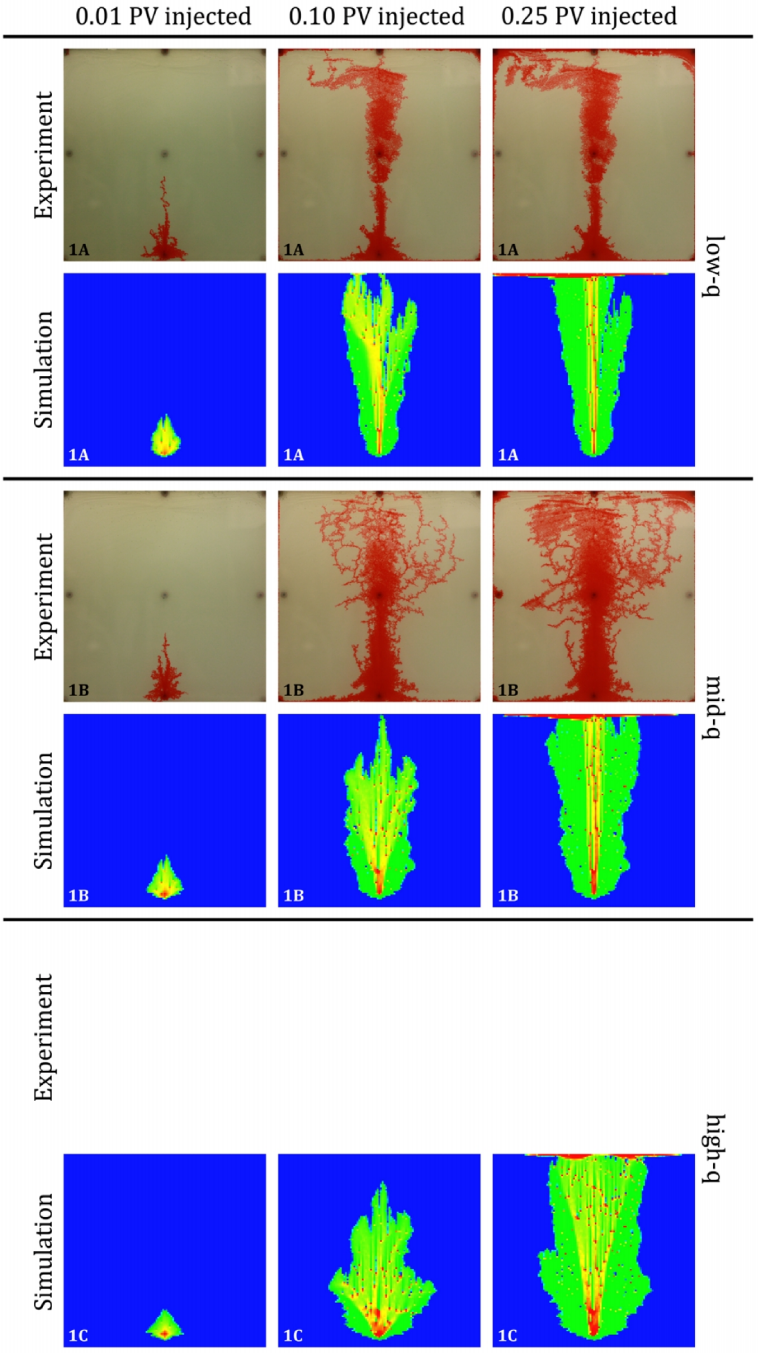

Fig. 3 Saturation maps of experiments and simulations at high-IFT and low-k (cases 1A, 1B, 1C); figures show displacements at 0.01, 0.10, and 0.25 PV of the light phase injected; figures for experiments are representative within each case; note that experiment in Case 1C was not performed

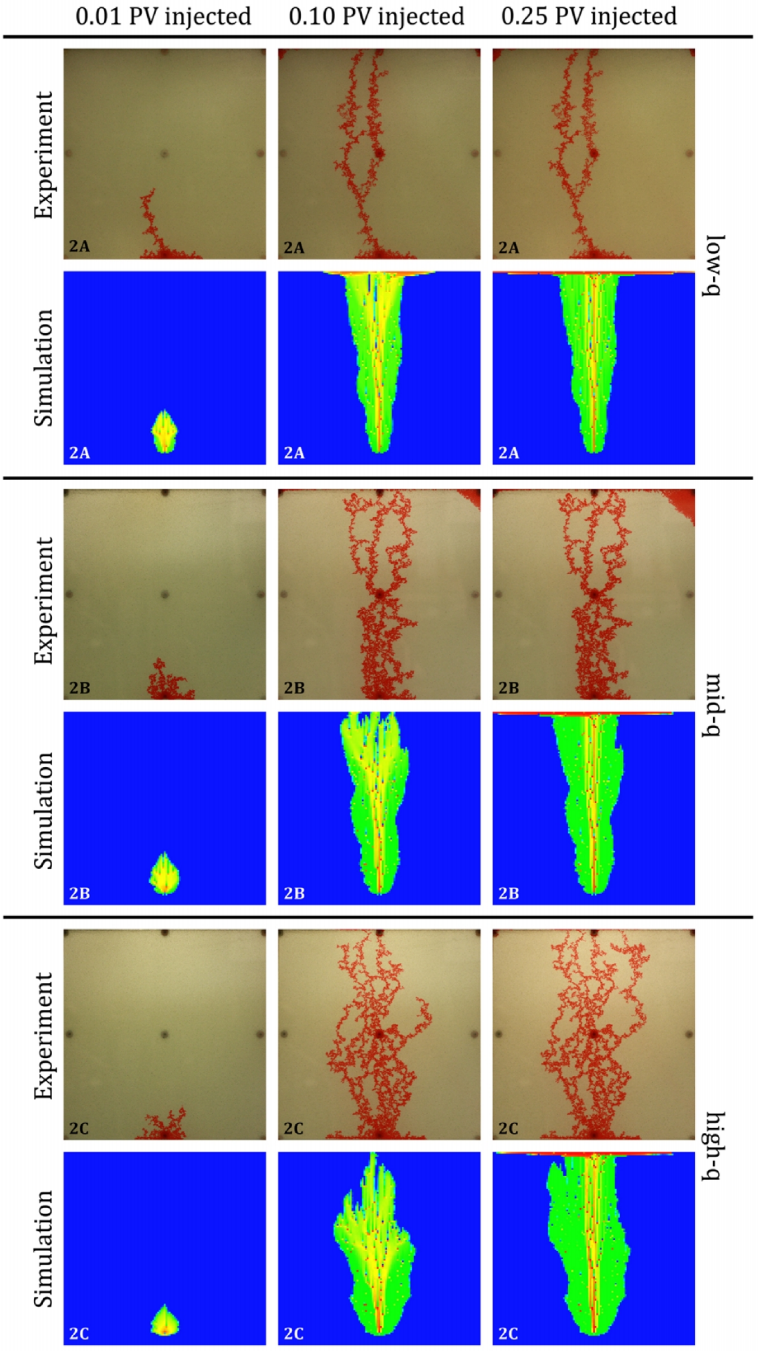

Fig. 4 Saturation maps of experiments and simulations at high-IFT and high-k (cases 2A, 2B, 2C); figures show displacements at 0.01, 0.10, and 0.25 PV of the light phase injected; figures for experiments are representative within each case

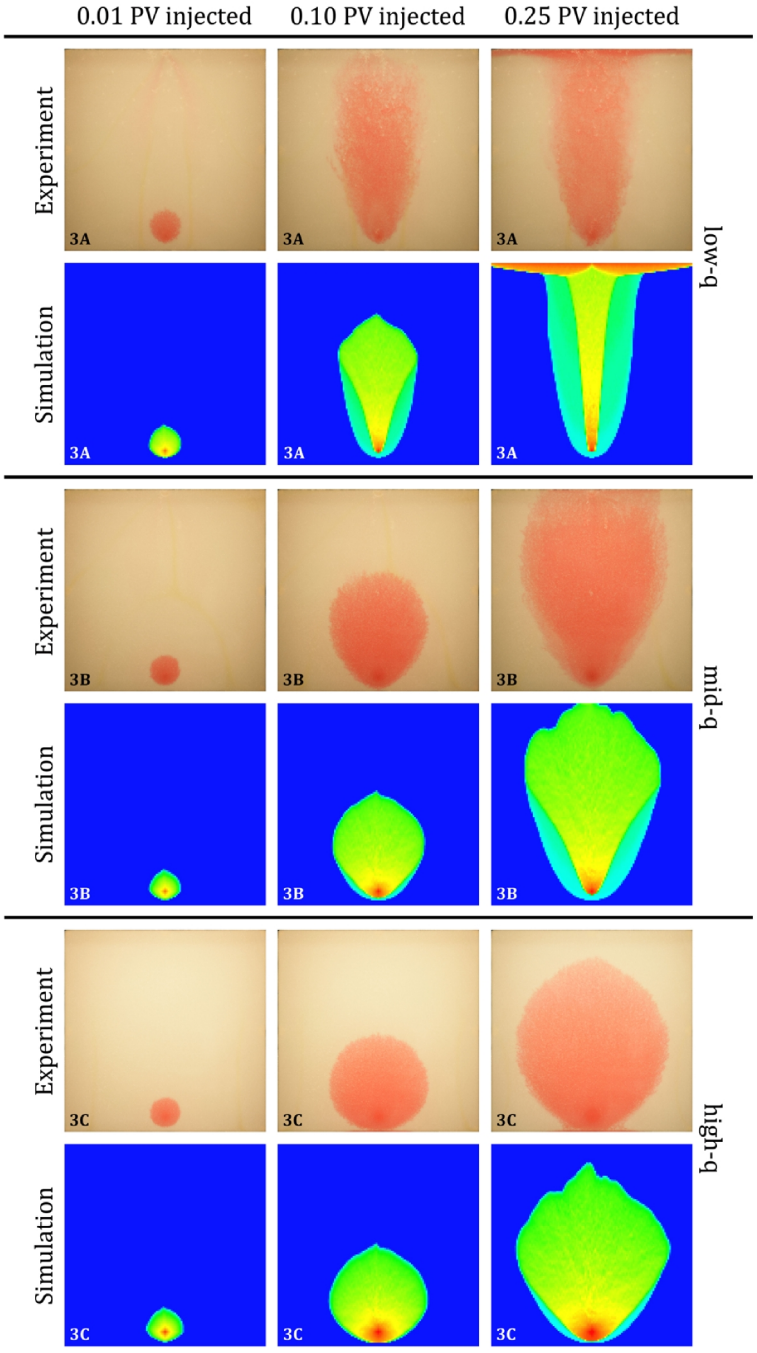

Fig. 5 Saturation maps of experiments and simulations at low-IFT and low-k (cases 3A, 3B, 3C); figures show displacements at 0.01, 0.10, and 0.25 PV of the light phase injected; figures for experiments are representative within each case

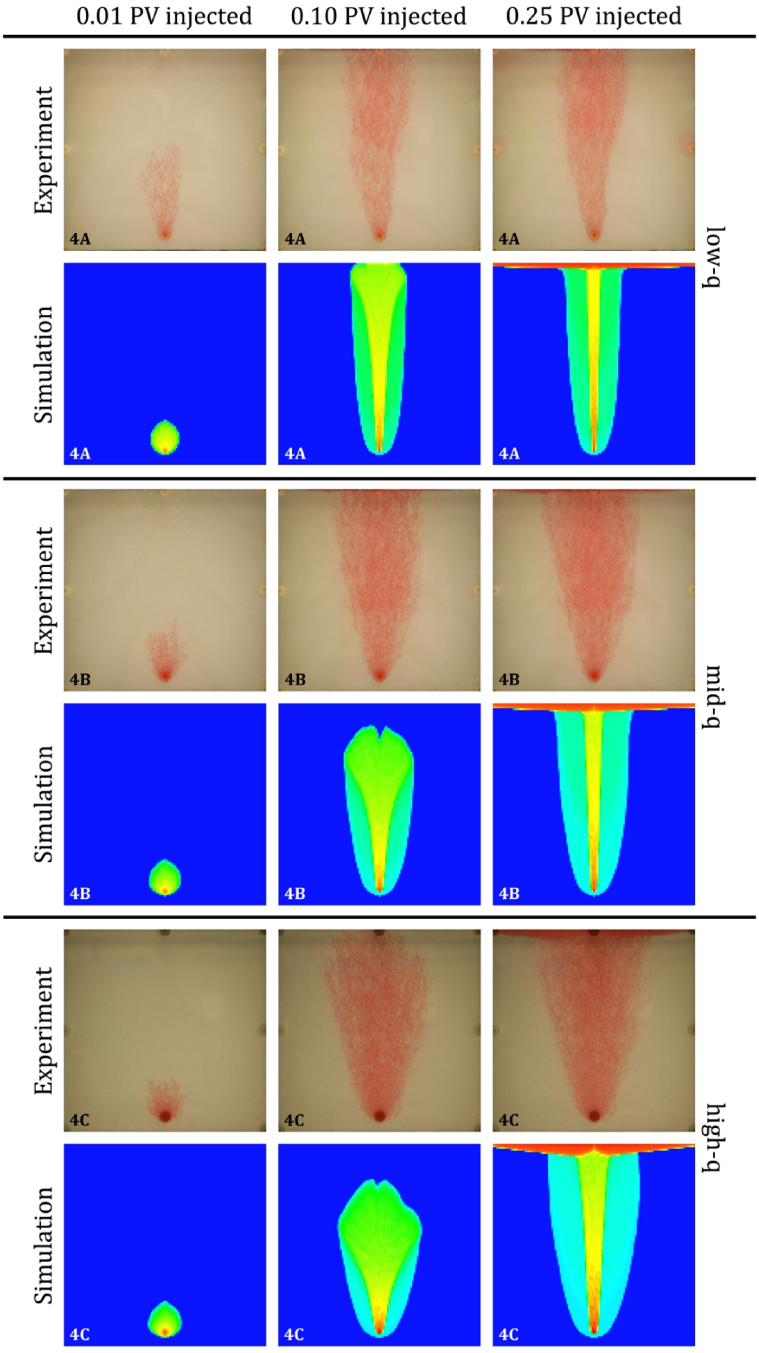

Fig. 6 Saturation maps of experiments and simulations at low-IFT and high-k (cases 4A, 4B, 4C); figures show displacements at 0.01, 0.10, and 0.25 PV of the light phase injected; figures for experiments are representative within each case

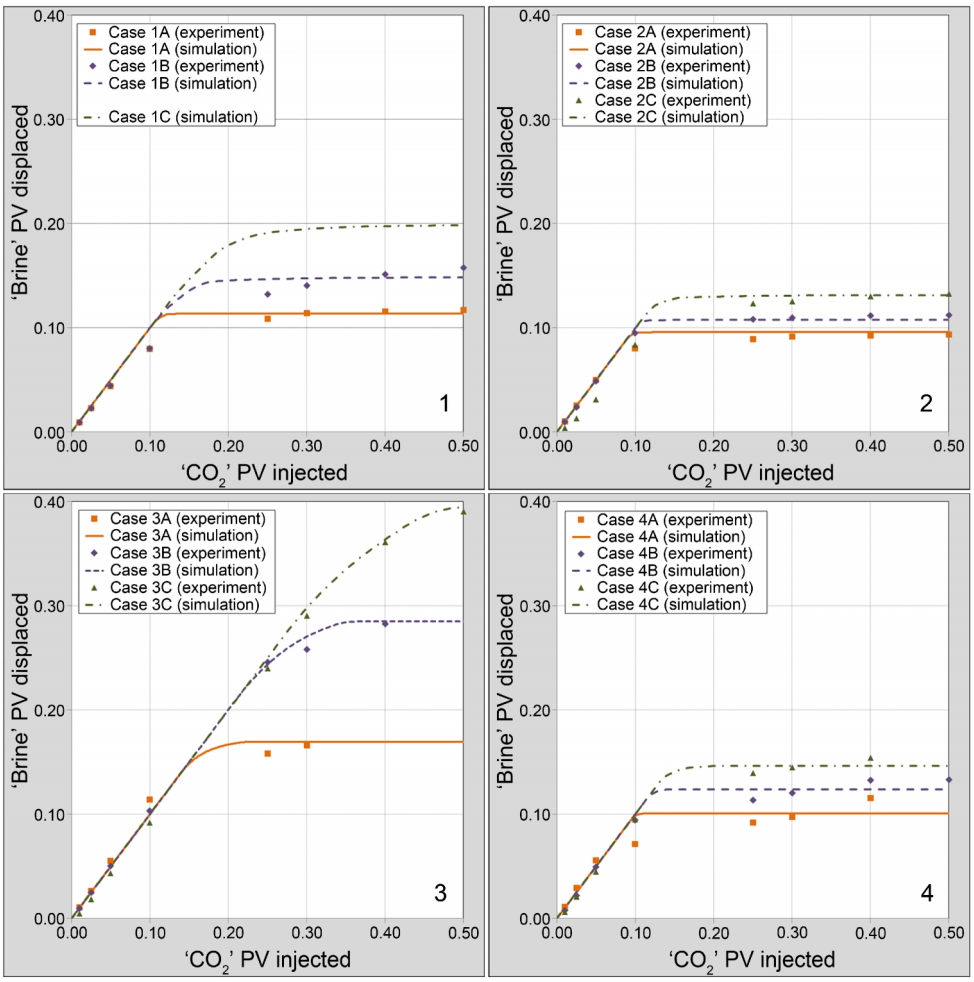

Fig. 7 Brine displacement: experiments (averaged values) vs. simulation matching

5 Discussion

The general observation from the comparison of the saturation 'maps' in the experiments with the simulations is that simulations matched the experiments reasonably well. It is clear, however, that the shape of the injection plumes in the low-IFT experiments were more accurately reproduced by the simulations. The high-IFT system was more challenging, and it was difficult to obtain similar patterns of fingering/channels even with the help of randomly introduced micro-barriers. There can be observed, however, high-saturation flow-paths, which resemble channels from the experiments. Those can be clearly seen in all cases in Fig. 4 and particularly well at 0.10 PV injected. Later, i.e. at 0.25 PV injected, these high-saturation flow-paths disappeared or became vertical, and only shape of

the injection plume, visible as a residual saturation of the injected phase, corresponds to the outermost reach of the channels formed in the experiments (compare in Fig. 4 saturation changes in experiments and simulations at 0.10 and 0.25 PV injected).

From the results of the experiments (Fig. 3 - Fig. 6) it can also be seen that, at low injection rates, the plume of the injected fluid was narrowest. This was due to the gravity effects (see Fig. 2) which were more pronounced in such cases, and it was especially emphasized at high-k cases. Density difference between fluids caused that injected fluid, lighter and thus buoyant, at low injection rate flowed more in the vertical direction (cases 1A, 2A, 3A, and 4A). As a result, less volume of the in-situ fluid was displaced (Fig. 7) compared to the mid- and high-q cases (cases 1B, 1C, 2B, 2C, 3B, 3C, 4B, 4C). This effect was especially well visible in the high-IFT cases (cases 1 and 2) with case 2A (high-k) reporting lowest 'brine' recovery of all experiments (Fig. 7).

When the injection rate was raised, the impact of viscous forces increased (Fig. 2), which resulted in wider plumes (cases 1B, 1C, 2B, 2C, and especially 3B, 3C, 4B, 4C). By comparing results from cases with the same injection rate and different permeability, it is apparent that wider plume, and thus higher sweep efficiency in the displaced area, was obtained at low-k. This is confirmed by higher 'brine' production shown in Fig. 7 (cases 1 vs. 2, and 3 vs. 4).

When the IFT of the fluids is taken into consideration, it can be seen, that flow of the injected fluid at high-IFT system is dominated by strong fingering or, what better describes it, channelling. From the definition of the capillary number (N_C) (Eq.4) it can be read that the higher the IFT is, the stronger capillary forces will be. In Fig. 2 it can be seen that in case of high-IFT system, the fingering will have strongly capillary character, while at low-IFT fingering will be more of a viscous type. At high-IFT fingering extends into long, irregular channels and once channels are established (i.e. after 'CO_2' breakthrough to the outlet) most of the fluid flow takes place through them, and no noticeable change in saturation is observed during further injection (compare experiments in Fig. 3 and Fig. 4 at 0.10 and 0.25 PV injected). Also, the injection plume's lateral extent at high-IFT system is smaller than at low-IFT cases and the displacement front is significantly more bifurcated. Consequently, a large part of the brine is bypassed resulting in an early breakthrough and consequently lower 'brine' production (Fig. 7, case 1 vs. 3, and 2 vs. 4). This could be seen as an analogy to a possible case of field-scale CO_2 injection, where production wells are used for brine production in order to control pore pressure (Lindeberg et al. 2009; e.g. Bergmo et al. 2011). As soon as CO_2 breakthrough to the production well occurs, it will bypass large part of the reservoir and will be produced together with brine. This is obviously undesired situation that leads to temporary or, in the worst case, permanent shut down of the production well.

Due to channelling in high-IFT cases there is also lack of clearly visible displacement front (see experiments in Fig. 3 and Fig. 4). It is, however, not a case at low-IFT where displacement front can be distinguished. Additionally, in the low-IFT cases, very fine, viscous fingers are formed at the displacement front, which are progressively inhibited by the advancement of the front (see experiments in Fig. 5 and Fig. 6). These fine details were unfortunately not reproduced by the numerical simulation software.

6 Conclusions

This paper has presented results of laboratory experiments and numerical simulations of 'model CO_2' injection into a 2D porous medium initially saturated with 'model brine'. The work focuses on the subject of CO_2 storage in geological formations, but its results are applicable to any kind of setting where the flow parameters are relevant, i.e. properties of fluids, flow rates, properties of porous media, and distribution of forces acting on the fluid flow. The following conclusions are drawn:

1) The high-IFT fluid system has an IFT close to the value of CO_2-brine systems at possible reservoir conditions. The results reported in this study, however, show that the flow in the laboratory model is dominated by capillary forces. It is less likely to observe such flow behaviour at field scale. Hence, the flow and distribution of fluids during experiments using a low-IFT fluid system are expected to better resemble field scale flow behaviour.
2) It has been demonstrated that numerical simulation of high-IFT experimental observations is challenging. It was only possible to reproduce laboratory observations by modifying the properties of the porous medium. Numerical simulation of low-IFT displacements is performed more accurately.
3) It has been confirmed that effects of gravity are more pronounced in cases with low injection rates and high permeability. Due to gravity effects less volume of the in-situ fluid is displaced, as flow occurs more in vertical direction, and thus, large part of 'brine' is bypassed. This is an undesired effect. During CO_2 injection it is preferred that the injected CO_2 displaces as much brine as possible. Therefore reservoir cases giving low influence of gravity forces are more suitable for CO_2 storage.
4) Cases where gravity forces are less dominant are characterised by low permeability and high injection rates. Experimental results demonstrate that increasing the injection rate to achieve stronger viscous forces yields a higher total displacement of brine. This suggests that reservoirs with low permeability allowing high injection rates should therefore be preferred for CO_2 storage. However, at such conditions, the pressure build-up can possibly damage the

geological formation by fracturing. This can lead to an undesired, early breakthrough of CO_2 at brine producing wells, if such were used, or even damage the sealing of the reservoir formation.

List of symbols

A – cross-section surface area, m^2
a, b, c, d – empirical constants in relative permeability calculations
d_b – glass-bead diameter, m or micron
Δp – pressure drop, Pa
$\Delta \rho$ – density difference of the fluids, kg/m^3
g – acceleration of gravity, m/s^2
γ – interfacial tension, IFT, mN/m
h – distance between model's inlet and top outlet, m
IFT – interfacial tension, mN/m
k – permeability, m^2 or mD or D
k_{rnw} – non-wetting phase relative permeability
k_{rw} – wetting phase relative permeability
L – glass bead pack length, m
μ – fluid viscosity, Pa·s
N_C – capillary number
P – pressure, bar
P_c – capillary pressure, bar
PV – pore volume fraction
ϕ – porosity
q – flow rate, m^3/s
R_{CG} – capillary to gravity forces ratio
R_{VG} – viscous to gravity forces ratio
ρ_{nw} – density of non-wetting phase, kg/m^3
ρ_w – density of wetting phase, kg/m^3
S_{nwr} – non-wetting phase residual saturation
S_w – wetting phase saturation
S_w^* – effective wetting phase saturation
S_{wi} – wetting phase irreducible saturation
u – Darcy's flow velocity, m/s

Acknowledgments

The authors gratefully acknowledge SINTEF Petroleum AS and The School of Petroleum Engineering (UNSW) for making their facilities available to perform this research. The authors also acknowledge the funding provided by the Australian Government through the CRC Program to support CO2CRC research.

This publication forms a part of the BIGCO2 project, performed under the strategic Norwegian research program CLIMIT. The authors acknowledge the partners: Statoil, GE Global Research, Statkraft, Aker Clean Carbon, Shell, TOTAL,

ConocoPhillips, ALSTOM, the Research Council of Norway (178004/I30 and 176059/I30) and Gassnova (182070) for their support.

References

Alhamdan, M.R., Cinar, Y., Suicmez, V.S., Dindoruk, B.: Experimental and numerical study of compositional two-phase displacements in layered porous media. Journal of Petroleum Science and Engineering **98–99**(0), 107-121 (2012). doi:http://dx.doi.org/10.1016/j.petrol.2012.09.009

Asghari, K., Torabi, F.: Effect of Miscible and Immiscible CO_2 Flooding on Gravity Drainage: Experimental and Simulation Results. Paper presented at the SPE/DOE Symposium on Improved Oil Recovery, Tulsa, Oklahoma, USA, 20-23 April 2008

Bennion, D.B., Bachu, S.: Dependence on Temperature, Pressure, and Salinity of the IFT and Relative Permeability Displacement Characteristics of CO_2 Injected in Deep Saline Aquifers. Paper presented at the SPE Annual Technical Conference and Exhibition, San Antonio, Texas, USA,

Berg, S., Ott, H.: Stability of CO_2–brine immiscible displacement. International Journal of Greenhouse Gas Control **11**(0), 188-203 (2012). doi:http://dx.doi.org/10.1016/j.ijggc.2012.07.001

Bergmo, P.E.S., Grimstad, A.-A., Lindeberg, E.: Simultaneous CO_2 injection and water production to optimise aquifer storage capacity. International Journal of Greenhouse Gas Control **5**(3), 555-564 (2011). doi:http://dx.doi.org/10.1016/j.ijggc.2010.09.002

Boden, T.A., Marland, G., Andres, R.J.: Global, Regional, and National Fossil-Fuel CO_2 Emissions. In. Carbon Dioxide Information Analysis Center, Oak Ridge National Laboratory, U.S. Department of Energy, Oak Ridge, Tenn., U.S.A., (2010)

Brooks, R., Corey, A.: Hydraulic properties of porous media, Hydrology Papers, No. 3, Colorado State University, Ft. Collins, Colo (1964)

Chiquet, P., Daridon, J.-L., Broseta, D., Thibeau, S.: CO_2/water interfacial tensions under pressure and temperature conditions of CO_2 geological storage. Energy Conversion and Management **48**(3), 736-744 (2007). doi:http://dx.doi.org/10.1016/j.enconman.2006.09.011

Cinar, Y., Jessen, K., Berenblyum, R., Juanes, R., Orr Jr, F.M.: An Experimental and Numerical Investigation of Crossflow Effects in Two-Phase Displacements. SPE Journal, **Volume 11, Number 2**(June 2006), 216-226 (2006). doi:10.2118/36600-MS

Cinar, Y., Riaz, A., Tchelepi, H.A.: Experimental Study of CO_2 Injection Into Saline Formations. SPE Journal **14**(4), 588-594 (2009). doi:10.2118/110628-pa

Corey, A.T.: The interrelation between gas and oil relative permeabilities. Producers monthly **19**(1), 38-41 (1954)

Duan, S., Wojtanowicz, A.K.: Laboratory Investigation of Immiscible Transverse Dispersion Using Hele-Shaw Experiment. Paper presented at the Petroleum Society of Canada. doi:10.2118/2007-187,

Holt, T., Vassenden, F.: Physical Gas/Water Segregation Model. In: Skjæveland, S.M., Skauge, A., Hinderaker, L., Sisk, C.D. (eds.) RUTH 1992-1995 - a Norwegian research program on improved oil recovery - program summary. p. 446 s. Norwegian Petroleum Directorate, Stavanger (1996)

Homsy, G.: Viscous fingering in porous media. Annual Review of Fluid Mechanics **19**(1), 271-311 (1987)

Honarpour, M., Koederitz, L., Harvey, A.H.: Relative permeability of petroleum reservoirs. Society of Petroleum Engineers, [S.l.] (1994)

IEA-GHG: Aquifer Storage – Development Issues. In. IEA Greenhouse Gas R&D Programme, (2008)

IPCC: IPCC Special Report on Carbon Dioxide Capture and Storage. Prepared by Working Group III of the Intergovernmental Panel on Climate Change. In: Metz, B., Davidson, O., de Coninck, H.C., Loos, M., Meyer, L.A. (eds.). Cambridge University Press, Cambridge, UK and New York, NY, USA, (2005)

IPCC: Summary for Policymakers. In: Climate Change 2007: Mitigation. Contribution of Working Group III to the Fourth Assessment Report of the Intergovernmental Panel on Climate Change. In: Metz, B., Davidson, O.R., Bosch, P.R., Dave, R., Meyer, L.A. (eds.). Cambridge University Press, Cambridge, UK and New York, NY, USA, (2007)

Islam, A., Chevalier, S., Sassi, M.: Experimental and Numerical Studies of CO_2 Injection Into Water-Saturated Porous Medium: Capillary to Viscous to Fracture Fingering Phenomenon. Energy Procedia **37**(0), 5511-5519 (2013). doi:http://dx.doi.org/10.1016/j.egypro.2013.06.471

Kaviany, M.: Principles of heat transfer in porous media, 2nd ed. Mechanical engineering series. Springer, New York (1995)

Kopp, A., Class, H., Helmig, R.: Investigations on CO_2 storage capacity in saline aquifers: Part 1. Dimensional analysis of flow processes and reservoir characteristics. International Journal of Greenhouse Gas Control **3**(3), 263-276 (2009)

Lindeberg, E., Vuillaume, J.-F., Ghaderi, A.: Determination of the CO_2 storage capacity of the Utsira formation. Energy Procedia **1**(1), 2777-2784 (2009). doi:http://dx.doi.org/10.1016/j.egypro.2009.02.049

Løvoll, G., Méheust, Y., Måløy, K.J., Aker, E., Schmittbuhl, J.: Competition of gravity, capillary and viscous forces during drainage in a two-dimensional porous medium, a pore scale study. Energy **30**(6), 861-872 (2005)

Michael, K., Allinson, G., Golab, A., Sharma, S., Shulakova, V.: CO_2 storage in saline aquifers II-Experience from existing storage operations. Energy Procedia **1**(1), 1973-1980 (2009)

Nordbotten, J.M., Celia, M.A., Bachu, S.: Injection and Storage of CO_2 in Deep Saline Aquifers: Analytical Solution for CO_2 Plume Evolution During Injection. Transport in Porous Media **58**(3), 339-360 (2005)

Polak, S., Cinar, Y., Holt, T., Torsæter, O.: An experimental investigation of the balance between capillary, viscous, and gravitational forces during CO_2 injection into saline aquifers. Energy Procedia **4**, 4395-4402 (2011). doi:10.1016/j.egypro.2011.02.392

Rumpf, H., Gupte, A.R.: The influence of porosity and grain size distribution on the permeability equation of porous flow. Chemie Ing. Techn. (Weinheim) (Transl. into ENGLISH) **43**(6), 367-375 (1975)

Saffman, P.G., Taylor, G.: The penetration of a fluid into a porous medium or Hele-Shaw cell containing a more viscous liquid. Proceedings of the Royal Society of London. Series A. Mathematical and Physical Sciences **245**(1242), 312-329 (1958)

Schechter, D.S., Zhou, D., Orr Jr, F.M.: Capillary Imbibition and Gravity Segregation in Low IFT Systems. Paper presented at the SPE Annual Technical Conference and Exhibition, Dallas, Texas, 01/01/1991

Stocker, T.F., D. Qin, G.-K. Plattner, L.V. Alexander, S.K. Allen, N.L. Bindoff, F.-M. Bréon, J.A. Church, U. Cubasch, S. Emori, P.F., P. Friedlingstein, N. Gillett, J.M. Gregory, D.L. Hartmann, E. Jansen, B. Kirtman, R. Knutti, K., Krishna Kumar, P.L., J. Marotzke, V. Masson-Delmotte, G.A. Meehl, I.I. Mokhov, S. Piao, V. Ramaswamy, D., Randall, M.R., M. Rojas, C. Sabine, D. Shindell, L.D. Talley, D.G. Vaughan and S.-P. Xie (eds.): Technical Summary. Cambridge University Press, Cambridge, United Kingdom and New York, NY, USA (2013)

Taku Ide, S., Jessen, K., Orr Jr, F.M.: Storage of CO_2 in saline aquifers: Effects of gravity, viscous, and capillary forces on amount and timing of trapping. International Journal of Greenhouse Gas Control **1**(4), 481-491 (2007)

Wood, D.J., Lake, L.W., Johns, R.T., Nunez, V.: A Screening Model for CO_2 Flooding and Storage in Gulf Coast Reservoirs Based on Dimensionless Groups. SPE Reservoir Evaluation & Engineering **Volume 11, Number 3**(June 2008), 513-520 (2008). doi:10.2118/36600-MS

Appendix E: Example of the simulation input file

Example of the ECLIPSE 100 simulation input file ('DATA' file) used for simulations of the laboratory experiments. Here data for the case 4A (low-IFT, high-k, low-q) is presented. Each of the cases had unique input file due to the different model and fluid properties, as well as the injection rate. Input parameters for all simulations are listed in Table 3.2, Table 3.4, Table 3.5, and Table 3.10.

```
-------------------------------------------------------------------------
-- Case 4A - low IFT, high k, low q
-- low-IFT:        1    mN/m
-- high-k:   108 500    mD
-- low-q:          0.10 cc/min
-- glass-beads: 300-400 micron
-------------------------------------------------------------------------


-------------------------------------------------------------------------
RUNSPEC ----------------------------------------------------------------
-------------------------------------------------------------------------

TITLE
  Injection into 2D glass-bead model

DIMENS
-- Grid Dimensions
--  NX  NY    NZ
   121   1   121 /

GRIDOPTS
  YES /

-- Active Phases Present
WATER
GAS
```

```
-- Unit system
LAB

-- Restart And Summary Files Are To Be Unified
UNIFOUT
-- Restart From A Unified Restart File
UNIFIN

-- No non-neighbour connections
NONNC

WELLDIMS
-- Well Dimension Data
-- NWMAXZ NCWMAX NGMAXZ NWGMAX
-- ------ ------ ------ ------
       10     10      2     10 /

TABDIMS
-- Table Of Dimensions
-- NTSFUN  NTPVT  NSSFUN  NPPVT  NTFIP  NRPVT
-- ------  -----  ------  -----  -----  -----
        1      1      30     30      1      2 /

START
-- DAY  MONTH  YEAR
-- ---  -----  ----
     1    JAN  2010 /

NSTACK
-- Stack Size For Linear Solver
   500 /

-- Disable echoing of the input file
NOECHO


------------------------------------------------------------------------------
GRID    ----------------------------------------------------------------------
------------------------------------------------------------------------------

EQUALS
  TOPS  0         1  121  1  1  1    1  /
--
  DX    0.2516    1  121  1  1  1  121  /
  DY    0.2600    1  121  1  1  1  121  /
  DZ    0.2516    1  121  1  1  1  121  /
--
  PORO  0.3880    1  121  1  1  1  121  /
/
```

```
INCLUDE
-- permeability has normal distribution, with mean value
-- equal to the C-K calculated permeability and
-- standard deviation equal to 10% of the mean value
  'include/PERMX_4_14641_GB300-400_108500mD_SD.dat' /

COPY
  'PERMX'   'PERMY' /
  'PERMX'   'PERMZ' /
/

-- randomly distributed transmissibility micro-barriers
-- included only in high-IFT cases
--INCLUDE
--  'include/MULTX__14641_P02_01.dat' /
--INCLUDE
--  'include/MULTX-_14641_P02_02.dat' /
--INCLUDE
--  'include/MULTZ__14641_P02_03.dat' /
--INCLUDE
--  'include/MULTZ-_14641_P02_04.dat' /

INIT

NOECHO


-----------------------------------------------------------------------------
EDIT    -----------------------------------------------------------------------
-----------------------------------------------------------------------------


-----------------------------------------------------------------------------
PROPS   -----------------------------------------------------------------------
-----------------------------------------------------------------------------

ROCK
-- Pref       Cr
    1.0   5.0E-5 /

DENSITY
-- low-IFT system
-- at surface conditions in g/cc
--    OIL    WATER      GAS
   0.6975    0.9031     0.6975 /

PVTW
-- low-IFT system
-- Pref   Bw(Pref)       Cw    Visc   Viscosibility
-- atma    rcc/scc    1/atm      cP           1/atm
    1.0        1.0   4.0e-5   3.556              1* /
```

```
PVDG
-- low-IFT system; lighter phase modelled as gas
-- because viscosity is lower than for the aqueous phase
--   p           Bg    Visc
-- atm      rcc/scc      cP
   1.0   1.00000001   0.556
   1.5   1.00000000   0.556
/

SGWFN
-- Swi  = 0.10; Snwr = 0.20
-- a    = 1.00; c    = 0.90
-- b    = 4.75; d    = 4.75
-- Sg   krnw           krw            Pc
0.00    0.000000       1.000000       0
0.20    0.000000       1.000000       0
0.25    0.000003       0.703271       0
0.30    0.000087       0.480842       0
0.35    0.000598       0.318059       0
0.40    0.002344       0.202252       0
0.45    0.006765       0.122615       0
0.50    0.016082       0.070076       0
0.55    0.033446       0.037163       0
0.60    0.063068       0.017869       0
0.65    0.110354       0.007516       0
0.70    0.182026       0.002604       0
0.75    0.286253       0.000664       0
0.80    0.432758       0.000097       0
0.85    0.632944       0.000004       0
0.90    0.900000       0.000000       0
/


--------------------------------------------------------------------------
REGIONS  ---------------------------------------------------------------
--------------------------------------------------------------------------


--------------------------------------------------------------------------
SOLUTION ---------------------------------------------------------------
--------------------------------------------------------------------------

EQUIL
-- Datum   Pinit@Datum   GWC   Pc@GWC
     0.0           1.0   0.0        0 /
-- datum is set at the top of the model

RPTRST
  BASIC=2             /

RPTSOL
  FIP=1 RESTART=2 PRESSURE SGAS SWAT /
```

```
------------------------------------------------------------------------------
SUMMARY ----------------------------------------------------------------------
------------------------------------------------------------------------------

-- Options
SEPARATE
RPTONLY
RUNSUM
EXCEL

-- Field
FPR
FGIR
FGIT
FGPR
FGPT
FGIP
FWPR
FWPT
FWIP
FVPR
FVPT
-- Wells
WBHP
/
WGIR
'INJE' /
WGIT
'INJE' /
WGPR
'PROD*' /
WGPT
'PROD*' /
WWPR
'PROD*' /
WWPT
'PROD*' /


------------------------------------------------------------------------------
SCHEDULE ---------------------------------------------------------------------
------------------------------------------------------------------------------

WELSPECS
--  WELL   WELL   LOCATION       BHP   PREFERRED   DRAINAGE
--  NAME  GROUP      I   J     DATUM       PHASE     RADIUS
  'INJE'   'IN'     61   1        1*       'GAS'         1* /
  'PRODTM' 'PR'     61   1        1*     'WATER'         1* /
  'PRODTL' 'PR'      1   1        1*     'WATER'         1* /
  'PRODTR' 'PR'    121   1        1*     'WATER'         1* /
  'PRODML' 'PR'      1   1        1*     'WATER'         1* /
  'PRODMR' 'PR'    121   1        1*     'WATER'         1* /
  'PRODBL' 'PR'      1   1        1*     'WATER'         1* /
```

```
  'PRODBR' 'PR'    121   1        1*     'WATER'         1* /
/

COMPDAT
--WELL      L O C A T I O N  WELL  Sat.  Transm. Wellbore Eff. Skin D-fact Dir.
--NAME       I  J   K1   K2  STAT. Tabl# Fact.   Diam. cm  Kh
  'INJE'    61  1  113  113  'OPEN'   0     1*   0.09962   1*    1*   1*    Y /
  'PRODTM'  61  1    1    1  'OPEN'   0     1*   0.09962   1*    1*   1*    Y /
  'PRODTL'   1  1    1    1  'OPEN'   0     1*   0.09962   1*    1*   1*    Y /
  'PRODTR' 121  1    1    1  'OPEN'   0     1*   0.09962   1*    1*   1*    Y /
  'PRODML'   1  1   61   61  'OPEN'   0     1*   0.09962   1*    1*   1*    Y /
  'PRODMR' 121  1   61   61  'OPEN'   0     1*   0.09962   1*    1*   1*    Y /
  'PRODBL'   1  1  121  121  'OPEN'   0     1*   0.09962   1*    1*   1*    Y /
  'PRODBR' 121  1  121  121  'OPEN'   0     1*   0.09962   1*    1*   1*    Y /
/

WCONINJE
--  WELL   INJ   WELL   CONTROL   FLOW  RATE  TARG.    BHP     THP        VFP
--  NAME   TYPE  STATUS MODE      SURFACE  RES.        TARG.   TARG.   TABLE#
--                               scc/hr     rcc/hr    atma    atma
  'INJE'   'GAS' 'OPEN' 'RATE'       6.0         1*       1*      1*       1* /
/

WCONPROD
--  WELL     WELL    CONTROL   F L O W  R A T E  T A R G E T     BHP   THP   VFP
--  NAME   STATUS      MODE    OIL  WATER  GAS  LIQ.  RES.FL.   TARG. TARG.TABLE#
--                             ------------ cc/hr -----------   atma  atma
  'PRODTM'  'OPEN'    'BHP'    1*     1*   1*     1*     1*   1.0001   1*   1* /
  'PRODTL'  'OPEN'    'BHP'    1*     1*   1*     1*     1*   1.0001   1*   1* /
  'PRODTR'  'OPEN'    'BHP'    1*     1*   1*     1*     1*   1.0001   1*   1* /
  'PRODML'  'OPEN'    'BHP'    1*     1*   1*     1*     1*   1.0133   1*   1* /
  'PRODMR'  'OPEN'    'BHP'    1*     1*   1*     1*     1*   1.0133   1*   1* /
  'PRODBL'  'OPEN'    'BHP'    1*     1*   1*     1*     1*   1.0265   1*   1* /
  'PRODBR'  'OPEN'    'BHP'    1*     1*   1*     1*     1*   1.0265   1*   1* /
/

WTEST
--  WELL       PERIOD      REASON
--  NAME           hr    FOR TEST
  'INJE'     0.016667         'P' /
  'PRODTM'   0.016667         'P' /
  'PRODTL'   0.016667         'P' /
  'PRODTR'   0.016667         'P' /
  'PRODML'   0.016667         'P' /
  'PRODMR'   0.016667         'P' /
  'PRODBL'   0.016667         'P' /
  'PRODBR'   0.016667         'P' /
/
```

```
TUNING
--TSINIT TSMAXZ TSMINZ   TSMCHP  TSFMAX  TSFMIN TSFCNV   TSDIFF  THRUPT TMAXWC
   .1      1.5    .051     .015     3.0     0.3    0.1     1.25    1E20    1* /
--TRGTTE TRGCNV TRGMBE TRGLCV XXXTTE XXXCNV  XXXMBE  XXXLCV XXXWFL TRGFIP TRGSFT
  0.1    0.001  1.0E-7 1.0E-6   10    0.01   1.0E-6  0.00001  0.001 0.025  1* /
--NEWTMX NEWTMN LITMAX LITMIN  MXWSIT  MXWPIT DDPLIM  DDSLIM  TRGDPR  XXXDPR
  12      1      800      1       8       8    1.6E6   1.0E6   1.0E6   1.0E6  /

TUNINGDP
--       TRGDDP   TRGDDS
  1*   1*   1.0     0.01 /

TSTEP
-- 1.0 min intervals
  466*0.016667
-- 0.50 PV injected at 0.10 cc/min
-- 7 h 46 min from start
/

-- stop of injection
WCONINJE
--  WELL   INJ   WELL   CONTROL   FLOW  RATE  TARG.    BHP     THP        VFP
--  NAME   TYPE  STATUS MODE      SURFACE  RES.        TARG.   TARG.   TABLE#
--                               scc/hr     rcc/hr    atma    atma
  'INJE'   'GAS' 'SHUT' 'RATE'       0.0         1*       1*      1*       1* /
/

TSTEP
-- 1.0 min intervals
  74*0.016667
-- 9 h total time of the run
/


-------------------------------------------------------------------------------
END     ---------------------------------------------------------------------
-------------------------------------------------------------------------------
```